DISSERTATION

RESPONSE AND TRANSPORT PROPERTIES IN COMPLEX QUANTUM SPIN SYSTEMS

Submitted by

Christopher Ard

Department of Physics

In partial fulfillment of the requirements

For the Degree of Doctor of Philosophy

Colorado State University

Fort Collins, Colorado

Fall 2025

Doctoral Committee:

Advisor: Hua Chen

Kristen Buchanan
Martin Gelfand
Olivier Pinaud

ABSTRACT

RESPONSE AND TRANSPORT PROPERTIES IN COMPLEX QUANTUM SPIN SYSTEMS

Understanding how quantum systems respond to external perturbations lies at the core of condensed matter physics. In spin systems—where localized magnetic moments interact through exchange, spin-orbit coupling, and external fields—these responses are often rich with emergent behavior. Spin degrees of freedom not only govern magnetic ordering and excitations, but also mediate charge and heat transport, and serve as carriers of information in next-generation quantum technologies. This dissertation investigates how complexity—arising from spatial inhomogeneity, many-body interactions, or local spin structure—affects the transport and response properties of quantum spin systems.

A central focus of this work is to clarify and reinterpret signatures observed in Hall transport measurements of magnetic materials. In Chapter 1, I explore how spatial inhomogeneities and resistances due to the presence of domain walls can mimic features traditionally associated with topological spin textures, such as skyrmions. Using homogenization theory, we derive rigorous bounds on the anomalous Hall conductivity (AHC) in inhomogeneous conductors under minimal assumptions. While the homogenized AHC must lie within the range of local conductivities, I show that experimental configurations involving inhomogeneous magnetic domains can give rise to apparent anomalies—such as humps in the Hall resistance hysteresis loop—without invoking topological effects. This result offers a non-topological explanation for widely observed transport features and underscores the importance of disentangling geometric, topological, and extrinsic contributions in interpreting experimental data.

Chapter 2 addresses a different aspect of spin response: the control of magnetic relaxation dynamics through local environmental design. Motivated by the need to suppress decoherence in spin-based quantum devices, we present a new strategy for engineering long spin relaxation

times by embedding a magnetic complex within a chemically compatible, but spin-active, matrix. Specifically, we show that the magnetic relaxation of the $[Co(SPh)_4]^{2^-}$ complex can be slowed by three orders of magnitude when embedded in isostructural lattices of $[M(SPh)_4]^{2^-}$ (M = Ni^{2+}, Fe^{2+}, Mn^{2+}). Magnetometry, EPR, and computational analyses reveal that the host matrices' large positive zero-field splitting and integer spin values generate a dynamically quiet local environment. Unlike traditional strategies that rely on diamagnetic dilution, this approach leverages structured magnetic environments to suppress spin noise—opening new design principles for molecular qubits and coherent spin systems.

Finally, Chapter 3 focuses on spin-orbit-driven transport phenomena that underlie much of modern spintronics. In systems with strong spin-orbit coupling (SOC), the spin Hall effect (SHE) and its inverse enable the interconversion of spin and charge currents—offering powerful tools for manipulating non-equilibrium spin states. This chapter examines the microscopic origins of the SHE and ISHE, their dependence on crystal symmetry and SOC strength, and the conditions under which transverse spin currents can be maximized or suppressed. These results contribute to the growing theoretical understanding of spin-charge coupling mechanisms and provide guidelines for optimizing spin current generation in realistic materials and devices.

Taken together, the results presented in this dissertation shed light on how local structure, symmetry, and disorder shape the transport and dynamical properties of quantum spin systems. The overarching theme is one of complexity—how microscopically diverse environments and interactions can yield counterintuitive or emergent behavior in macroscopic response. In doing so, this work provides theoretical tools, reinterpretations, and design strategies that are broadly relevant to the study of magnetic materials, spintronic devices, and quantum information platforms.

DEDICATION

I would like to dedicate this to my family

TABLE OF CONTENTS

LIST OF TABLES

LIST OF FIGURES

Chapter 1

Introduction

The study of spin-dependent transport phenomena lies at the heart of modern condensed matter physics, both as a fundamental theoretical challenge and as a foundation for emerging spin-based technologies. The field of spintronics, in particular, seeks to utilize the spin degree of freedom of electrons to manipulate the equilibrium and nonequilibrium properties of quantum materials. In this dissertation, we investigate several critical aspects of spin transport and spin response, focusing on the role of spatial inhomogeneities, magnetic interactions, and spin-orbit coupling in shaping measurable effects such as the anomalous Hall effect (AHE), spin relaxation dynamics, and the spin Hall effect (SHE).

The anomalous Hall effect is a hallmark of ferromagnetic systems with broken time-reversal symmetry and strong spin-orbit coupling. While the intrinsic AHE is widely understood in homogeneous materials through Berry curvature physics, interpreting experiments on real samples often encounters a major obstacle: spatial inhomogeneity. Domain walls, texture boundaries, and nonuniform current paths can all significantly alter the measured Hall voltage, often in ways that defy naive expectations.

In Chapter 2, we rigorously address this issue using tools from homogenization theory—a branch of applied mathematics concerned with the effective properties of heterogeneous media. We establish general upper and lower bounds on the homogenized anomalous Hall conductivity based solely on local conductivity tensors. We prove that under minimal assumptions, the effective Hall conductivity cannot exceed the range spanned by the local anomalous Hall response.

Surprisingly, however, certain anomalies frequently observed in experiments—such as nonmonotonic features or "humps" in Hall resistance hysteresis loops—appear to violate these bounds. These features are often attributed to the topological Hall effect arising from skyrmions or chiral spin textures. Our work shows that similar signatures can arise even in systems without any topological spin texture, purely due to inhomogeneities in the material or due to the presence of a do-

main wall. This is described in Fig. 2.1. Through two concrete examples, we demonstrate how spatial inhomogeneities alone can mimic THE-like behavior, raising caution about over-interpretation of Hall data in complex materials. These apparent contradictions can be resolved either by recognizing that the extrema—humps and dips—represent the bounds and can exceed the saturated conductivity, or by noting that the hump observed in the hysteresis curve appears in the resistivity; upon inversion to obtain the conductivity, the hump vanishes. This work was conducted in collaboration with Hua Chen, Olivier Pinaud, and Evan Camrud. The homogenization analysis was primarily carried out by Evan Camrud and Olivier Pinaud. The results were published in Communications Physics [1].

Spin relaxation mechanisms govern the lifetime of nonequilibrium spin polarizations and are central to the design of spin-based memory or quantum information platforms. While much attention has been given to spin-orbit-mediated relaxation channels, recent work has shown that dipolar interactions between localized spins can dominate in certain molecular or insulating systems. These interactions are long-ranged, anisotropic, and intrinsically inhomogeneous due to local structural disorder.

In Chapter 3, we develop a dipolar field model to study spin relaxation from a linear response perspective. We treat an ensemble of spins coupled via dipole-dipole interactions and subject to thermal fluctuations. Using a perturbative approach, we compute the dynamical susceptibility and extract characteristic spin relaxation times as a function of interaction strength and spatial configuration. This work was carried out in collaboration with Ian Mosely, Joe Zadrozny, and Hua Chen. Ian Mosely and Joe Zadrozny performed the experimental measurements. The results were published in Cell Reports Physical Science [2].

A key result is that increasing the dipolar interaction strength—counterintuitively—can slow down spin relaxation. We trace this to a suppression of local field fluctuations as the system becomes more correlated, leading to a kind of self-stabilization of spin orientation. This insight opens new avenues for chemically engineering longer spin lifetimes by tuning dipolar couplings through the choice of molecular ligands or host matrices.

The spin Hall effect (SHE) and its reciprocal, the inverse spin Hall effect (ISHE), offer a route to generate and detect spin currents in nonmagnetic systems via spin-orbit coupling. These effects are pivotal to many spintronic devices, yet their interpretation—particularly in materials with strong spin-orbit coupling—remains subtle. The notion of a spin current itself becomes ill-defined when spin is not conserved, complicating continuity equations and transport formalisms.

In Chapter 4, we revisit the spin Hall response, including both intrinsic and extrinsic contributions to the spin current. We examine the role of spin accumulation at sample boundaries and the impact of strong spin-orbit interaction, where the spin current ceases to be a conserved or even a gauge-invariant quantity. In such regimes, we argue that focusing on measurable spin densities or edge accumulations, rather than bulk spin currents, provides a more physically robust description.

We also present a novel computational approach based on a tight-binding Hamiltonian that includes both Kane-Mele-type spin-orbit coupling and electronic interactions. This allows us to capture both the band-structure-derived (intrinsic) and interaction-driven contributions to spin accumulation. We find that the interplay of these two ingredients can significantly modify the magnitude and sign of the transverse spin response.

Conclusion and Outlook

Taken together, the three chapters of this dissertation highlight the crucial role that spatial inhomogeneities and internal interactions play in determining spin transport phenomena. While linear response theory provides a rigorous foundation for analyzing such effects, the presence of disorder, long-range interactions, or nonuniform geometries necessitates careful theoretical and computational treatment. By combining analytical bounds, perturbative modeling, and numerical simulations within a unified linear response framework, this work offers new perspectives on how to interpret and manipulate spin transport in complex quantum systems.

The results have implications not only for basic understanding but also for practical spintronics, where engineering the local environment and interaction profile may prove as important as band structure design. Future work may extend these methods to time-dependent phenomena, nonper-

turbative effects, or topologically nontrivial systems, where new forms of response behavior may emerge from the same foundational principles.

Chapter 2

Bounds and anomalies of inhomogeneous anomalous Hall effects

It is well recognized that interpreting transport experiment results can be challenging when the samples being measured are spatially nonuniform. However, quantitative understanding on the differences between measured and actual transport coefficients, especially the Hall effects, in inhomogeneous systems is lacking. In this work we use homogenization theory to find exact bounds of the measured or homogenized anomalous Hall conductivity (AHC) in inhomogeneous conductors under minimal assumptions. In particular, we prove that the homogenized AHC cannot exceed the bounds of the local AHC. However, in common experimental setups, anomalies that *appear* to violate the above bounds can occur, with a popular example being the "humps" or "dips" of the Hall hysteresis curves usually ascribed to the topological Hall effect (THE). We give two examples showing how such apparent anomalies could be caused by different types of inhomogeneities and discuss their relevance in experiments.

An experimental setup is shown in Fig. 2.1. To measure the resistivity tensor, current is first injected along the $+x$ axis while the Hall voltage is recorded across the contacts along the y axis. The procedure is then repeated with current driven vertically along the y axis and the voltage measured laterally along the x axis. From these measurements, all components of the resistivity tensor are obtained via $\rho_{ij} = \Delta V_i / I_j$, and the conductivity is determined by matrix inversion, $\sigma = \rho^{-1}$. To acquire hysteresis loops, an out-of-plane magnetic field is applied to saturate the magnetization and then slowly swept between positive and negative values and back, tracing out the hysteresis loop while measuring the Hall conductivity.

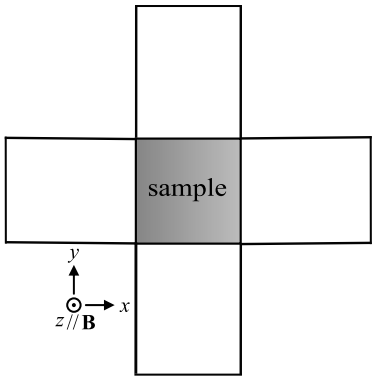

Figure 2.1: Example experimental setup for measuring all components of conductivity. The sample is placed between four conductive leads. Current is first driven along the $+x$ direction, while the voltage drop is recorded between contacts along the y axis. The procedure is then repeated with current applied along the y direction and the voltage measured between contacts along the x axis. These measurements yield the components of the resistivity tensor ρ_{ij}, from which the conductivity tensor is obtained via $\sigma = \rho^{-1}$. This procedure is repeated as the magnetic field is swept from $+z$ to $-z$ and back, tracing out the hysteresis loop.

2.1 Introduction

Transport experiments are usually performed using macroscopic or mesoscopic samples that have unavoidable spatial inhomogeneities. Inhomogeneities on the scale much larger than the mean free path of the microscopic quasiparticles can be described by classical transport equations with spatially varying coefficients. The effective transport coefficients measured experimentally by probes located at the sample boundary or in the interior but separated by macroscopic distances [3] are, however, not trivially determined by the local ones through a simple spatial average [4]. In certain cases the mesoscopic spatial inhomogeneity may lead to dramatic consequences not expected from the local physics. A prominent example is the classical inhomogeneity-induced non-saturating magnetoresistance [5, 6] proposed to explain the experimental observation in silver chalcogenides [7].

Another anomaly in transport experiments that has attracted significant interest recently is the hump or dip features in Hall resistivity versus magnetic field curves [8–18, 18–58], usually observed in magnetic conductors lacking spatial inversion symmetry either in the bulk or due to the presence of interfaces. A physically appealing picture of such anomalies is that finite magnetic fields stabilize an intermediate skyrmion phase in inversion-symmetry-breaking systems [59]. It

has been well established that conduction electrons coupled to skyrmion magnetic textures experience an emergent magnetic field and consequently have an extra Hall effect contribution, now known as the topological Hall effect (THE) [60–64]. The THE in the intermediate skyrmion phase therefore serves as a straightforward explanation for the anomalies [64]. However, such an interpretation, particularly when there is no complementing evidence from other experimental probes, has been seriously challenged in recent years [40–42, 46, 47, 65–72]. Among the alternative mechanisms, a widely accepted one is that superposition of anomalous Hall effect (AHE) [60, 73–83] hysteresis loops coming from subsystems with distinct magnetic (e.g. coercive fields) or transport (e.g. signs of the AHE) properties in the measured samples can lead to similar hump or dip features [37, 65–70, 84–86]. Effectively such a superposition is equivalent to performing a simple spatial average of the AHE. However, since the anomalies of the Hall signal occur near magnetization reversal which is a first-order phase transition, inhomogeneities due to formation of magnetic domains are prevalent. It is not clear if the measured anomalous Hall signals in an inhomogeneous magnetic conductor are always equivalent to such a spatial average. Moreover, the assumption of subsystems with individually well-defined coercive fields may be overly stringent [26].

In the above context, it is desirable if one can constrain the measured Hall coefficients, especially the anomalous Hall conductivities (AHC), in inhomogeneous systems without assuming particular mechanisms, so that influences due to inhomogeneities only may be isolated. Theoretical bounds of AHC of nonuniform systems can also be a useful diagnostic tool for uncovering details of inhomogeneities by standard transport experiments. Exact results of such type are, however, relatively scarce in the physics literature (see e.g. [87, 88] and references therein), possibly due to the general complexity of inhomogeneous transport problems and to the lack of experimental techniques for accurately characterizing inhomogeneity.

In this section, we use homogenization theory, a topical field in partial differential equations (PDE), to study the bounds and anomalies of the measured AHE in inhomogeneous quasi-two-dimensional systems. This is enabled by assuming the system has well-defined local conductivities determined by microscopic electronic structure details, so that classical transport equations are

applicable and the inhomogeneities are encoded in the spatially varying transport coefficients. We have first given exact bounds of the homogenized AHC in systems with both inhomogeneous longitudinal and Hall conductivities. The insights from this exact result further guide us to propose two inhomogeneity-related mechanisms that can lead to the hump/dip features in Hall hysteresis loops.

2.2 Bounds of the homogenized AHC

We consider the following set of equations governing classical electric transport in 2D:

$$\nabla \cdot (\boldsymbol{\sigma} \cdot \mathbf{E}) = 0,\ \nabla \times \mathbf{E} = 0, \tag{2.1}$$

where

$$\boldsymbol{\sigma} = \begin{pmatrix} \sigma_{xx} & \sigma_{xy} \\ \sigma_{yx} & \sigma_{yy} \end{pmatrix} \tag{2.2}$$

is the 2D conductivity tensor varying with position $\mathbf{r} = (x, y)$. The Hall conductivity σ_{h} is the antisymmetric part of $\boldsymbol{\sigma}$, i.e., $\sigma_{\mathrm{h}} \equiv (\sigma_{yx} - \sigma_{xy})/2$, and is due to either external magnetic fields (ordinary Hall effect) or spontaneous time-reversal-symmetry breaking (anomalous Hall effect). In this work we consider the latter only. σ_{h} is therefore odd under the reversal of the magnetic order parameter that breaks time-reversal symmetry, and fluctuates between positive and negative values in the presence of magnetic domains.

The boundary condition is chosen so that the spatial average of $\mathbf{E}$ is equal to that of the externally applied electric field $\mathbf{E}_0$, i.e., $\langle \mathbf{E} \rangle \equiv \frac{1}{A} \int d^2\mathbf{r}\mathbf{E} = \mathbf{E}_0$, A being the sample area. The homogenized conductivity $\bar{\boldsymbol{\sigma}}$ focused on in this work is defined through the spatial average of the electric current density $\mathbf{j}$ satisfying

$$\langle \mathbf{j} \rangle = \langle \boldsymbol{\sigma} \cdot \mathbf{E} \rangle \equiv \bar{\boldsymbol{\sigma}} \cdot \langle \mathbf{E} \rangle = \bar{\boldsymbol{\sigma}} \cdot \mathbf{E}_0. \tag{2.3}$$

To get some feel of the problem we start from the simplest case when $\sigma_{xx} = \sigma_{yy} \equiv \sigma_0$, $\sigma_{yx} = -\sigma_{xy} = \sigma_{\rm h}(\mathbf{r})$, and $|\sigma_{\rm h}(\mathbf{r})| = \sigma_{\rm h}$. Namely, only the AHC fluctuates between $\pm\sigma_{\rm h}$ spatially according to the magnetic domain profile. Bounds of $\bar{\sigma}_{\rm h}$ in this case can be obtained by first transforming $\boldsymbol{\sigma}$ to an isotropic tensor $\boldsymbol{\sigma}'$ using the duality transformation [89–93], and then applying the Hashin-Shtrikman bounds for 2-phase isotropic composites [88, 94]

$$\frac{\bar{\sigma}_{\rm h}}{\sigma_{\rm h}} \in \left[-1 + \frac{2p\sigma_0^2}{\sigma_0^2 + (1-p)^2\sigma_{\rm h}^2},\ 1 - \frac{2(1-p)\sigma_0^2}{\sigma_0^2 + p^2\sigma_{\rm h}^2}\right] \tag{2.4}$$

where p is the area percentage of domains with $\sigma_{\rm h}(\mathbf{r}) = \sigma_{\rm h}$. The two bounds are realized by domain configurations of packed coated circular cells with the same core/shell ratio [88]. Moreover, one can see that the absolute value of $\bar{\sigma}_{\rm h}$ can never exceed $\sigma_{\rm h}$. The two bounds reduce to the trivial spatial-average value $\langle\sigma_{\rm h}(\mathbf{r})\rangle = (2p-1)\sigma_{\rm h}$ when $\sigma_{\rm h}/\sigma_0 \to 0$.

Can $\bar{\sigma}_{\rm h}$ exceed the bounds of local $\sigma_{\rm h}$ when the longitudinal conductivity is inhomogeneous and in particular has a nonzero correlation with $\sigma_{\rm h}$? A simpler version of the problem can be obtained by replacing σ_0 by σ_1 (σ_2) in domains with $\sigma_{\rm h}(\mathbf{r}) = \sigma_{\rm h}$ ($-\sigma_{\rm h}$). Such a situation could happen during a magnetization reversal, when individual domains first nucleate at the regions with lower conductivities or more defects (see below). Note the values of $\sigma_{\rm h}(\mathbf{r})$ can be either positive- or negative-correlated with the longitudinal conductivity, depending on the material and on which half of the hysteresis loop is under consideration. The bounds of $\bar{\sigma}_{\rm h}$ in this case can be obtained using the same approach as

$$\begin{aligned}\frac{\bar{\sigma}_{\rm h}}{\sigma_{\rm h}} \in \Bigg[& -1 + \frac{8p\sigma_2^2}{[(1-p)\sigma_1 + (1+p)\sigma_2]^2 + 4(1-p)^2\sigma_{\rm h}^2}, \\ & 1 - \frac{8(1-p)\sigma_1^2}{[(2-p)\sigma_1 + p\sigma_2]^2 + 4p^2\sigma_{\rm h}^2}\Bigg].\end{aligned} \tag{2.5}$$

Different from Eq. (2.4), the above bounds can now exceed the spatial average $\langle\sigma_{\rm h}\rangle$, demonstrating the nontrivial consequences of correlation between longitudinal and Hall conductivities. However, they still cannot go beyond the maximum or minimum of $\sigma_{\rm h}$.

The above observations, plus numerical results not shown here, motivated us to speculate that the homogenized AHC is always bounded by the maximum and minimum of the local AHC. This indeed turns out to be the case as we prove below with minimal assumptions. To be precise, we consider $\boldsymbol{\sigma}(\mathbf{r}) = \boldsymbol{\sigma}_0(\mathbf{r}) + \sigma_{\mathrm{h}}(\mathbf{r})\mathbf{R}_\perp$, where $\boldsymbol{\sigma}_0(\mathbf{r})$ is a positive definite diagonal matrix with entries σ_{xx} and σ_{yy}, and $\mathbf{R}_\perp$ is the $\pi/2$ rotation matrix in 2D. $\boldsymbol{\sigma}_0$ and σ_{h} can be correlated or not, and do not have to vary smoothly with $\mathbf{r}$. The theorem below, whose proof is given in the supplemental material A.2, shows that in this case $\bar{\sigma}_{\mathrm{h}}$ is still bounded by the global minimum and maximum of $\sigma_{\mathrm{h}}(\mathbf{r})$:

Theorem 1. Suppose that σ_{xx}, σ_{yy} and σ_{h} are stationary ergodic random fields (see e.g. [95] for definitions) and that σ_{xx}, σ_{yy} are both bounded above and below by positive constants. Suppose additionally that

$$-\sigma_M \leq \sigma_{\mathrm{h}}(\mathbf{r}) \leq \sigma_M, \tag{2.6}$$

for some positive constant σ_M. Then, we have the inequality

$$-\sigma_M \leq \bar{\sigma}_{\mathrm{h}} \leq \sigma_M. \tag{2.7}$$

The above theorem is independent of physical mechanisms contributing to the local $\boldsymbol{\sigma}$ and suggests that in order for the measured AHC in the Hall hysteresis loop to exceed the values at saturation, the latter must not be the maximum/minimum of the local AHC when the anomalies appear, which includes the skyrmion scenario. Another potential cause of the anomalies is that the measured Hall signal is not $\bar{\sigma}_{\mathrm{h}}$. We provide examples for both possibilities associated with inhomogeneities below.

2.3 Anomalies due to nonuniform saturated AHC

In this section we discuss a possible mechanism for the anomalies when the spatial dependence of $\sigma_{\mathrm{h}}(\mathbf{r})$ is not only due to the magnetic domains. To this end we first give a recipe for modeling

magnetic domain evolution in field sweeps. As the perpendicular magnetic field sweeps, e.g., from negative to positive values, one expects the magnetic configuration to continuously evolve from a uniform negative magnetization, to spatially separated positive/negative-magnetization domains in a relatively narrow field range centered at the coercive field H_c, and finally to a uniform positive magnetization. This process can be qualitatively captured by the following function describing the spatial profile of normalized perpendicular magnetization

$$m(\mathbf{r}) = \mathrm{sgn}\left[\frac{H - H_c}{\epsilon_H} + M(\mathbf{r})\right] \tag{2.8}$$

where $\mathrm{sgn}(x) = 1$ (-1) when $x > 0$ $(x < 0)$, H is the perpendicular magnetic field, H_c is the coercive field, $M(\mathbf{r})$ is a smooth random field ranging from $M_{\min} < 0$ to $M_{\max} > 0$, and ϵ_H controls the abruptness of magnetic switching. For analytical convenience, below we replace $\mathrm{sgn}(x)$ by $\mathrm{erf}(x)$ where $\mathrm{erf}(x) = \frac{2}{\sqrt{\pi}}\int_0^x e^{-t^2}dt$ is the error function. Note that Eq. (2.8) gives infinitely sharp domain walls, while using the error function makes the domain wall width be determined by the $\mathbf{r}$ dependence of M.

If the inhomogeneity of $\sigma_{\mathrm{h}}(\mathbf{r})$ is only caused by magnetic domains, one can express it simply as $\sigma_{\mathrm{h}}(\mathbf{r}) = \sigma_{\mathrm{h}} m(\mathbf{r})$, where σ_{h} is the absolute value of the AHC in magnetically saturated states. However, in the presence of inhomogeneous material composition in real samples, even if the local magnetization in different spatial regions is the same, the local AHC does not have to have the same value or sign. This is particularly the case for nearly compensated ferrimagnets whose AHC changes sign across the compensation point [96–100]. To account for such an inhomogeneity, we generalize $\sigma_{\mathrm{h}}(\mathbf{r})$ to the following

$$\sigma_{\mathrm{h}}(\mathbf{r}) = \sigma_{\mathrm{h}}\left[1 + r_{\mathrm{h}} C(\mathbf{r})\right] m(\mathbf{r}) \tag{2.9}$$

where $C(\mathbf{r})$ (C stands for composition) is a zero-mean random field whose typical size is controlled by the dimensionless number $r_{\mathrm{h}} > 0$.

While $C(\mathbf{r})$ is in general distinct from $M(\mathbf{r})$, it is reasonable to expect them to have certain correlation, as already mentioned in the last section. For example, the energy barrier for locally nucleating a magnetic domain in an inhomogeneous sample is ultimately determined by the local material composition. Therefore regions where the local magnetization flips first during field sweeps should also have consistently larger/smaller AHC compared to the other regions. Similar correlation can also exist between local AHC and other local magnetic properties such as coercivity and saturation magnetization.

We now show that the correlation between $C(\mathbf{r})$ and $M(\mathbf{r})$ generally leads to hump/dip features in Hall hysteresis loops, which already manifests in the lowest order approximation of the homogenized conductivity $\bar{\sigma} \approx \langle\sigma\rangle$. Namely,

$$\bar{\sigma}_{\mathrm{h}} \approx \langle\sigma_{\mathrm{h}}(\mathbf{r})\rangle = \sigma_{\mathrm{h}} \left\langle (1 + r_{\mathrm{h}} C) \operatorname{erf}\left(\frac{H - H_c}{\epsilon_H} + M\right)\right\rangle \tag{2.10}$$

To proceed, we assume both C and M are zero-mean Gaussian random fields with unity variance and a nonzero covariance

$$\langle C^2\rangle = 1,\ \langle M^2\rangle = 1,\ \langle CM\rangle = \mathcal{V}_{CM} \tag{2.11}$$

where the fields in the angle brackets have the same position variable $\mathbf{r}$ and the covariance $\mathcal{V}_{CM}$ can be either positive or negative depending on the nature of the correlation. Eq. (2.10) can then be formally calculated using Wick's theorem in the appendix (A.1). However, before using the resulting formula to numerically evaluate $\langle\sigma_{\mathrm{h}}\rangle$, we derive some useful qualitative results first.

The extrema of $\langle\sigma_{\mathrm{h}}\rangle$ versus $\delta h \equiv \frac{H - H_c}{\epsilon_H}$ can be found by

$$0 = \frac{\partial\langle\sigma_{\mathrm{h}}\rangle}{\partial(\delta h)} \approx \frac{2}{\sqrt{\pi}}\sigma_{\mathrm{h}}\langle(1 + r_{\mathrm{h}} C)(1 - 2\delta h M - M^2)\rangle \tag{2.12}$$

which gives the critical values $\delta h_c = 0$. The resulting extremal value of $\langle \sigma_{\rm h} \rangle$ is

$$\langle \sigma_{\rm h} \rangle_c \approx \frac{2}{\sqrt{\pi}} \sigma_{\rm h} \langle (1 + r_{\rm h} C)(\delta h_c + M) \rangle = \frac{2}{\sqrt{\pi}} \sigma_{\rm h} r_{\rm h} \mathcal{V}_{CM} \tag{2.13}$$

whose absolute value can exceed $\sigma_{\rm h}$ if $r_{\rm h} |\mathcal{V}_{CM}| \gtrsim 0.89$. Since $|\mathcal{V}_{CM}|$ is expected to be less than 1, $r_{\rm h}$ should be on the order of 1 or larger. This means that the fluctuation of $\sigma_{\rm h}$ must be strong enough so that its sign can change spatially even in a uniform magnetic state.

The above qualitative picture is verified by Figure 2.2, which plots Eq. (2.10) versus H as well as its time reversal, amounting to $(H_c, M) \to (-H_c, -M)$. Note that the half of hysteresis loop with positive H_c corresponds to sweeping H from negative to positive values. A hump in the upsweeping curve therefore occurs when $\mathcal{V}_{CM} > 0$ [Fig. 2.2 (b)]. More intuitively, when $H \approx H_c > 0$, regions with $M > 0$ are positive domains nucleated within a negative magnetization background. The positive $\mathcal{V}_{CM}$ therefore means that regions with larger AHC are switched first. When a local coercive field can be approximately defined, it means regions with larger AHC have smaller coercive fields, as proposed in previous literature [65–68], but our theory applies to more general situations such as that in [26, 36].

2.4 Anomalies due to domain wall resistance

In this section we consider another possible cause of the anomalies, i.e., it is not the $\bar{\sigma}_{\rm h}$ that is actually measured. We also consider another complication that is not accounted for in Theorem 1, i.e., when $\boldsymbol{\sigma}(\mathbf{r})$ has symmetric off-diagonal components.

Experiments for Hall effects are usually performed using "Hall bar" devices, where the longitudinal currents flowing through the sample are externally controlled and are expected to be nearly uniform near the middle of the bar, and it is the voltage between transverse boundaries that is measured. Supposing one considers a system in the domain $x, y \in [0, 1]$, the above measurement

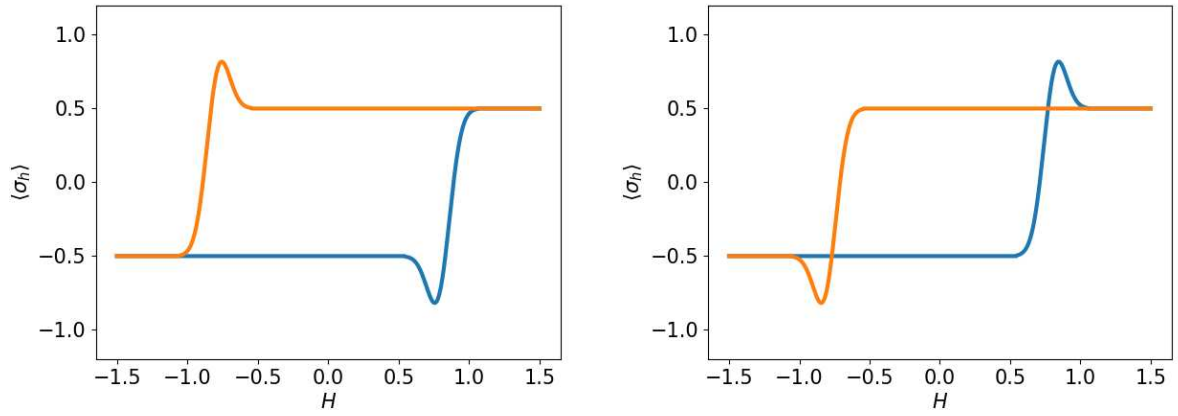

Figure 2.2: Dip (a) and hump (b) features due to nonuniform saturated values of $\sigma_{\rm h}$ correlated with magnetic domains, plotted using Eq. (2.10). The up-sweeping part of each loop is plotted using $\sigma_{\rm h} = 0.5$, $H_c = 0.8$, $\epsilon_H = 0.1$, $r_{\rm h} = 4$, $\mathcal{V}_{CM} = -0.7$ (a) and $\mathcal{V}_{CM} = 0.7$ (b), while the down-sweeping half is obtained by flipping the signs of H_c and $\mathcal{V}_{CM}$.

geometry can be described by the following boundary conditions:

$$\mathbf{j} \cdot \hat{n} = \begin{cases} -\sigma_0 E_0, & x = 0 \\ \sigma_0 E_0, & x = 1 \\ 0, & y = 0, 1 \end{cases} \tag{2.14}$$

where $\hat{n}$ is the unit normal vector of the boundary pointing to the exterior of the solution domain. The combination of $\sigma_0 E_0$ for specifying the longitudinal current I_x is introduced for later convenience. One can then obtain $R_{yx} = V_y/I_x$, where V_y is the voltage difference between top and bottom edges averaged over x. The Hall resistance is R_{yx} after antisymmetrization: $R_{\rm h} = (R_{yx} - \mathcal{T}[R_{yx}])/2$ where $\mathcal{T}$ means time reversal.

We solve the above problem for $R_{\rm h}$ by considering an anisotropic contribution to $\boldsymbol{\sigma}(\mathbf{r})$ from the magnetic domain walls, which prevail during the magnetization reversal. It is well known [101] that currents flowing parallel and perpendicular to a domain wall experience different resistivities.

Near a domain wall oriented along the y-axis, we can define the domain wall contribution to $\boldsymbol{\sigma}$ as

$$\boldsymbol{\sigma}_{\mathrm{DW}} = f(\mathbf{r}) \begin{pmatrix} \sigma_\perp & 0 \\ 0 & \sigma_\parallel \end{pmatrix} \tag{2.15}$$

where $\sigma_\perp$ ($\sigma_\parallel$) is the local change to the xx (yy) component of the conductivity tensor. Normally one expects $-\sigma_0 < \sigma_\perp < \sigma_\parallel < 0$. $f(\mathbf{r})$ is a positive scalar function that smoothly increases from 0 to 1 as one moves from domain interior to the wall. Using notations in the last section, we can, for example, choose

$$f(\mathbf{r}) = 1 - \mathrm{erf}^2 \left[\frac{1}{\epsilon_W} \left(\frac{H - H_c}{\epsilon_H} + M \right) \right] \tag{2.16}$$

where the new parameter ϵ_W controls the typical width of f variation relative to that of magnetization domain walls, since the spatial range in which $f(\mathbf{r})$ becomes significant does not have to be the same as that of the magnetization variation near a domain wall. We can then rotate Eq. (2.15) to describe arbitrarily oriented domain walls as

$$\boldsymbol{\sigma}_{\mathrm{DW}}(\mathbf{r}) = f(\mathbf{r}) R[\theta(\mathbf{r})] \begin{pmatrix} \sigma_\perp & 0 \\ 0 & \sigma_\parallel \end{pmatrix} R^{-1}[\theta(\mathbf{r})]$$

where $R[\theta(\mathbf{r})]$ is the 2D rotation matrix with the rotation angle θ a function of $\mathbf{r}$. $\theta(\mathbf{r})$ can be obtained from $f(\mathbf{r})$ since the gradient of f is perpendicular to the domain wall: $(\cos\theta, \sin\theta) = \frac{1}{|\nabla f|}(\partial_x f, \partial_y f)$.

We next solve the transport equations with the boundary condition Eq. (2.14), $\boldsymbol{\sigma}_{\mathrm{DW}}$ in Eq. (2.17), and Eq. (2.9) with $C = 0$ for $\sigma_{\mathrm{h}}(\mathbf{r})$. This is done numerically with FEniCS [102] and M generated as a 2D Gaussian random field in the unit square. The time reversal of R_{yx} for defining R_{h} corresponds to $(H, M, H_c) \to (-H, -M, -H_c)$ in our model.

Figure A.1 (a) plots the hysteresis loop $R_{\mathrm{h}}(H)$ obtained from the above numerical scheme. A distinct feature of the figures, different from Fig. 2.2, is that both a hump and a dip appear in a

single half of the hysteresis. Figure A.1 (b) shows the domain profile at the peak position of the up-sweeping curve, indicating that the correlation length ξ of the random field M is not very small compared to the solution domain. However, by further calculating configurations with $\xi \ll 1$, as exemplified by Fig. A.1 (d), the double hump/dip feature still survives [Fig. A.1 (c)], suggesting the domain wall mechanism is relevant even in the homogenization limit.

The origin of the double hump/dip feature in the homogenized Hall *resistance* can be understood from a heuristic perturbation calculation as follows. Up to the lowest nonzero order in $\sigma_{\rm h}(\mathbf{r})$, the solution of the transport equation is $\mathbf{E} \approx \mathbf{E}^{(0)} + \mathbf{E}^{(1)}$ where the superscript means the order in $\sigma_{\rm h}$. The spatial average of $\mathbf{j}(\mathbf{r})$ is then

$$\langle \mathbf{j} \rangle \approx \left\langle (\sigma_0 \mathbf{I} + \sigma_{\rm h} \mathbf{R}_\perp + \boldsymbol{\sigma}_{\rm DW}) \left(\mathbf{E}^{(0)} + \mathbf{E}^{(1)} \right) \right\rangle . \tag{2.17}$$

For simplicity we approximate $\langle AB \rangle \approx \langle A \rangle \langle B \rangle$, and consider the homogenization limit when $\langle \sigma_{\rm DW}^{xx} \rangle = \langle \sigma_{\rm DW}^{yy} \rangle \equiv \sigma_{\rm DW}$ and $\langle \sigma_{\rm DW}^{xy} \rangle = \langle \sigma_{\rm DW}^{yx} \rangle = 0$. The boundary condition $\langle j_x \rangle = j_0$, $\langle j_y \rangle = 0$ then leads to

$$\begin{aligned} (\sigma_0 + \sigma_{\rm DW}) \langle E_x^{(0)} + E_x^{(1)} \rangle - \langle \sigma_{\rm h} \rangle \langle E_y^{(1)} \rangle &= j_0 \\ (\sigma_0 + \sigma_{\rm DW}) \langle E_y^{(1)} \rangle + \langle \sigma_{\rm h} \rangle \langle E_x^{(0)} + E_x^{(1)} \rangle &= 0 \end{aligned} \tag{2.18}$$

from which we get the Hall resistivity

$$\bar{\rho}_{\rm h} \approx -\frac{\langle E_y^{(1)} \rangle}{j_0} = \frac{\langle \sigma_{\rm h} \rangle}{(\sigma_0 + \sigma_{\rm DW})^2 + \langle \sigma_{\rm h} \rangle^2} \tag{2.19}$$

consistent with that obtained by inverting the averaged conductivity tensor as expected. Compared to the saturated value $\rho_{\rm h} = \sigma_{\rm h}/(\sigma_0^2 + \sigma_{\rm h}^2)$, $\bar{\rho}_{\rm h}$ differs by a factor of $r_{\rm DW} \equiv \frac{\bar{\rho}_{\rm h}}{\rho_{\rm h}} \approx \frac{\langle \sigma_{\rm h} \rangle}{\sigma_{\rm h}} (1 - |\sigma_{\rm DW}|/\sigma_0)^{-2}$, assuming the Hall conductivities are negligible compared to the longitudinal ones. $r_{\rm DW}$ is always positive when $\langle \sigma_{\rm h} \rangle$ has the same sign as the saturated value $\sigma_{\rm h}$. Therefore both a hump and a dip will appear simultaneously in either half of the hysteresis loop when $r_{\rm DW} > 1$,

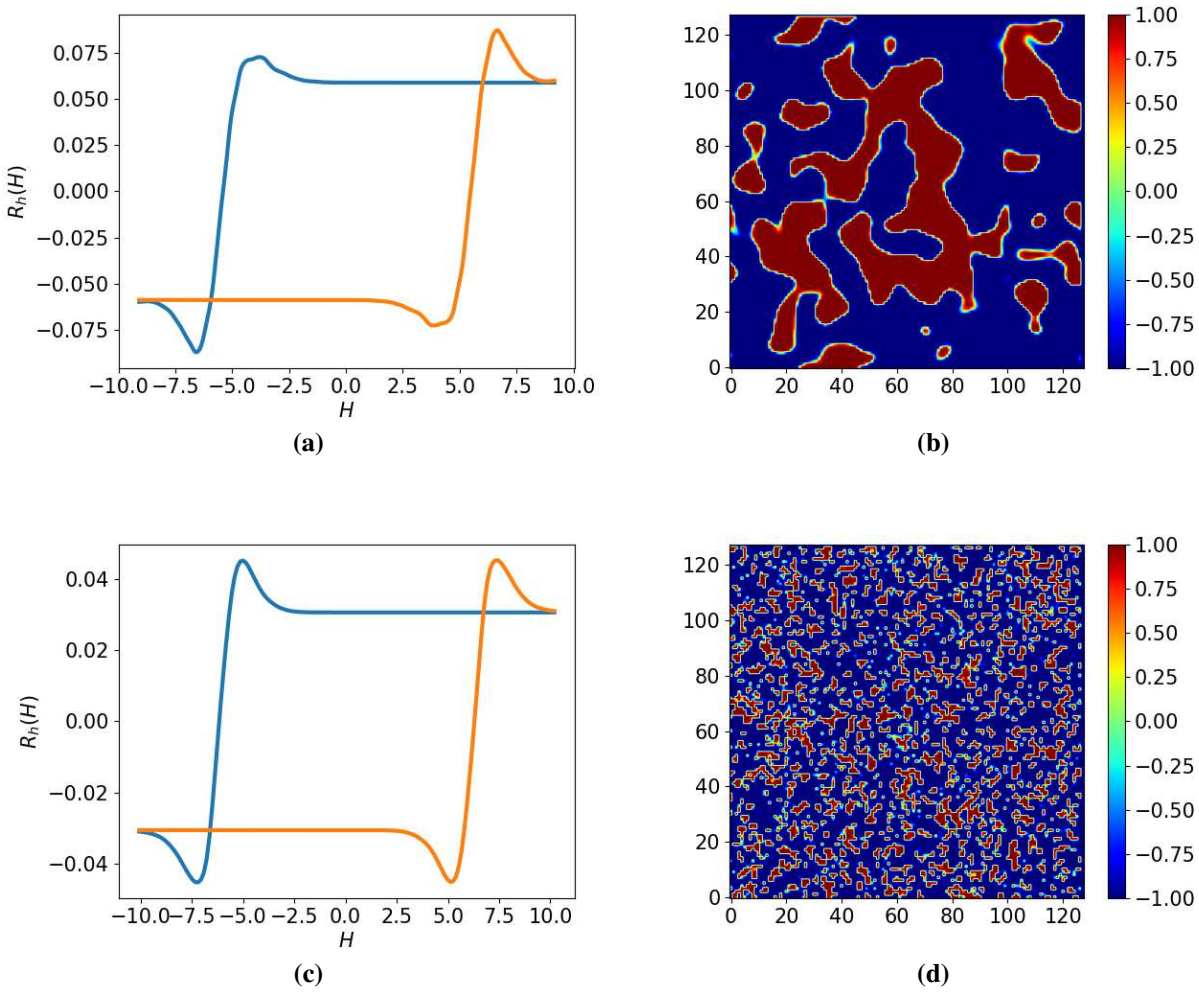

Figure 2.3: (a, c) Hysteresis loops with humps/dips induced by the domain wall resistance mechanism, calculated using $\xi = 3 \times 10^{-2}, |H_c| = 5.0$ (a) and $\xi = 2 \times 10^{-3}$, $|H_c| = 3.6$ (c), respectively, and a mesh size of 128×128. (b, d) Domain configurations $m(\mathbf{r})$ at the peaks of up-sweeping curves in (a) and (c), respectively. The other parameter values are: $\sigma_{\rm h} = 0.07, \sigma_\perp = -0.8, \sigma_\parallel = -0.4, \epsilon_W = 10$, $\sigma_0 = E_0 = \epsilon_H = 1$.

or equivalently $\frac{\langle\sigma_{xx}\rangle}{\sigma_0} < \sqrt{\frac{\langle\sigma_{\rm h}\rangle}{\sigma_{\rm h}}}$, at certain values of $H - H_c$. Since $\frac{\langle\sigma_{xx}\rangle}{\sigma_0}$ grows quadratically with $H - H_c$ near H_c, while $\frac{\langle\sigma_{\rm h}\rangle}{\sigma_{\rm h}}$ increases linearly with $H - H_c$, the inequality always holds when $\frac{\langle\sigma_{xx}\rangle(H_c)}{\sigma_0} \to 0$, i.e., when the longitudinal conductivity is strongly suppressed by the presence of domain walls.

The coexistance of hump/dip in a single half of the hysteresis loop, together with abnormally large magnetoresistance near the magnetic switching, are strong indicators of our domain wall mechanism. Such a scenario has been briefly discussed in [35], where the difference between $\bar{\rho}_{\rm h}$ and $\bar{\sigma}_{\rm h}$ is also emphasized. The double hump/dip features due to the domain wall mechanism can be very similar to that caused by the THE when the coercive field is negligible. In such cases the field dependence of the longitudinal resistance is essential for distinguishing the two.

Finally, as shown in the appendix (A.4), we have consistently observed that the Hall conductance, obtained by first inverting the resistance tensor and then antisymmetrizing the off-diagonal part, is always bounded by the saturated values in the homogenization limit [35]. This strongly suggests that the conclusion of Theorem 1 still holds when the conductivity tensor has spatially dependent anisotropy.

2.5 Discussion

In this work we have given exact bounds of the AHC in nonuniform systems that satisfy the classical transport equation with spatially varying coefficients. As a result, it also incorporates quantum effects as long as their contribution can be described as a local conductivity tensor, such as the THE as mentioned previously. Therefore our formalism can in principle be generalized to include other interesting quantum effects such as domain wall modes in Weyl semimetals, integer or fractional Chern insulators, etc., and to study their consequences in the presence of various mesoscopic inhomogeneities. Our study also calls for the need of developing transport techniques that can characterize the extent of inhomogeneity and allow for comparison with a full solution of the transport problem in a given system. This is in the same line as recent experiments in

disentangling domain wall vs. bulk contributions to the Hall conductivity in quantum anomalous Hall systems [103, 104].

Chapter 3

Spin relaxation: Dipolar Field Model

Strategies for slowing magnetic relaxation via local environmental design are vital for developing next-generation spin-based technologies (e.g. quantum information processing). Herein we demonstrate a new technique to do so via chemical design of a local magnetic environment. We show that embedding the open-shell complex $(Ph_4P)_2[Co(SPh)_4]$ in solid-state matrices of the isostructural, open-shell species $(Ph_4P)_2[M(SPh)_4]$ (M = Ni^{2+}, S = 1; M = Fe^{2+}, S = 2; M = Mn^{2+}, $S = {}^5/_2$) will slow magnetic relaxation for the embedded $[Co(SPh)_4]^{2-}$ ion by three orders of magnitude. Magnetometry, EPR, and computational analyses reveal that integer spin and large, positive zero field splitting (D) values for the diluent produce a quiet local magnetic field. As a result, these matrices enable slower relaxation rates. Embedding complexes into diamagnetic environments is well-established for slowing relaxation. Herein we, in contrast, slow magnetic relaxation via embedding in a spin-abundant environment.

The unifying framework for this investigation is *linear response theory*, a foundational tool in condensed matter physics used to predict how systems near equilibrium respond to weak external perturbations. While thermodynamic quantities offer susceptibility via differentiation, they are inherently coarse-grained and obscure spatial structure and dynamical behavior. However, since such quantities are accessible in experiments, it is essential to develop a theoretical framework that connects them to the underlying microscopic dynamics.

At its core, linear response theory relates equilibrium correlation functions of conserved quantities to nonequilibrium responses such as currents, polarizations, and accumulated densities. To describe the linear response of an observable $X_i(\mathbf{r}, r)$ to a weak external perturbation $F'_j(\mathbf{r}', t')$ applied in the past, we write,

$$X_i(\mathbf{r}, t) = \int dt' \int d^d r' \chi_{ij}(\mathbf{r}, t; \mathbf{r}', t') F'_j(\mathbf{r}', t') + \mathcal{O}(F_j^2) \tag{3.1}$$

Here, χ_{ij} is the response function characterizing the influence of the perturbation spacetime point $(\mathbf{r}', t')$ on the observable at $(\mathbf{r}, t)$. This framework captures the causal, linear dependence of system observables on external forces that drive the system out of equilibrium. Retaining only the first term in Eq. (3.1) is typically justified, as external forces are generally much weaker than the internal interactions governing the system.

3.0.1 Symmetries and Constraints

The response function is subject to several fundamental constraints. A key one is causality: a generalized force $F_j'(t')$ cannot influence the system before it is applied. This implies the response function must vanish for earlier times, i.e., $\chi_{ij}(\mathbf{r}, \mathbf{r}'; t, t') = 0$ for $t < t'$. We refer to such a response as retarded.

For Hamiltonians that are explicitly not a function of time, the response depends only on the time difference, $\chi_{ij}(\mathbf{r}, \mathbf{r}'; t, t') = \chi_{ij}(\mathbf{r}, \mathbf{r}'; t - t')$. This time-translation invariance allows a simplification via Fourier transformation. Defining the Fourier transform of the observable response $X(\mathbf{r}, \omega)$ as

$$\begin{aligned} X(\mathbf{r}, \omega) &\equiv \int dt\, e^{-i\omega t} X(\mathbf{r}, t) \\ &= \int d^d r' \int dt' \int dt\, e^{-i\omega t} \chi_{ij}(\mathbf{r}, \mathbf{r}'; t - t') F_j'(\mathbf{r}', t') \end{aligned} \tag{3.2}$$

replacing $t - t' = \tau \to dt = d\tau$,

$$\begin{aligned} X(\mathbf{r}, \omega) &= \int d^d r' \int dt' e^{-i\omega t'} \left(\int d\tau\, e^{-i\omega \tau} \chi_{ij}(\mathbf{r}, \mathbf{r}'; \tau) \right) F_j'(\mathbf{r}', t') \\ &= \int d^d r' \chi_{ij}(\mathbf{r}, \mathbf{r}'; \omega) \left(\int dt' e^{-i\omega t'} F_j'(\mathbf{r}', t') \right) \\ &= \int d^d r' \chi_{ij}(\mathbf{r}, \mathbf{r}'; \omega) F_j'(\mathbf{r}', \omega). \end{aligned} \tag{3.3}$$

An immediate consequence is that an external force oscillating at frequency ω induces a response at the same frequency, reflecting the linearity and time-translation invariance of the system.

Another important symmetry to explore is that of translational invariance. Applying the same reasoning as the previous paragraph, we obtain

$$X(\mathbf{q},\omega) \equiv \int d^d r\, e^{-i\mathbf{q}\cdot\mathbf{r}} X(\mathbf{r},\omega) = \chi_{ij}(\mathbf{q};\omega) F'_j(\mathbf{q},\omega) \tag{3.4}$$

This relation shows that $X(\mathbf{q},\omega)$ corresponds to the system's response to a perturbation of frequency ω, with a wave vector $\mathbf{q}$.

Another symmetry is that of Time-Reversal symmetry. The constraint is if the unperturbed system is invariant under time-reversal, this symmetry can impose relations on the response functions. For example, the conductivity tensor σ_{ij} satisfies $\sigma_{ij}(B) = \sigma_{ji}(-B)$ under time reversal with a magnetic field B.

The response function must yield real observable quantities and obey second law of thermodynamics. This implies that the imaginary part of the response function that is related to dissipation must be positive definite, e.g., Im[$\chi \geq 0$].

Suppose we have a time dependent Hamiltonian:

$$H(t) = H_0 + H'(t), \tag{3.5}$$

where H_0 is the unperturbed Hamiltonian, and $H'(t)$ is a small time dependent perturbation of the form:

$$H_{\mathrm{F}}(t) = \int d^d r F'_j(\mathbf{r},t) \hat{X}_j(\mathbf{r}). \tag{3.6}$$

Here the coefficients $F'_j(\mathbf{r},t)$ are called the generalized "forces" who represent a perturbation that couples to the system through some operator$\hat{X}$, for example $F'(\mathbf{r},t)$ could correspond to the electric field, and $\hat{X}$ could represent charge or density operator.

Suppose we want to find the expectation value of some operator $\hat{Y}$. To first order in the perturbation, this is given by Eq. 3.1. In the interaction picture, the time evolution of the density matrix

$\rho_I(t)$ is:

$$\frac{d\rho_i(t)}{dt} = -\frac{i}{\hbar}\left[H'_I(t), \rho_I(t)\right] \tag{3.7}$$

To first order in H', this gives, with $\rho_I(t) = \rho_0 + \rho'(t)$:

$$\rho_I(t) = \rho_0 - \frac{i}{\hbar}\int_{-\infty}^{t} dt'[H'_I(t'), \rho_0], \tag{3.8}$$

where $\rho_0 = e^{-\beta H_0}/Z$ is the equilibrium density matrix.

Then the expectation value of $\hat{Y}$ becomes:

$$\left\langle \hat{Y}_i(\mathbf{r}, t)\right\rangle = \text{Tr}\left[\rho_I(t)\hat{Y}_{i,I}(\mathbf{r}, t)\right], \tag{3.9}$$

Inserting this into the expansion for $\rho_I(t)$:

$$\delta\left\langle \hat{Y}_i(\mathbf{r}, t)\right\rangle = -\frac{i}{\hbar}\int_{-\infty}^{t}\int d^d r' F_j(\mathbf{r}', t')\left\langle\left[\hat{Y}_i(\mathbf{r}, t), \hat{X}_j(\mathbf{r}', t')\right]\right\rangle_0 \tag{3.10}$$

Where $\langle\cdots\rangle_0$ means expectation in equilibrium. This then gives us the form of the response function, including causality we get:

$$\chi_{ij}(\mathbf{r} - \mathbf{r}', t - t') = \frac{i}{\hbar}\theta(t - t')\left\langle\left[\hat{Y}_i(\mathbf{r}, t), \hat{X}_j(\mathbf{r}', t')\right]\right\rangle_0 \tag{3.11}$$

which is known as the Kubo formula. This expresses that the response of an observable to an external perturbation is governed by the system's equilibrium fluctuations. It quantifies the sensitivity of an observable $\hat{Y}(\mathbf{r}, t)$ to a perturbation $X_j(\mathbf{r}', t')$ applied at an earlier time.

Having established the framework of linear response theory, we now turn to its application in understanding spin relaxation phenomena. Relaxation processes determine how long a spin system retains nonequilibrium polarization, directly impacting technologies ranging from molecular qubits to spintronic memory devices. While many treatments emphasize spin–orbit–mediated channels, recent work highlights that dipolar interactions between localized spins can serve as a dominant

relaxation pathway, especially in molecular and insulating systems. In the following section, we introduce the dipolar field model of spin relaxation and show how the linear response formalism provides both conceptual clarity and quantitative access to relaxation rates in experimentally relevant systems.

In the following, the experimental work was done by Ian Mosely, and Joe Zadrozny.

3.1 Introduction

Single-molecule magnets are potential next-generation components in information storage and processing, [105–107] spintronics [108], and magnetic resonance imaging [109]. These complexes display an activation energy barrier (U) to reorientation of the magnetic moment that can induce extremely long magnetic relaxation times ($>$ 1s) at low temperature [110–116]. Environmental spins (which constitute the "spin bath") frequently induce rapid relaxation through dipolar interactions, and nearly all envisioned applications of single molecule magnets involve the existence of a spin bath in some form (e.g. high-density arrays of open-shell molecules on surfaces or ^{1}H nuclear-spin-rich aqueous environments) [117]. Hence, developing new ways to study, understand, and chemically control the impact of the spin bath is vital to eventual application.

At low temperatures, the spin bath of a metal ion hastens relaxation by enhancing quantum tunneling of the magnetization [118]. In this process, a single-molecule magnet's spin will flip and undercut the barrier [119]. Tunneling in these systems is driven by electronic dipolar interactions with adjacent molecules and can be disrupted by diamagnetic dilution [105]. Diamagnetic dilution is achieved by taking a magnetic molecule and either (1) dissolving it into an organic solvent or matrix (as was done for $Mn_{12}O_{12}$) [120, 121], or (2) cocrystallizing with a structurally analogous, closed-shell species. For example, mononuclear M^{2+} complexes can be diluted with Zn^{2+} [122] or low-spin Ni^{2+} analogues [123], M^{3+} species can be diluted with low-spin Co^{3+} [124], Y^{3+} [125, 126], or Ga^{3+} [127], and M^{4+} species can be diluted with Ti^{4+} [128]. In these dilute systems, wherein the potential size advantage of molecular information storage is lost, magnetic relaxation is often slowed by orders of magnitude. It is vital to deviate away from these

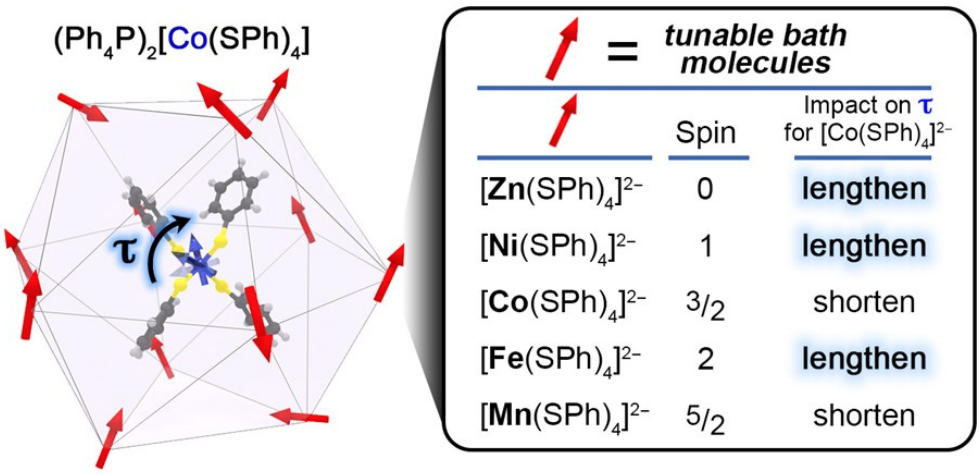

Figure 3.1: (left) The local environment of $[Co(SPh)_4]^{2-}$ in crystals of pure $(Ph_4P)_2[Co(SPh)_4]$ (Co) is rich in high-spin Co(II) ions. (right) We show via chemical control of the spin bath that certain paramagnetic diluents are able to lengthen magnetic relaxation times (τ) analogous to nonmagnetic molecules.

magnetically quiet confines to discover how to slow relaxation rates when the environment is noisy. Thus, it is necessary to develop new, chemical means of modifying the local magnetic environment for studying magnetic relaxation.

Herein, we illustrate a new way of chemically manipulating relaxation through a synthetically tunable *paramagnetic* matrix and the technique of *paramagnetic dilution*. Importantly, we use this method to show that select $S = 1$ and $S = 2$ ions can produce a spin bath that suppresses tunneling similar to a bath of closed-shell Zn^{2+}. This work focuses on the mononuclear single-molecule magnet $[Co(SPh)_4]^{2-}$ Fig. (3.1), which demonstrates facile quantum tunneling at low temperature [122]. We measured the magnetization dynamics of dilutions of $(Ph_4P)_2[Co(SPh)_4]$ (Co, $S = {}^3/_2$) in the paramagnetic diluents $(Ph_4P)_2[Ni(SPh)_4]$ (Ni, $S = 1$), $(Ph_4P)_2[Fe(SPh)_4]$ (Fe, $S = 2$), $(Ph_4P)_2[Mn(SPh)_4]$ (Mn, $S = {}^5/_2$), and the diamagnetic diluent $(Ph_4P)_2[Zn(SPh)_4]$ (Zn, $S = 0$). These data reveal an exciting disruption of tunneling for baths of $S = 1$ Ni and $S = 2$ Fe, similar to the effects observed for the traditional diamagnetic diluent S = 0 Zn. On the basis of EPR, susceptibility, and theoretical modeling data, we correlate the viability of the $S = 1$ Ni and $S = 2$ Fe diluents with the positive zero field splitting (D) of these species. This feature, we propose, makes them effective-spin zero ($S_{eff} = 0$) at low temperature despite possessing multiple unpaired

electrons and effectively quiets the local dipolar fields that hasten relaxation [129, 130]. Whereas most dilutions of single-molecule magnets exploit strictly diamagnetic environments, this study is, to the best of our knowledge, the first to explicitly target magnetically concentrated diluting conditions.

3.2 Results / Discussion

3.2.1 Synthesis

The following section presents work carried out by Ian Mosely and Joe Zadrozny. The $(Ph_4P)_2[M(SPh)_4]$ species (M = Mn, Fe, Co, Ni, and Zn), denoted **Mn**, **Fe**, **Co**, **Ni**, and **Zn,** are isostructural mononuclear complexes [131, 132]. A tetragonal distortion in the tetrahedral MS_4 unit of these complexes makes the local symmetry D_{2d} and engenders an extreme magnetic anisotropy and slow magnetic relaxation for **Co** [133]. A slight change is observed in the average M–S distances as a function of M 2.328(4) for **Co** [132], 2.288(4) for **Ni** [131], 2.356(6) for **Fe** [132], 2.442(3) for **Mn**, and 2.352(3) Å for **Zn** [134], but all crystallize in the $Pbc2_1$ space group. Furthermore, the same tetragonal distortion toward D_{2d} symmetry is seen in all $[M(SPh)_4]^{2-}$ units. Finally, each metal ion has 12 nearest neighbors, with closest MM distances of around 10.456(7) Å (Fig. 3.1) [129, 132].

Multiple sets of solid solutions of **Co** in **Ni**, **Fe**, **Mn**, and **Zn** were made to test the impact of paramagnetic spin baths on magnetic relaxation of **Co**. First, we prepared variable-concentrations of **Co** in **Ni** (73%, 58%, 25%, 9%, and 3% **Co** relative to **Ni**). Second, we prepared dilutions of **Co** in **Fe** (83%, 57%, 24%, 16%, and 6% **Co** to **Fe**). Third, dilutions of **Co** in **Mn** (81% and 43% **Co** to **Mn**) and finally, dilutions of **Co** in **Zn** (30% and 3% **Co** to **Zn**). PXRD demonstrates that these dilutions assume the same crystalline phases of their pure components, and preliminary energy dispersive X-ray spectroscopy (EDS) data suggests homogeneous distribution over μm-length scales Fig. S1, S2 [135, 136].

3.2.2 DC Susceptibility

Magnetic analyses via direct-current (dc) magnetic susceptibility ($\chi_M T$) measurements indicate that Co, Ni, Fe, and Mn are isolated spin systems with varying magnetic anisotropies. Room-temperature (300 K) $\chi_M T$ values of 2.45, 1.34, 2.90, and 4.56 cm^3K/mol for Co, Ni, Fe, and Mn (Fig. S3), indicate $S = {}^3/_2$, 1, 2, and ${}^5/_2$ metal ions, respectively, matching previous results [137]. With decreasing temperature, $\chi_M T$ decreases, most dramatically for Ni, somewhat less for Co and Fe, and almost negligibly for Mn, decreases likely attributable to zero-field splitting. The $\chi_M T$ data were fit with a spin Hamiltonian accounting for zero-field splitting (using the program PHI34 – see SI for fitting details). The final extracted D values are $D \approx$ –61 for Co, D = +68 cm^{-1} for Ni, D = +5.85 cm^{-1} for Fe, and D = -0.12 cm^{-1} for Mn, all values are in keeping with previous reports for other similar, 4-coordinate MS_4 complexes [138–141].

3.2.3 High-Field, High-Frequency EPR (HF-EPR)

Electron paramagnetic resonance (EPR) measurements were pursued to better quantitate the zero-field splitting for **Mn**, **Fe**, and **Ni** (Figs. 3.2.3) Fig. S4-S7 [136], as dc susceptibility can sometimes incorrectly assign the signs/magnitudes of these parameters. [142] High-field and high-frequency EPR (HF-EPR) analyses of **Co** were previously reported and generally agree with the large, negative D obtained from dc susceptibility fits [133]. For **Ni** and **Fe**, which also appeared by $\chi_M T$ to have large D values, we used high-field (up to 17 T) and high-frequency analyses (up to 650 GHz). For **Mn**, which signaled a small D in the $\chi_M T$ analyses, we employed X-band (9.838 GHz) analyses augmented by one high-frequency (381 GHz) (Fig. S7 [136]) spectrum. **Mn** revealed an X-band spectrum with 6 broad peaks while only 5 peaks were observed at 381 GHz (Fig S4-S6 [136]). For **Fe**, a highly frequency- and temperature-dependent EPR spectrum was observed, with multiple sharp peaks detected at all frequencies (Fig. 3.2.3)(Fig. S4-S6 [136]). In contrast, no EPR signal was observed for **Ni** from 0 to 17 T and frequencies up to 650 GHz.

The EPR spectra generally agree with the susceptibility analyses and were simulated with Easyspin40 and the program*SPIN*, see [136] for full details. First, for S = 1 **Ni** with a D of ca.

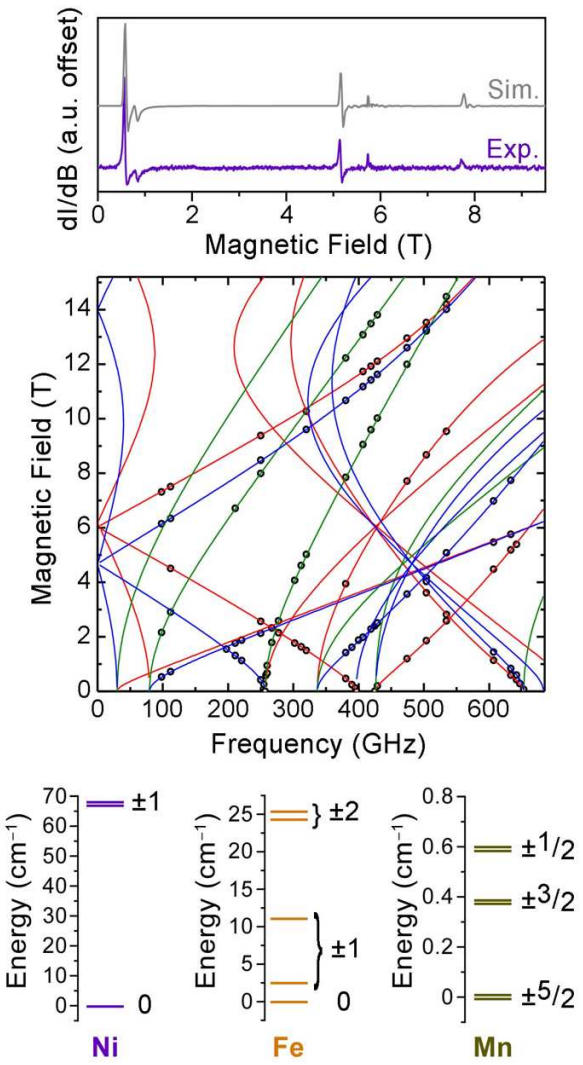

Figure 3.2: Top:633 Ghz EPR spectra for a powder of **Fe** collected at 20 K. See SI for experimental and simulation details. **Middle:** Field versus frequency dependence of the EPR translations for **Fe**. Each circle represents a transition observed at that field and frequency. Green, blue, and red lines were calculated with **Fe** x, y, and z

+67 cm^{-1}, we observed, as expected, no EPR signal under the experimental fields and frequencies. Second, for **Fe** (S = 2), relatively sharp, well resolved peaks were observed, and the frequency/field dependence of these peaks can be convincingly modeled with D = +5.848(1) cm^{-1}, and E = +1.428(1) cm^{-1}, in general agreement with other lower-frequency EPR analyses (Fig. 3.2.3) [143–145]. Finally, for **Mn**, simulations of the X-band and 381 GHz spectra produce average D and E values of -0.11 cm^{-1}, and -0.024 cm^{-1}, respectively, close to the small values from $\chi_M T$ simulations (Fig. S7) and the general expectations for an Mn^{2+} ion [146–148].

Modeling the HF-EPR spectra of **Fe** and **Mn** was attempted for both positive and negative values of the anisotropy parameters (D and E). The models for **Fe** obtained when $D > 0$ resulted in significant improvements over the model with $D < 0$ (Fig. S7 [136]). In the case of **Mn**, which possesses a much smaller ZFS, the simulations of the X-band and HF-EPR spectra were of generally equal quality with negative or positive D.

Together, the susceptibility and EPR data highlight an important varying aspect of the different bath spins, beyond just S: the ground-state M_S values (Fig. 3.2.3). The large positive D for Ni suggests that the M_S = 0 level of Ni bath spins is the lowest energy and separated from the M_S = $\pm$1 levels by a $\sim$67 cm^{-1} gap. The data for Fe likewise indicate that the Fe spins possess a ground M_S = 0 level. But, the M_S = 0 level is only separated by $\sim$3 cm^{-1} from the M_S = $\pm$1 levels and $\sim$24 cm^{-1} from the M_S = $\pm$2 levels for Fe relative to the 67 cm^{-1} gap for Ni. Note that the M_S = $\pm$1 levels are split for Fe by a transverse anisotropy $|E|$ = 1.43 cm^{-1}, and this anisotropy also mixes these levels. For Mn, the separation in all M_S levels is even smaller, with the ground-state $M_S = \pm 5/2$ levels only 0.38 cm^{-1} below the $M_S = \pm 3/2$ levels and 0.58 cm^{-1} below the $M_S = \pm 1/2$ levels (Fig. 3.2.3). As is shown below, these specific arrangements of M_S levels are likely critical to the roles of Mn, Ni, and Fe as diluents for Co.

3.2.4 AC Susceptibility

Out-of-phase, alternating-current (ac) magnetic susceptibility (χ''_M) measurements of pure **Co**, **Ni**, **Fe** and **Mn** reveal slow magnetic relaxation at zero applied dc field for only **Co** at ac frequencies

from 0.1 to 1500 Hz. For **Co**, we observe a nonzero, frequency-dependent c_M'' with a peak at 27.7 Hz at 2.0 K (Fig. S8 [136]). From 2 to 2.6 K, the frequency of this peak is temperature-independent, indicative of quantum tunneling. In contrast, above 3.0 K the peak position is highly temperature dependent. This behavior is typical of magnetic relaxation that transitions to thermally activated processes [122, 149]. In contrast **Ni**, **Fe**, and **Mn** display a featureless c_M'' at zero applied dc field (Fig. S9 [136]). The only indication of slow magnetic relaxation in these latter compounds is in **Mn**, which shows a high- frequency rise in $c_M{}''$ (200-1000 Hz) under 500-1500 G applied fields, but a peak maximum is never fully resolved (Fig. S10 [136]). These data establish the zero-field ac susceptibility measurement as an effective probe of the dynamics of **Co** alone in the three probed spin baths (composed of **Ni**, **Fe**, and **Mn**), owing to the absence of a zero-field χ_M'' signal in these diluents.

Zero-field ac magnetic susceptibility studies of **Co** diluted to different extents in **Ni** (Fig. S11-13 [136]) (Figs. 3.3) reveal a slowing of magnetic relaxation at 2 K upon dilution in the $S = 1$ bath. For pure **Co**, there is a region of temperature independence in c_M'' below 2.5 K when no external field is applied, an indication of magnetic dipole-mediated tunneling relaxation processes. In contrast, for the dilutions, magnetic relaxation is increasingly temperature dependent below 2.5 K with increasing dilution level, indicating that the tunneling process is disfavored in the diluted samples. Furthermore, the c_M'' peaks for **Co** broaden at low temperature when diluted, an additional indicator that the dilution process is effectively modulating the tunneling-based magnetic relaxation in the < 3 K temperature regime.

Quantitation of the relaxation times (τ) from a Cole-Cole analysis [150] of the AC data enabled the construction of Arrhenius plots (Fig. 3.3) for the relaxation dynamics of **Co** in **Ni**. For pure **Co**, τ is temperature-independent from 2.0 to 2.6 K at a value of 27.6 Hz (Fig. S8 [136]). The values of τ become longer over this temperature window and generally more temperature-dependent with increasing dilution level in **Ni**. The parameter a, which is also obtained from the Cole-Cole fitting (and characterizes the broadness of the c_M'' peak), increases from 0.276 at 2.0 K for pure **Co** to 0.579 at 2.0 K for the 1:34 **Co:Ni** dilution. A larger value of a in the Cole-Cole analysis suggests

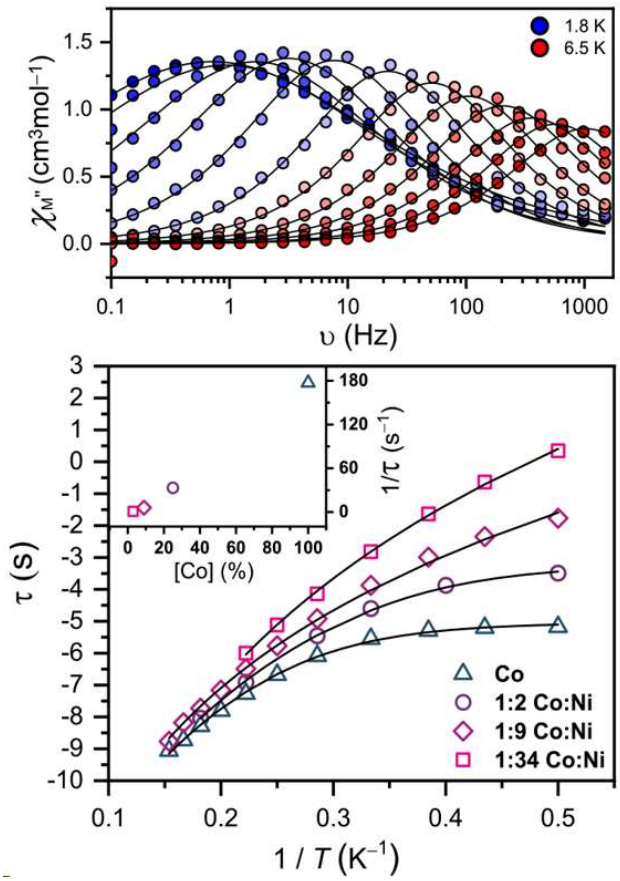

Figure 3.3: Top: Out-of-phase AC susceptibility data (χ''_M) for a 1:10 dilution of Co in Ni as a function of temperature in zero applied magnetic field. Data were collected at temperature intervals of .3 K from 1.8 K to 2.7 K and intervals of .5 K from 3.0 K to 6.5 K. Lines were generated via fits to the Cole-Cole equation (see SI). Bottom: Temperature dependence of the zero-field relaxation time (τ) for Co dilutions in Ni. Solid black lines are fits of the temperature dependence following the Raman and tunneling model proposed in the main text. Inset: $1/\tau$ as a function of dilution level.

a larger distribution of relaxation times for the **Co** unit upon dilution in **Ni**, which is likely because of some inhomogeneity in the disruption of the tunneling process.

The variable-temperature τ data for pure **Co** can be easily modeled with two common magnetic relaxation processes, Raman and quantum tunneling [119, 151], via the following equation (Fig. S8 [136] for full details):

$$\frac{1}{\tau} = AT^n + \frac{1}{\tau_{QTM}}, \tag{3.12}$$

here, $1/\tau$ is the relaxation rate, A is the Raman coefficient related to physical properties of the crystal, n is the Raman exponent, T is temperature, and τ_{QTM} is the timescale of the quantum tunneling of the magnetization. As a function of dilution, the best fits change, most notably for the tunneling process, which slows considerably, with τ_{QTM} = 6.6(4) ms for pure **Co** lengthening to τ_{QTM} = 41(3) ms for 1:2 **Co**:**Ni** (Figs. 3.3 and Fig. S15 [136]). These data indicate a slowing of magnetic relaxation via reduction of tunneling with increasing **Ni** concentration, just like dilution with **Zn** [122]. At higher dilutions, tunneling is no longer required to simulate the data, which can be modeled solely with a Raman process. The parameters for the Raman process change upon dilution, with A ranging from 0.03(1) to 0.8(2) $K^{-n}s^{-1}$ and n = 5.6(1) to 7.96(9) for **Co**:**Ni** dilutions. The Raman process is predicted to be dependent on dipolar interaction [151]. These data may provide the first quantitative evidence of the spin-bath impact on Raman relaxation; however, caution should be exercised in analyzing this change too deeply as the present analysis only spans a 5 K window of relaxation dynamics.

Additional variable-concentration ac susceptibility analyses of the dilutions of **Co** in $S = 2$ **Fe**, $S = {}^5/_2$ **Mn**, and $S = 0$ **Zn** were performed to test the effect of the different paramagnetic baths (Figs. 3.5 and Fig. S11-19 [136]). Zero-field, 2 K analyses of dilutions with **Fe** demonstrate a similar effect as **Ni** and **Zn**, in that increasing concentration of the diluent slows the relaxation rate of **Co** and the c''_M peaks broaden considerably. Importantly, however, **Fe** appears slightly less effective as a diluent than **Ni**, as the relaxation rates for **Co** appear faster in the **Fe** diluent at all studied concentrations. Just like with **Fe** and **Ni**, the peak in c''_M for **Co** when diluted in **Mn** becomes broadened in frequency space, indicating a distribution in relaxation times. However, in contrast

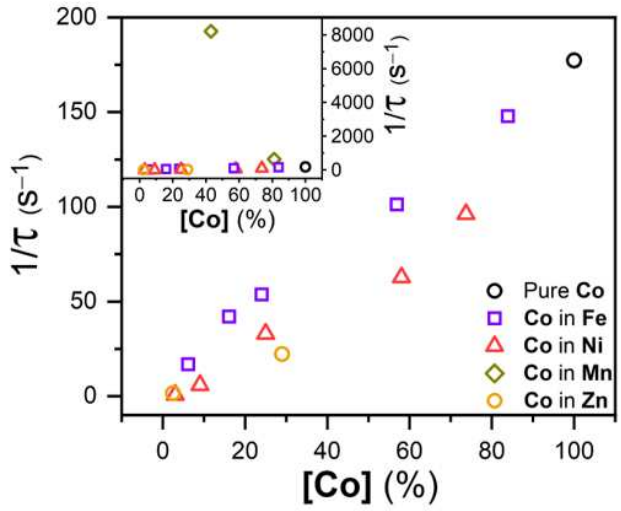

Figure 3.4: Variable-concentration relaxation rate ($1/\tau$) for Co diluted in Ni, Fe, Mn, and Zn. All relaxation rates were extracted from variable frequency AC susceptibility measurements at 2 K and zero applied magnetic field. *Inset*: Scale altered to show Mn dilution data.

to **Fe** and **Ni**, the c''_M peak maximum for **Co** in **Mn** rapidly moves to higher frequencies with increasing Mn concentration, indicating relaxation times that rapidly hasten beyond the detectable range of our magnetometer.

The presented relaxation time data suggest that the functional feature of the **Fe** and **Ni** spin baths is related to the magnetic anisotropy of the spin-bath ions. For an integer spin ion with a positive D (e.g. **Ni** and **Fe**), the ground M_S levels are $M_s = 0$ and bear no spin angular momentum. Note that this scenario is distinct from being completely diamagnetic, as both **Fe** and **Ni** still possess unpaired electrons (i.e., they are not undergoing a low-temperature spin crossover) [152], and there is no zero-field splitting for an $S = 0$ spin state. At 2 K, the 67 cm^{-1} energy gap between the $M_S = 0$ and ± 1 levels in **Ni** is significant, and the $M_S = 0$ level is populated by nearly 100 % of the spins in the **Ni** bath (following a simple Boltzmann distribution). Hence, to the magnetization dynamics of **Co** ions embedded in the **Ni** bath, this "effective $S = 0$" state for **Ni** appears to wield the same impact as the $S = 0$ **Zn** bath, despite **Ni** still bearing two unpaired electrons. **Fe** is also an integer spin with positive D, and hence it shows a similar effect on the quantum tunneling process for **Co**, owing to a high population of the $M_S = 0$ level (73 %). However, the data in Fig. (3.5) demonstrate that Fe does not disrupt the tunneling process as effectively as **Ni**, as the relaxation

rates for **Co** diluted in Fe are faster than when diluted in **Ni** at all measured concentrations. To explain this discrepancy, we note that the D of Fe is smaller than that of Ni by a factor of 11.7. This relatively smaller D (and the appreciable E) for **Fe** means that one of the $M_S = \pm 1$ levels is populated by 26 % at 2 K. Hence, **Fe** is less effective as a diluent because there is sufficient population of the magnetic $M_S \neq 0$ levels at 2 K, and the spin bath can hence induce quantum tunneling for **Co**. This explanation mirrors previous work by Cornia and coworkers on chain compounds, which showed that integer-spin ions with strong easy-plane anisotropy incorporated into chains of open-shell species will block intrachain exchange interactions [153].

The temperature dependence of τ for **Co** in **Fe** supports this argument. We posit that, if population of the excited-state M_S levels in **Fe** is driving relaxation of **Co** in that bath, then there should also be a greater T-dependence of τ for **Co** in **Fe** versus in **Zn**. Indeed, comparison of the temperature-dependence of τ for **Co** in baths of **Co**, **Fe**, **Ni** with that of **Zn** shows temperature dependence similar to that of the pure **Co**, while dilution with **Zn** appears less temperature dependent over the high-temperature regime (Fig. S19 [136]). 2.2 K. **Mn** is similar to **Co**, except there is only a pronounced temperature dependence below *ca.* 0.5 K.

With increasing dilution, both the local field magnitude and its temperature dependence gradually change from that of pure **Co** to that of the diluent, as shown in Fig. 3.5b for the case of **Co** in **Ni**. At a fixed temperature, we found that c_h^n depends linearly on the dilution for all baths (Fig 3.5c; S23), a consequence of our independent bath spin assumption. The nice agreement between the linear dependence of c_h^n and the experimental $1/\tau$ data on dilution confirms the applicability of this assumption.

The observed orientation, temperature, and diluent dependence of the local dipolar fields are all in agreement with our interpretation of the effect of the different $[M(SPh)_4]^{2-}$ environments. Thus, we see the operative mechanism of the **Ni** and **Fe** diluents. The $M_S = 0$ level is almost entirely populated at low temperature, causing all dipolar fields to fall to 0. This reduction of the dipolar field then suppresses the tunneling relaxation, as observed for diamagnetic **Zn** dilution. Furthermore, we see why **Co** and **Mn** both enable tunneling of embedded **Co** species: the half-

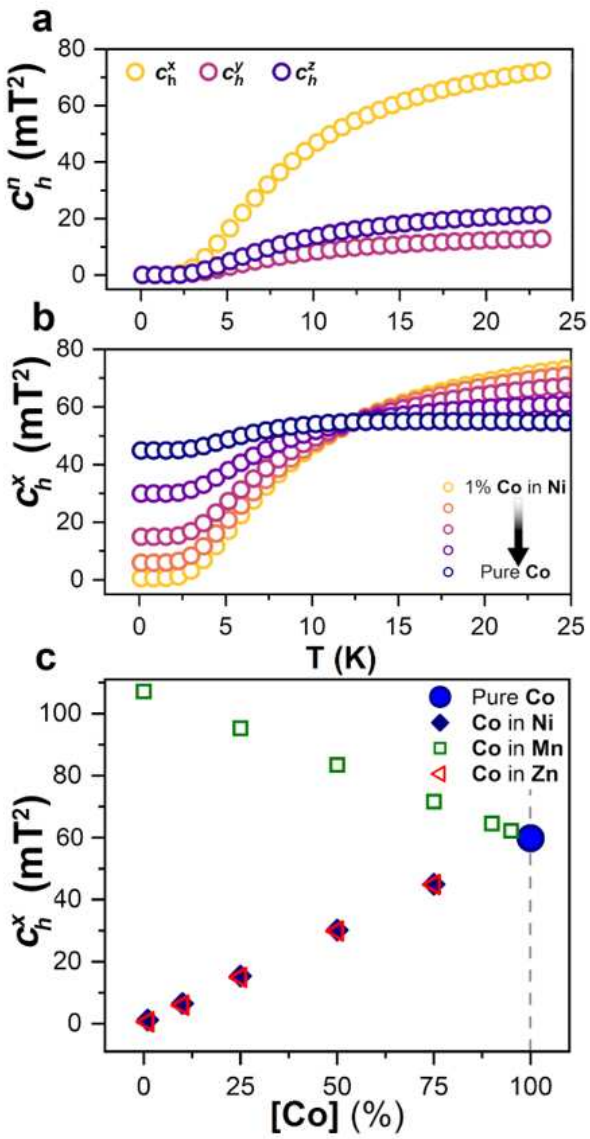

Figure 3.5: a. Computed variable-temperature local dipolar field variance for the x, y, and z components ($c_h^{x,y,z}$) of pure Ni. b. Computed variable temperature c_h^x for a $[Co(SPh)_4]^{2-}$ embedded in Ni. c. Computed variable-concentration c_h^x for $[Co(SPh)_4]^{2-}$ diluted in Mn, Ni, and Zn at 2.6 K.

integer spins of these bath complexes (in contrast to the integer-spin, positive-D Ni) ensure that a substantial, nonzero dipolar field (**Mn** larger than **Co**) exists at low temperature. Consequently, we see tunneling proceed in pure **Co** and the relaxation rate increase in **Mn**. Together, these computational and experimental data pinpoint the mechanistic function of the chemically tuneable paramagnetic spin bath.

3.2.5 Conclusion

The foregoing demonstration is the first slowing of the magnetization dynamics of a single-molecule magnet by deliberate chemical dilution in a magnetically concentrated environment. Furthermore, the results reveal that $S = 1$ and $S = 2$ complexes can be used to reduce quantum tunneling of the magnetization, like $S = 0$ analogues, if D is positive and of sufficient magnitude.

There are two broader implications of these results. First, from a practical standpoint, the ability to realize magnetic dilution with open-shell complexes opens the door to the effective dilutions when closed-shell analogues are chemically unstable or impossible to synthesize, as for example, radical-bridged bimetallic species [154]. Second, we show that the paramagnetic dilution technique is a valid means of manipulating relaxation via chemical engineering of the dipolar field. The work thus provides a new experimental technique for studying the relaxation dynamics of molecular magnets, one that, critically, approaches the proposed conditions where magnetic molecules may be applied. We finally highlight that this work describes the impact on a single-molecule magnet with easy-axis magnetic anisotropy, for which quantum tunneling is the dominant relaxation mechanism. There are many other relaxation mechanisms, many of which are predicted to be affected by dipolar fields [155–157]. Future work will test these theories using the paramagnetic dilution approach presented here, and those results will be presented in due course.

3.3 Calculation and estimations of the relaxation rate

The following details are partitioned into four subsections. In the first two subsections, we briefly define the out-of-phase magnetic susceptibility and its relationship to a relaxation rate; then

we discuss the relaxation rate in the context of an $S = \frac{1}{2}$ ion induced by a dipolar magnetic field. In the last two sections, we justify treatment of the embedded Co(II) ions of $[Co(SPh)_4]^{2-}$ as effective $S = \frac{1}{2}$ species, then describe how we calculated the expectation values of the dipolar field components $c_h^n = \langle h_n h_n \rangle$, $(n = x, y, z)$. A visual representation of the vectors on the easy axis and the transformed axis is given (see Fig. 3.1).

3.3.1 Out-of-phase magnetic susceptibility description used for model

First, we describe the relationship between out-of-phase susceptibility and spin relaxation rate, which yielded the c''_M versus frequency plots (Figs. 3.3). The AC magnetic field (H) used to measure the relaxation behavior has a simple sinusoidal, linearly polarized form, where ω is the frequency of the applied field:

$$\mathbf{H}(t) = \mathbf{H}\sin(\omega t) \tag{3.13}$$

the power absorbed by the spin system at a given frequency, $P(\omega)$, is

$$P(\omega) = -\frac{1}{T}\int_0^T M^i(t)dH^i(t) = \frac{\omega}{2}H^i H^j \chi''_{ij}(\omega) \tag{3.14}$$

where M^i is the i-th component of the magnetization, T is the period, and χ'' is the imaginary part of the magnetic susceptibility tensor

$$\chi(\omega) \equiv \chi'(\omega) + i\chi''(\omega) \tag{3.15}$$

Below we take the independent spin approximation and consider the χ due to a single spin for simplicity. It is useful to relate χ to the time-correlated function or relaxation function defined as

$$\Phi^{ij}(t) \equiv \frac{1}{2}\langle S^i(t)S^j + S^j(t)S^i\rangle - \langle S^i\rangle\langle S^j\rangle \tag{3.16}$$

where S^i is the i-th component of the spin operator. The symmetrization is to ensure that $\Phi^{ij}(t)$ is real. Below we assume $\langle S\rangle = 0$ in the absence of external magnetic fields. The fluctuation-

dissipation theorem dictates

$$\gamma^2 \Phi^{ij}(\omega) = \frac{2\hbar}{1 - e^{-\beta\hbar\omega}} (\chi'')^{ij}(\omega) \tag{3.17}$$

where $\gamma = g\mu_B/\hbar$ is the gyromagnetic ratio and g is the Landé g-factor for the electronic spin. Since our interest is in χ''_{ij}, it is sufficient to consider only the time correlation function, Φ. In the case that $\Phi(t)$ is described by a simple exponential decay, $\Phi(t) = \Phi_0 e^{-\Gamma|t|}$, where is the decay rate ($\Gamma > 0$), we have

$$\Phi(\omega) = \frac{2\Gamma}{\omega^2 + \Gamma^2} \Phi_0 \tag{3.18}$$

In the present experiments the frequency $\omega (< 1000$ Hz) is much smaller than $k_B T/\hbar \sim 10^{11}$ Hz. So $e^{-\beta\hbar\omega} \approx 1 - \beta\hbar\omega$, and we can obtain χ''

$$\chi''(\omega) \approx \frac{\gamma^2}{k_B T} \frac{\omega\Gamma}{\omega^2 + \Gamma^2} \Phi_0 \tag{3.19}$$

which is non-monotonic with ω and takes its maximum at $\omega = \Gamma$. Thus, the position of the low-frequency peak of $\chi''(\omega)$ corresponds to the decay rate. If more complex fitting functions (e.g., the Cole-Cole function) of the experimental $\chi''(\omega)$ are needed, the decay behavior is likely to be more complicated than the simple exponential form.

3.3.2 Relaxation of an $S = \frac{1}{2}$ spin

In this section we give a general discussion on the relaxation of an $S = \frac{1}{2}$ spin in the presence of a DC magnetic field and explain the difficulty in modeling it when the DC field vanishes. The consideration of $S = \frac{1}{2}$ is also motivated by the fact that the low-frequency behavior of the $\chi''(\omega)$ for Co spins is governed by the low-energy Kramers doublet behaving as a spin-$\frac{1}{2}$.

We assume the DC magnetic field is along z, and the spin is subject to a fluctuating magnetic field $(\mathbf{h})$ which is assumed to be much weaker than the DC field ($\mathbf{h}_0$). The Hamiltonian is

$$H = -h_0 \sigma_z - \mathbf{h}(t) \cdot \boldsymbol{\sigma} \tag{3.20}$$

where $\boldsymbol{\sigma}$ is the Pauli matrix vector and all numerical factors are absorbed into h_0 and $\mathbf{h}(t)$. We also assume that $\mathbf{h}(t)$ has a zero time-average. For simplicity we consider the time correlation function Φ^{ii} only, i.e.

$$\Phi^{ii} = \langle \sigma^i(t)\sigma^i \rangle - \langle \sigma^i \rangle^2 \tag{3.21}$$

When $|\mathbf{h}| \ll h_0$, Φ^{ii} can be calculated from time-dependent perturbation theory. Denoting $H_0 = -h_0\sigma_z$ and $H(t) = -\mathbf{h}(t)\cdot\boldsymbol{\sigma}$, up to 2nd order of h one can find

$$\sigma^i(t) \approx \sigma_0^i(t) - \frac{1}{\hbar^2}\int_0^t dt_1 \int_0^{t_1} dt_2 U_0^\dagger(t)\left[\left[\sigma^i, \sigma_0^j(-t_2)\right], \sigma_0^k(-t_1)\right] U_0(t)\langle h^j(t_2)h^k(t_1)\rangle_h \tag{3.22}$$

where $\langle h^j(t_2)h^k(t_1)\rangle_h$ is the stochastic average over $\mathbf{h}(t)$, and $U_0 \equiv \exp(-itH_0/\hbar)$. We assume $\mathbf{h}(t)$ to be described by a Gauss-Markov process with the autocorrelation

$$\langle h^j(t_2)h^k(t1)\rangle_h = c_h\delta^{jk}e^{-\Gamma_h|t_1-t_2|} \tag{3.23}$$

Here, c_h is the varience of the dipolar fields at $\Delta = 0$, δ^{ij} is the Kronecker delta, and Γ_h is the phenomenological decay rate. The integrals in Eq. 3.22 can be done explicitly, leading to

$$\begin{aligned}
\sigma^+(t) = &\quad \sigma_0^+(t)\left[1 - \tfrac{c_h}{\hbar^2}\left(\tfrac{|t|}{\Gamma_h} + \tfrac{e^{-\Gamma_h|t|}-1}{\Gamma_h^2} - \tfrac{|t|}{2i\omega_0-\Gamma_h} + \tfrac{e^{2i\omega_0 t-\Gamma_h|t|}-1}{(2i\omega_0-\Gamma_h)^2}\right)\right] \\
\sigma^-(t) = &\quad \sigma_0^-(t)\left[1 - \tfrac{c_h}{\hbar^2}\left(\tfrac{|t|}{\Gamma_h} + \tfrac{e^{-\Gamma_h|t|}-1}{\Gamma_h^2} + \tfrac{|t|}{2i\omega_0+\Gamma_h} + \tfrac{e^{-2i\omega_0 t-\Gamma_h|t|}-1}{(2i\omega_0+\Gamma_h)^2}\right)\right] \\
\sigma^z(t) = &\quad \sigma_0^z(t)\left[1 - \tfrac{c_h}{\hbar^2}\left(\tfrac{2|t|\Gamma_h}{4\omega^2+\Gamma_h^2} + \tfrac{e^{2i\omega_0 t-\Gamma_h|t|}-1}{(2i\omega_0-\Gamma_h)^2} + \tfrac{e^{-2i\omega_0 t-\Gamma_h|t|}-1}{(2i\omega_0+\Gamma_h)^2}\right)\right]
\end{aligned} \tag{3.24}$$

where $\omega_0 \equiv h_0/\hbar$. Therefore, all components have a common form,

$$\sigma^i(t) = \sigma_0^i(t)[1 - f(t)] \approx \sigma_0^i(t)e^{-f(t)} \tag{3.25}$$

A more complete discussion on the approximation involved in the last step can be found is Ref. [158] The decay behavior of $\sigma^i(t)$ is thus due to the linear in t terms in Eq. 3.24. These can also

be obtained by taking the long time limit ($|t| \to \infty$)

$$\begin{aligned} \sigma^+(t) = &\quad \sigma_0^+(t)\left[1 - \tfrac{c_h}{\hbar^2}\left(\tfrac{|t|}{\Gamma_h} - \tfrac{|t|}{2i\omega_0 - \Gamma_h}\right)\right] \\ \sigma^-(t) = &\quad \sigma_0^-(t)\left[1 - \tfrac{c_h}{\hbar^2}\left(\tfrac{|t|}{\Gamma_h} + \tfrac{|t|}{2i\omega_0 + \Gamma_h}\right)\right] \\ \sigma^z(t) = &\quad \sigma_0^z(t)\left[1 - \tfrac{c_h}{\hbar^2}\tfrac{2|t|\Gamma_h}{4\omega^2 + \Gamma_h^2}\right] \end{aligned} \tag{3.26}$$

In the $\omega_0 \to 0$ limit relevant to AC susceptibility measurements, one cannot truncate the perturbation series at 2nd order (to be discussed further below). However, in the following regime

$$\sqrt{c_h}/\hbar \ll \omega_0 \ll \Gamma_h \tag{3.27}$$

the 2nd order perturbation result should still be valid, which gives

$$\Gamma^{\pm} = \Gamma^z = \frac{2c_h}{\hbar^2 \Gamma_h} \tag{3.28}$$

Where Γ^z is the axial component of the relaxation rate. Although Eq. 3.27 may not be satisfied in the present experiments, the relaxation rate in Eq. 3.28 is still a useful reference for making qualitative estimates. For example, when $[Co(SPh)_4]^{2-}$ is diluted with Ni or Zn which does not contribute to the fluctuating dipolar fields at low temperatures, the dipolar field felt by each $[Co(SPh)_4]^{2-}$ is only due to the other Co ions, felt at long range. Then it is natural to expect that $\Gamma_h \sim \Gamma$ and Eq. 3.28 suggests that

$$\Gamma \sim \Gamma_h \sim \frac{\sqrt{2c_h}}{\hbar} \tag{3.29}$$

We will see below that the other limit $\Gamma_h \ll \frac{\sqrt{c_h}}{\hbar}$, Γ is on the order as Γ_h and is independent of c_h. Therefore eq. 3.28 is expected to hold approximately when Γ_h is not too small compared to $\sqrt{c_h}/\hbar$.

A nonperturbative treatment of zero-field spin relaxation was first developed by Kubo and Toyabe [159] by treating $\mathbf{h}(t)$ as a random vector that can be described as a Gauss-Markov process. Analytic results can be obtained using this approach in the static limit ($\Gamma_h = 0$) and isotropic

$c_h^n = c_h$. The result is the Kubo-Toyabe relaxation function

$$\Phi^{zz}(t) = \frac{1}{3} + \frac{2}{3}\left(1 - \frac{c_h t^2}{\hbar^2}\right) e^{-\frac{c_h t^2}{2\hbar^2}} \tag{3.30}$$

which approaches a constant as $t \to \infty$. When Γ_h is finite the $\frac{1}{3}$ will be replaced by a complex time-dependent function and only numerical results can be obtained in general. Therefore, the long-time decay behavior necessarily comes from a finite Γ_h. In the present case, since Γ_h itself is implicitly dependent on c_h, as the bath spins are coupled together through the dipolar interaction, such a calculation is not necessarily useful. Instead, we may consider the other limit $\Gamma_h \ll \frac{\sqrt{c_h}}{\hbar}$ that was not able to be addressed using the perturbation method. For isotropic c_h [151] showed analytically that in this limit the long-time behaviours of Φ^{zz} is described by an infinite sum of exponentially decaying functions with different decay rates approach

$$\Gamma_n = \left(\frac{-1 + \sqrt{17}}{2} + 2n\right)\Gamma_h, \quad n = 0, 1, 2, \ldots \tag{3.31}$$

The long-time decay is then governed by $\Gamma_0 \approx 1.56\Gamma_h$. Therefore, qualitatively we expect that the decay rate is of the same order of magnitude as Γ_h in the limit $\Gamma_h \ll \frac{\sqrt{c_h}}{\hbar}$ as well, and $\frac{\sqrt{c_h}}{\hbar}$ serves as an upper bound of Γ. The main problem with this approach is, however, that Γ_h depends on the microscopic details of the bath, some of which are experimentally unknown here and therefore its value cannot be given by this theory.

3.3.3 Relaxation of an effective $S = \frac{1}{2}$ pseudospin of a single Co ion

The cobalt complex of $[\mathrm{Co(Sph)_4}]^{2-}$ is an $S = \frac{3}{2}$ molecule with large zero-field splitting. The local Hamiltonian of an isolated Co ion is governed by the crystal electric field (CEF) contribution. By local terms up to 2nd order in spin operators we have the following simplified CEF Hamiltonian

$$H_{CEF} = DS_z^2 + E(S_x^2 - S_y^2), \tag{3.32}$$

here D and E are input from fits of experimental data. For $S = \frac{3}{2}$, the spin operators take the following form in the S_z eigenstate basis $\{|m = -3/2\rangle, |m = -1/2\rangle, |m = 1/2\rangle, |m = 3/2\rangle\}$

$$S_x = \begin{pmatrix} 0 & \frac{\sqrt{3}}{2} & 0 & 0 \\ \frac{\sqrt{3}}{2} & 0 & 1 & 0 \\ 0 & 1 & 0 & \frac{\sqrt{3}}{2} \\ 0 & 0 & \frac{\sqrt{3}}{2} & 0 \end{pmatrix}, S_y = \begin{pmatrix} 0 & \frac{\sqrt{3}}{2}i & 0 & 0 \\ -\frac{\sqrt{3}}{2}i & 0 & i & 0 \\ 0 & i & 0 & \frac{\sqrt{3}}{2}i \\ 0 & 0 & -\frac{\sqrt{3}}{2}i & 0 \end{pmatrix}, S_z = \begin{pmatrix} -\frac{3}{2} & 0 & 0 & 0 \\ 0 & -\frac{1}{2} & 0 & 0 \\ 0 & 0 & \frac{1}{2} & 0 \\ 0 & 0 & 0 & \frac{\sqrt{3}}{2} \end{pmatrix} \tag{3.33}$$

where we have set $\hbar = 1$. For the case of $(Ph_4P)_2[Co(SPh)_4]$, $D < 0$ and $|D| \gg |E|$, the two low energy eigenstates mainly consist of the states with $m = \pm 3/2$. At the lowest temperatures (below 10 K, where the χ'' measurements were performed) the size of D ensures near complete population of these levels and negligible population of the higher lying $m = \pm 1/2$ levels. Thus, we define them as up and down eigenstates of pseudospin $S = 1/2$, as follows (assuming $E > 0$)

$$\begin{aligned} |\uparrow\rangle &= u|m = 3/2\rangle - \sqrt{1-u^2}|m = -1/2\rangle \\ |\downarrow\rangle &= v|m = -3/2\rangle - \sqrt{1-v^2}|m = 1/2\rangle \end{aligned} \tag{3.34}$$

where

$$u = \left[1 + \left(\frac{\sqrt{D^2 + 3E^2} + D}{\sqrt{3}E}\right)^2\right]^{-\frac{1}{2}}, v = \frac{\sqrt{D^2 + 3E^2} - D}{\sqrt{3E^2 + (\sqrt{D^2 + 3E^2} - D)^2}} \tag{3.35}$$

recalling that $D < 0$, u, v approach 1 as $|E/D| \to 0$. One can then define the pseudospin operators $\tilde{\boldsymbol{\sigma}}$ as the usual Pauli matrices but in the $|\uparrow\rangle, |\downarrow\rangle$ basis. Moreover, the original $S = 3/2$ operators projected to the pseudo spin space and rotated to the $|\uparrow\rangle, |\downarrow\rangle$ basis have the following form

$$(S_x, S_y, S_z)_{ps} = (g_x\tilde{\sigma^x}, g_y\tilde{\sigma^y}, g_z\tilde{\sigma^z}), \tag{3.36}$$

$$(g_x, g_y, g_z) = \left(\frac{D-3E}{2\sqrt{D^2+3E^2}} + \frac{1}{2}, -\frac{D+3E}{2\sqrt{D^2+3E^2}} - \frac{1}{2}, -\frac{D}{2\sqrt{D^2+3E^2}} + \frac{1}{2} \right) \approx \frac{3}{2}\left(\frac{E}{D}, \frac{E}{D}, 1 \right) \tag{3.37}$$

Since $|E/D| \ll 1$, magnetic fields predomintly couple to the z component of the pseudospin only. Thus, if one calculates χ'' and Φ using the $S = 1/2$ results in the previous sections, the power absorption is dominated by χ''_{zz} since the other contributions will be suppressed by E^2/D^2. On the other hand, in the expression of $\sigma_z(t)$ (or rather $\tilde{\sigma}^z(t)$) one would just need the following replacement

$$c_h \to \frac{9E^2\gamma_{\text{Co}}^2\hbar^2}{8D^2}(c_h^x + c_h^y) \tag{3.38}$$

if different components of the fluctuating magnetic fields are allowed to have different variances. We have also recovered the gyromagnetic ratio of Co ($\gamma_{\text{Co}} = g_{\text{Co}}\mu_B/\hbar$) and $\hbar$. A crude estimate of the relaxation rate based on Eq. (3.28) is then

$$\Gamma^z = \frac{9E^2\gamma_{\text{Co}}^2}{4D^2\Gamma_h}(c_h^x + c_h^y) \tag{3.39}$$

or if $\Gamma^z \sim \Gamma_h$,

$$\Gamma^z \sim \frac{3|E\gamma_{\text{Co}}|}{2|D|}\sqrt{c_h^x + c_h^y} \tag{3.40}$$

From this result, we see that the relaxation rate is directly driven by the magnetic dipolar field components in the x-y plane relative to the embedded spin. In addition, we see that the rate is dependent on the E of the embedded ion. As E is extremely small and likely consistent of different environments owning to the strong structural similarities of the MS_4 coordination shells [105], the rate changes as a function of bath are more likely to be impacted by changes in c_h^x and c_h^y, which are diluent dependent.

3.3.4 Estimation of c_h

In this subsection we provide estimates of the c_h in the present experimental system. The dipolar magnetic field generated at the position of a Co ion in $[Co(SPh)_4]^{2-}$ (assumed to be the

origin) by another spin (S_i'') is

$$h_i = \frac{\mu_0 \gamma_b}{4\pi r_i^3}[3\hat{\mathbf{r}}(S_i'' \cdot \hat{\mathbf{r}}_i) - S_i''] \tag{3.41}$$

where γ_b is the gyromagnetic ratio of bath spins, $\hat{\mathbf{r}}$ is the distance separating the two spins, and μ_0 is the vacuum permeability. The total dipolar field at the origin is

$$\mathbf{h}_d = \sum_i \mathbf{h}_i \tag{3.42}$$

For the convenience of studying the temperature dependence of bath spins, we introduce $\{\hat{e}'' = \{\hat{x}''\hat{y}''\hat{z}''\}$ consistent with the local coordinates of a spin back S_i (according to which E and D are defined). Similarly, the local basis for the Co ion at the origin is defined as $\{\hat{e}'\} = \{\hat{x}', \hat{y}', \hat{z}'\}$. As a first approximation, we assume the spin baths are not correlated with each other. Then, taking $\langle h^{z'} h^{z'} \rangle$ as an example

$$\langle h^{z'} h^{z'} \rangle = \sum_{ij} \langle h_i^{z'} h_j^{z'} \rangle = \sum_i \langle h_i^{z'} h_i^{z'} \rangle \tag{3.43}$$

$$= \sum_i \left(\frac{\mu_0 \gamma_b}{4\pi r_i^3} \right) \left[9(\hat{\mathbf{r}} \cdot \hat{\mathbf{z}}')^2 \langle (\mathbf{S}_i'' \cdot \hat{\mathbf{r}}_i)^2 \rangle - 3(\hat{\mathbf{r}}_i \cdot \mathbf{z}') \left(\langle (\mathbf{S}'' \cdot \hat{\mathbf{r}}_i)(S_i'')^{z'} \rangle + (S_i'')^{z'} \rangle (\mathbf{S}'' \cdot \hat{\mathbf{r}}_i) \right) + \langle (S_i'')^{z'} (S_i'')^{z'} \rangle \right] \tag{3.44}$$

$\langle S^\alpha S^\beta \rangle$ for independent spins in thermal equilibrium should be

$$\langle S^\alpha S^\beta \rangle = \frac{1}{Z} \text{Tr} \left[e^{-\beta \epsilon_i} S^\alpha S^\beta \right] = \frac{1}{Z} \sum_i e^{-\beta \epsilon_i} (U^\dagger S^\alpha S^\beta U)_{ii} \tag{3.45}$$

Where U is the unitary transformation that diagonalizes H. Due to the independent spin assumption, samples of different dopant concentrations can be considered simply by making

$$\langle h_i^\alpha h_i^\alpha \rangle = f_{\text{Ni}} \langle h_i^\alpha h_i^\alpha \rangle_{\text{Ni}} + f_{\text{Co}} \langle h_i^\alpha h_i^\alpha \rangle_{\text{Co}} \tag{3.46}$$

where f_s is the concentration of species s, and $\langle h_i^\alpha h_i^\alpha \rangle_s$ is the correlation calculated with all bath spins being species s. It is important to note that in calculating $\langle h_i^\alpha h_i^\alpha \rangle$ one must use the correct

spin Hamiltonians, i.e. $S = 3/2$ for Co, and $S = 1$ for Ni. Furthermore for Ni, since its ground state is a singlet (i.e. $D > 0$), the dipolar field due to Ni is not active unless the temperature is comparable to $|D|$. Fundamentally this is because the effect of the "dipolar field" in Co spin relaxation comes from intra-band transitions among the low-energy modes in the bath. Therefore we account for this effect in our calculation by replacing S with PSP, where P is a projection operator that projects out matrix elements across nondegenerate levels.

In calculating $c_h^\alpha \sim \langle h^\alpha h^\alpha \rangle$ we use $\gamma_s = g_s \mu_B/\hbar$ where $s = \{Ni, Co\}$, together with parameter values listed tables 3.1 and 3.2. c_h therefore has units of $T^2(T =$Tesla), and the spin operators are dimensionless.

Parameter	Unit	Value
$\hbar$	[eV][Sec]	6.582 $\times 10^{-16}$
$\hbar$	[Joules][Sec]	1.05 $\times 10^{-34}$
μ_B	$\frac{\text{[Joules]}}{\text{[Tesla]}}$	9.27 $\times 10^{-24}$
μ_0	$\frac{\text{[Henries]}}{\text{[Meter]}}$	$4\pi \times 10^{-7}$
c	$\frac{\text{[cm]}}{\text{[sec]}}$	2.998 $\times 10^{+10}$
g_{Ni}	-	5.105
g_{Co}	-	2.24
g_{Mn}	-	2.126
$\gamma = \frac{g\mu_B}{\hbar}$	$\frac{\text{[eV]}}{\text{[Tesla]}} \frac{1}{[eV][sec]}$	$g \times 5.788 \times 10^{-5} \times \frac{1}{6.582 \times 10^{-16}}$
D_{Ni}	[eV]	+67.54 cm$^{-1}\times\hbar$[eV sec] $\times$c[cm/sec]
E_{Ni}	[eV]	-0.25 cm$^{-1}\times\hbar$[eV sec] $\times$c[cm/sec]
D_{Co}	[eV]	-61.4 cm$^{-1}\times\hbar$[eV sec] $\times$c[cm/sec]
E_{Co}	[eV]	+0.0011 cm$^{-1}\times\hbar$[eV sec] $\times$c[cm/sec]
D_{Mn}	[eV]	-0.097 cm$^{-1}\times\hbar$[eV sec] $\times$c[cm/sec]
E_{Mn}	[eV]	+0.008 cm$^{-1}\times\hbar$[eV sec] $\times$c[cm/sec]

Table 3.1: Parameter values used in the calculations of c_h for Ni, Co, and Mn bath spins.

	Ni (no projection)	Ni (projection)	Co	Mn
$(c_h)_x$	5.1 $\times 10^{-5}$	2.7 $\times 10^{-7}$	6.7 $\times 10^{-5}$	9.66 $\times 10^{-5}$
$(c_h)_y$	1.1 $\times 10^{-4}$	4.8 $\times 10^{-8}$	2.8 $\times 10^{-5}$	7.14 $\times 10^{-5}$
$(c_h)_z$	1.6 $\times 10^{-4}$	8.0 $\times 10^{-8}$	4.1 $\times 10^{-5}$	1.02 $\times 10^{-5}$

Table 3.2: Calculated values of c_h for Ni, Co, and Mn as spin baths in units of T^2 at 2 K.

In much smaller c_h in the case of Ni when one uses the projection operator is due to the inactive $m = \pm 1/2$ levels of its spin at low temperatures. Thus, the typical size of the fluctuating dipolar magnetic field, when the bath spins have dipole moments $\sim 10^{-3}T$. This can be converted to a frequency by doing the substitution in Eq. 3.38. Since $\frac{g_{co}\mu_B E}{D} \times 1T \sim 10^{-9}eV$, the fluctuating dipolar field corresponds to an energy scale of $\sim 10^{-11}$ to 10^{12} eV, or 10^3 to 10^4 Hz. This is larger than $\Gamma = \frac{1}{\tau} < 10^2$ Hz measured experimentally. The experimental system is therefore in the limit of $\Gamma_h \ll \frac{\sqrt{c_h}}{\hbar}$ when $[Co(SPh)_4]^{2-}$ is diluted by nonmagnetic ions such as Zn(11). Thus, the slowing down of Co relaxation as the concentration of Ni increases is due to the decreasing Γ_h. Although qualitatively it is reasonable to expect that Γ_h should decrease with decreasing c_h, their precise relationship can only be established by understanding the dynamics of the correlated bath spins, which is beyond the theories presented here and will be left for future processes that are well documented for single molecule magnet like $[Co(SPh)_4]$ [105]. On the other hand, when the bath spins are Mn, the relaxation rate seems to approach the $\frac{\sqrt{c_h}}{\hbar}$. Thus Eq. 3.28 may be used to estimate the dependence of Γ on the concentration of Mn.

Chapter 4

Spin Hall effect with interaction

Spintronics utilizes both charge and spin degrees of freedom of electrons to manipulate nonequilibrium and equilibrium states of materials [160–163]. At its center is the control of spin currents [164–166]. A key mechanism is the spin Hall effect (SHE), which describes the transverse spin current response to a charge current. Its reciprocal is the inverse spin Hall effect (ISHE) where a transverse charge current arises in response to a spin current. Both effects rely fundamentally on spin-orbit coupling (SOC).

The SHE was predicted as far back as 50 years ago [167], but it wasn't until 1999 [168] and 2000 [169] that it resurfaced with theoretical predictions suggesting the possibility of significant contributions to the intrinsic SHE. The mechanisms underlying the SHE are described in terms of AHE, which encompasses three contributions: Intrinsic deflection, skew scattering, and side jump.

A schematic for what the SHE is illustrated in Fig 4.1. The sample is placed between two leads, then an electric field is applied along the x axis to drive a current. Spin will then accumulate along the y axis.

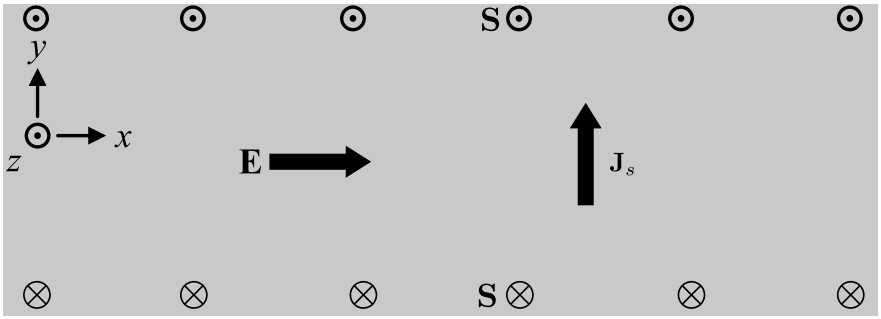

Figure 4.1: Schematic of the spin Hall effect. An electric applied along the x axis generates a spin current in the y axis.

The interpretation of the SHE as a response to a spin current is valid only in the regime where the SOC is much smaller than $\hbar/\tau$. With τ denoting the disorder scattering time. In this weak SOC

limit, one can meaningfully define spin currents and formulate continuity equations. However, in materials of interest for spintronics applications—where SOC is typically strong—spin currents become ill-defined, and the notion of a continuity equation breaks down, even with the inclusion of a phenomenological decay term. In such cases, the concept of spin accumulation provides a more robust and physically meaningful description. Below, we solve for the non-equilibrium Green's functions to compute physical observables, focusing in particular on the transverse edge spin accumulation.

We here analyze a tight-binding Hamiltonian that simultaneously incorporates on-site electron-electron interactions and intrinsic spin-orbit coupling in the form of a Kane-Mele term. While each component has been studied extensively in isolation, their combined treatment remains largely unexplored due to the added complexity introduced by competing energy scales and broken spin conservation. Our approach captures both correlation-driven effects and topological band structure on equal footing.

4.1 SHE with spin-orbit coupling and interaction

We now discuss a mechanism for the SHE that arises from including interactions. In our study, we numerically compute the SHE in a finite strip of a hexagonal lattice connected to leads held at different chemical potentials. The Hamiltonian incorporates both Kane-Mele spin–orbit (SO) coupling [170], whose strength is governed by λ below and an exchange field described by the $\mathbf{m}_i \cdot \sigma_{\alpha\beta}$ term, where the exchange field breaks time-reversal symmetry in the spin sector and the SO interaction entangles the spin and orbital degrees of freedom. We specifically examine how these mechanisms affect the bare magnetic susceptibility at the edge of a two-dimensional topological insulating ribbon. To further elucidate our findings, we develop an analytical toy model and compare its predictions with the numerical results.

To model this we consider the following Hamiltonian, obtained from the usual Hartree-Fock decoupling [171] of the Kane-Mele-Hubbard model [172, 173],

$$H \approx t \sum_{\langle i,j\rangle,\alpha} c^{\dagger}_{i\alpha} c_{j\alpha} + i\lambda \sum_{\langle\langle i,j\rangle\rangle,\alpha\beta} \nu_{ij} c^{\dagger}_{i\alpha} \sigma^{z}_{\alpha\beta} c_{j\beta} + \frac{U}{2} \sum_{i,\alpha,\beta} c^{\dagger}_{i\alpha} \left(n_i \mathbb{1}_{\alpha\beta} - \mathbf{m}_i \cdot \boldsymbol{\sigma}_{\alpha\beta} \right) c_{i\beta} + \frac{U}{4} \sum_{i} \left(n_i^2 - |\mathbf{m}_i|^2 \right) \tag{4.1}$$

where t is the hopping potential, λ is the strength of the Kane-Mele spin orbit coupling. The factor ν_{ij} takes values ± 1, with $\nu_{ij} = -\nu_{ji}$, determined by the orientation of the two nearest-neighbor bonds as the electron moves from site i to j: $\nu_{ij} = +1$ if the second neighbor is reached in a counterclockwise sense, and $\nu_{ij} = -1$ if reached clockwise. $\langle \dots \rangle$ & $\langle\langle \dots \rangle\rangle$ is the nearest neighbors, and second nearest neighbors respectively, $\mathbb{1}$ is the 2×2 identity matrix, $\boldsymbol{\sigma} = (\sigma^x, \sigma^y, \sigma^z)$ is a vector of 2×2 Pauli matrices acting in spin space, and defining the local mean electron density as

$$n_i = \left\langle \sum_{\alpha} c^{\dagger}_{i\alpha} c_{i\alpha} \right\rangle, \tag{4.2}$$

and the local mean spin polarization as

$$\mathbf{m}_i = \left\langle \sum_{\alpha\beta} c^{\dagger}_{i\alpha} \boldsymbol{\sigma}_{\alpha\beta} c_{i\beta} \right\rangle, \tag{4.3}$$

which is determined self consistently.

4.1.1 Calculating spin accumulation

We briefly describe the procedure [174] for calculating the spin accumulation. We begin with a tight-binding Hamiltonian for a lattice connected to two leads. For a system with N sites, quantities such as the Green's function G and the self-energy Σ are represented by $N \times N \times K$ matrices at each energy, i.e. $G = G(r_i, r_j, E_k)$.

In principle, the retarded and advanced Green's function, G^R and G^A, are obtained from

$$G^{\mathrm{R}} = \left[EI - H_{\mathrm{C}} - \Sigma^{\mathrm{R}}\right]^{-1} \tag{4.4}$$

$$G^{\mathrm{A}} = \left[G^{\mathrm{R}}\right]^{+}. \tag{4.5}$$

where H_c is the Hamiltonian of the conductor, Σ^R includes contributions from electron-electron interactions and coupling to the leads. Once G^R is determined, any observable can be computed.

To describe the transport properties, we need to consider the correlation between lattice sites r_i in the conductor, and sites p_j in the leads by partitioning the full Green's function as,

$$G = \begin{bmatrix} G_p & G_{pC} \\ G_{Cp} & G_C \end{bmatrix}, \tag{4.6}$$

where G_C is the Green's function for the conductor, G_{Cp} (and its conjugate G_{pC}) describes the coupling between the conductor and the leads, and G_P pertains to the leads themselves.

We begin by calculating the self-energy term as,

$$\Sigma(p_i, p_j, E) = t^2 g(p_i, p_j, E) \tag{4.7}$$

$$= -t \sum_{m \in p} \chi_m(p_i) e^{ik_m a} \chi_m(p_j) \tag{4.8}$$

where $\chi_m(p_i)$ represents the transverse mode, $g(p_i, p_j, E)$ is the Green's function for an isolated lead between two points along an edge, p labels the isolated lead, and $\lambda = \hbar^2/2ma^2$ relates the spacing between lattice sites. The quantity,

$$\Gamma_p(i, j, E) = \sum_{m \in p} \chi_m(p_i) \frac{\hbar v_m}{a} \chi_m(p_j) \tag{4.9}$$

expresses the scattering rate and determines the rate of electron loss. Here k_m is the wavenumber for mode m, and v_m is the velocity for the mode, related to the energy E via the tight-binding

dispersion relation,

$$E = \varepsilon_m + 2\lambda\left[1 - \cos(k_m a)\right] \tag{4.10}$$

and the velocity given by,

$$\hbar v_m = \frac{\partial E}{\partial k_m} = 2a\lambda \sin(k_m a), \tag{4.11}$$

with ε_m being the cutoff energy for mode m.

Next, we obtain the inscattering and outscattering functions, whose sum equals Γ. Assuming each lead is in equilibrium with some Fermi distribution $f_p(E)$ we write

$$\Sigma_p^{\text{in}}(r_i, r_j, E) = f_p(E)\Gamma_p(r_i, r_j, E) \tag{4.12}$$

$$\Sigma_p^{\text{out}}(r_i, r_j, E) = (1 - f_p(E))\Gamma_p(r_i, r_j, E). \tag{4.13}$$

These expressions enable the evaluation of both the retarded Eq. (4.4), and advanced Eq. (4.5) Green's functions.

To carry out this computationally intensive step, we require the matrix representation of the conductor Hamiltonian, Eq (4.1). The local electron and spin densities are defined by Eqs. (4.2) and (4.3), respectively. Recall, both n_i and $\mathbf{m}_i$ are determined self-consistently.

Next, we compute the correlation functions:

$$G^{\text{n}} = G^{\text{R}}\Sigma^{\text{in}}G^{\text{A}} \tag{4.14}$$

$$G^{\text{p}} = G^{\text{R}}\Sigma^{\text{out}}G^{\text{A}}. \tag{4.15}$$

The scattering functions include contributions from both leads and interactions:

$$\Sigma^{\text{in}} = \left[\Sigma^{\text{in}}_{\varphi} + \sum_{p} \Sigma^{\text{in}}_{p} \right] \tag{4.16}$$

$$\Sigma^{\text{out}} = \left[\Sigma^{\text{out}}_{\varphi} + \sum_{p} \Sigma^{\text{out}}_{p} \right]. \tag{4.17}$$

Note that Σ_{φ} must be updated at each iteration.

The self-energy and scattering functions due to the interactions are calculated iteratively until convergence is achieved. At every step, we invert an $N \times N$ matrix for each energy channel, where the calculation depends on the temperature, bias, and correlation energy.

$$\Sigma^{\text{in}}_{\varphi}(\mathbf{r}, \mathbf{r}', \tau) = \overline{D}(\mathbf{r}, \mathbf{r}') G^{N}(\mathbf{r}, \mathbf{r}'), \tag{4.18}$$

where $\overline{D}(\mathbf{r}, \mathbf{r}')$ represents the spatial correlation and energy spectrum of phase breaking scatterers,

$$D(\mathbf{r}, \mathbf{r}', \hbar\omega) = \sum_{\mathbf{q}} |U_q|^2 \begin{bmatrix} -\exp\left[-i\mathbf{q}(\mathbf{r} - \mathbf{r}')\right] N_q \delta(\omega - \omega_q) \\ \exp\left[+i\mathbf{q}(\mathbf{r} - \mathbf{r}')\right] (N_q + 1) \delta(\omega - \omega_q) \end{bmatrix} \tag{4.19}$$

Although computationally intensive, this iterative procedure is essential for achieving self-consistency.

Having established the computational framework for the spin Hall effect with spin–orbit coupling and interactions, we now develop a complementary toy model that captures the essential role of edge states and their associated spin accumulation.

4.2 Toy Model

To complement the previous section, we here provide a minimal model to compute the spin accumulation response. In a metallic strip of finite width, electrons occupy states that can be classified as either edge or bulk states. In the low-energy limit of a topologically nontrivial material, only a few—or even a single—edge state contributes to conduction. Here, we investigate whether perturbing a single edge state can induce spin accumulation along the edges.

4.2.1 Symmetry Considerations

In this discussion we analyze how symmetry considerations constrain the system's response to spin accumulation in the presence of an external magnetic field h. We define the response to an applied magnetic field, Q_{ij}, as

$$Q_{ij} = \delta s_i x_j = \chi_{ijk} h_k, \tag{4.20}$$

where δs_i represents the i-th component of the spin accumulation, x_j is the j'th Cartesian component, and χ_{ijk} is the response tensor.

Under inversion, both δs_i and h_k remain invariant while the coordinate transforms as $x_j \rightarrow -x_j$. Thus, applying the inversion operator yields

$$I^{-1}\delta s_i I I^{-1} x_j I = I\chi_{ijk} I^{-1} I h_k I^{-1}, \tag{4.21}$$

which simplifies to

$$\delta s_i(-x_j) = \chi'_{ijk} h_k, \tag{4.22}$$

where χ'_{ijk} denotes the transformed response tensor. Comparing with the original definition sides, we obtain

$$-\chi_{ijk} = \chi'_{ijk}. \tag{4.23}$$

Therefore, if χijk were inversion symmetric – that is, if $\chi_{ijk} = \chi'_{ijk}$ – it would necessarily vanish. A nonzero spin accumulation in response to the applied h-field thus requires that the response tensor χ_{ijk} lacks inversion symmetry.

In particular, if we want an accumulation of δs_z, due to the z component of the **h** field,

$$\delta s_z x_j = \chi_{zjz} h_z \tag{4.24}$$

we see we would need some of the components of the row/column of χ_{zjz} to be non-zero. In the following section, we imagine a thin strip, of finite width along the y-component, which could mean we need χ_{zyz} in particular to be non-zero to accumulate δs_z.

4.2.2 Initializing the Hamiltonian

In the preceding section, we demonstrated that inversion symmetry must be broken to achieve spin accumulation. Consider the Hamiltonian:

$$H = H_0 + H_{\text{int}} \tag{4.25}$$

where

$$H_0 = \hbar v_k k \, \sigma_z \otimes \tau_z \tag{4.26}$$

is the free electron Hamiltonian, and

$$H_{\text{int}} = \Delta \, \sigma_k \otimes \tau_l \tag{4.27}$$

represents interaction Hamiltonian, with $k, l \in \{x, y, z\}$. Here σ_i are the Pauli matrices in spin space, and τ_i are the Pauli matrices in edge space (top edge vs bottom edge).

To examine the symmetry-breaking requirements of H_{int}, we consider the inversion operator I_i along the $i-$th Cartesian axis and the time-reversal operator T, defined as:

$$I_i = \{k \to -k\} \otimes \sigma_0 \otimes \tau_i; \quad i \in \{x, y\} \tag{4.28}$$

and

$$T = \{k \to -k\} \otimes \sigma_y \otimes \tau_0 \varkappa \tag{4.29}$$

where $\varkappa$ denotes complex conjugation.

For H_{int} to break inversion symmetry, it must satisfy

$$H'_{\text{int}} = I_i^{-1} H_{\text{int}} I_i \neq H_{int} \tag{4.30}$$

leading to

$$H'_{\text{int}} = \Delta\sigma_k \otimes \{\tau_i \tau_l \tau_i\}. \tag{4.31}$$

To break both I_x and I_y, we require $l = z$.

For time-reversal symmetry, we consider:

$$H'_{\text{int}} = T^{-1} H_{\text{int}} T = \Delta\sigma_y \sigma_k \sigma_y \otimes \tau_z \tag{4.32}$$

If $k = y$, $H' = H_{\text{int}}$, preserving time-reversal symmetry. Conversely, if $k = z$ (or $k = x$), then

$$H'_{\text{int}} = \Delta\sigma_y \sigma_z \sigma_y \otimes \tau_z = \Delta(-\sigma_z) \otimes \tau_z = -H_{\text{int}} \tag{4.33}$$

breaking time-reversal symmetry. This term correlates bands along the z-axis through σ_z.

While our complete framework provides a controlled way to initialize and explore the Hamiltonian, the resulting spin accumulation proved difficult to interpret. These challenges point toward the need for further refinements and motivate the directions outlined in the following section on future work.

4.3 Future Work

This work establishes clear parallel between the SHE and AHE emphasizing that the mechanisms underpinning both–intrinsic, skew scattering, and side jump–have analogous roles. However, for SHE, each contribution must take account for opposite spin orientations.

In systems with strong SOC, spin current is ill-defined due to the absence of spin conservation and a valid continuity equation. Instead, spin accumulation at material edges becomes the physically meaningful and measurable quantity. By incorporating on-site Hubbard interactions into

the tight-binding Kane-Mele model, the study provides a more complete and realistic description of spin transport in correlated systems. This combination of topological band structure and interaction is rarely tackled directly due to its complexity, but is essential for accurate modeling of experimental systems.

This study details a numerical framework using nonequilibrium Green's functions to compute spin accumulation in a finite strip geometry. The inclusion of self-consistent Hartree-Fock terms and full treatment of lead couplings allows for precise tracking of interaction effects on edge spin accumulation. A symmetry-based toy model confirms that inversion symmetry must be broken to observe a non-zero spin accumulation. This is consistent with expectations from linear response theory: the spin accumulation response tensor must be odd under inversion. We presented a minimal model that captures conditions for time-reversal and inversion symmetry breaking. This simplified two-band model shows that to produce edge spin accumulation we need two things. First, the Hamiltonian must include interaction terms coupling spin and edge degrees of freedom (e.g., $\sigma_z \otimes \tau_z$). Second these terms must break inversion and optionally break time-reversal symmetry, depending on the specific σ_k used.

While the Kane-Mele model and the Hubbard interaction are both well-studied, their combined impact on the spin Hall effect and spin accumulation has not been extensively explored. This work contributes a new method to compute spin accumulation in such systems, providing both numerical and analytical tools. The results point to the edge states of topological insulators as the key contributors to spin accumulation, especially under the influence of interactions and symmetry breaking—consistent with the expected behavior of quantum spin Hall systems.

This work provides a unified framework to understand how interactions modify the spin Hall response, focusing on spin accumulation rather than ill-defined spin currents in the strong SOC regime. It advances the field by offering a self-consistent computational method and toy model analysis that clarify how symmetry and interactions control spin accumulation in topological materials. Future work will be on elucidating the origin of an unexpected sign change of spin accumulation versus changing chemical potential in the NEGF calculation by using the toy model.

Bibliography

[1] C. Ard, E. Camrud, O. Pinaud, and C. Hua. Bounds and anomalies of inhomogeneous anomalous hall effects. *Commun Phys*, page 209, 2025.

[2] Ian P. Moseley, Christopher P. Ard, Joseph A. DiVerdi, Andrew Ozarowski, Hua Chen, and Joseph M. Zadrozny. Slowing magnetic relaxation with open-shell diluents. *Cell reports. Physical science*, 3(3):100802, March 2022.

[3] L. J. van der Pauw. A method of measuring specific resistivity and Hall effect of discs of arbitrary shape. *Philips Research Reports*, 13(2):1–9, 1958.

[4] A.B. Pippard. *Magnetoresistance in Metals*. Cambridge Studies in Low Temperature Physics. Cambridge University Press, 1989.

[5] M. M. Parish and P. B. Littlewood. Non-saturating magnetoresistance in heavily disordered semiconductors. *Nature*, 426(6963):162–165, Nov 2003.

[6] Meera M. Parish and Peter B. Littlewood. Classical magnetotransport of inhomogeneous conductors. *Phys. Rev. B*, 72:094417, Sep 2005.

[7] R. Xu, A. Husmann, T. F. Rosenbaum, M.-L. Saboungi, J. E. Enderby, and P. B. Littlewood. Large magnetoresistance in non-magnetic silver chalcogenides. *Nature*, 390(6655):57–60, Nov 1997.

[8] N. Kanazawa, Y. Onose, T. Arima, D. Okuyama, K. Ohoyama, S. Wakimoto, K. Kakurai, S. Ishiwata, and Y. Tokura. Large Topological Hall Effect in a Short-Period Helimagnet MnGe. *Phys. Rev. Lett.*, 106:156603, Apr 2011.

[9] Yufan Li, N. Kanazawa, X. Z. Yu, A. Tsukazaki, M. Kawasaki, M. Ichikawa, X. F. Jin, F. Kagawa, and Y. Tokura. Robust Formation of Skyrmions and Topological Hall Effect Anomaly in Epitaxial Thin Films of MnSi. *Phys. Rev. Lett.*, 110:117202, Mar 2013.

[10] Jobu Matsuno, Naoki Ogawa, Kenji Yasuda, Fumitaka Kagawa, Wataru Koshibae, Naoto Nagaosa, Yoshinori Tokura, and Masashi Kawasaki. Interface-driven topological Hall effect in $SrRuO_3$-$SrIrO_3$ bilayer. *Science Advances*, 2(7):e1600304, 2016.

[11] Anjan Soumyanarayanan, M. Raju, A. L. Gonzalez Oyarce, Anthony K. C. Tan, Mi-Young Im, A. P. Petrović, Pin Ho, K. H. Khoo, M. Tran, C. K. Gan, F. Ernult, and C. Panagopoulos. Tunable room-temperature magnetic skyrmions in Ir/Fe/Co/Pt multilayers. *Nature Materials*, 16(9):898–904, September 2017.

[12] Davide Maccariello, William Legrand, Nicolas Reyren, Karin Garcia, Karim Bouzehouane, Sophie Collin, Vincent Cros, and Albert Fert. Electrical detection of single magnetic skyrmions in metallic multilayers at room temperature. *Nature Nanotechnology*, 13(3):233–237, March 2018.

[13] Katharina Zeissler, Simone Finizio, Kowsar Shahbazi, Jamie Massey, Fatma Al Ma'Mari, David M. Bracher, Armin Kleibert, Mark C. Rosamond, Edmund H. Linfield, Thomas A. Moore, Jörg Raabe, Gavin Burnell, and Christopher H. Marrows. Discrete Hall resistivity contribution from Néel skyrmions in multilayer nanodiscs. *Nature Nanotechnology*, 13(12):1161–1166, December 2018.

[14] M. Raju, A. Yagil, Anjan Soumyanarayanan, Anthony K. C. Tan, A. Almoalem, Fusheng Ma, O. M. Auslaender, and C. Panagopoulos. The evolution of skyrmions in Ir/Fe/Co/Pt multilayers and their topological Hall signature. *Nature Communications*, 10(1):696, March 2019.

[15] Y. Ohuchi, Y. Kozuka, M. Uchida, K. Ueno, A. Tsukazaki, and M. Kawasaki. Topological Hall effect in thin films of the Heisenberg ferromagnet EuO. *Physical Review B*, 91(24):245115, June 2015.

[16] Qiming Shao, Yawen Liu, Guoqiang Yu, Se Kwon Kim, Xiaoyu Che, Chi Tang, Qing Lin He, Yaroslav Tserkovnyak, Jing Shi, and Kang L. Wang. Topological Hall effect at above

room temperature in heterostructures composed of a magnetic insulator and a heavy metal. *Nature Electronics*, 2(5):182–186, May 2019.

[17] Adam S. Ahmed, Aidan J. Lee, Nuria Bagués, Brendan A. McCullian, Ahmed M. A. Thabt, Avery Perrine, Po-Kuan Wu, James R. Rowland, Mohit Randeria, P. Chris Hammel, David W. McComb, and Fengyuan Yang. Spin-Hall Topological Hall Effect in Highly Tunable Pt/Ferrimagnetic-Insulator Bilayers. *Nano Letters*, 19(8):5683–5688, August 2019.

[18] Bin Pang, Lunyong Zhang, Y. B. Chen, Jian Zhou, Shuhua Yao, Shantao Zhang, and Yanfeng Chen. Spin-Glass-Like Behavior and Topological Hall Effect in SrRuO3/SrIrO3 Superlattices for Oxide Spintronics Applications. *ACS Applied Materials & Interfaces*, 9(3):3201–3207, January 2017.

[19] Yuki Ohuchi, Jobu Matsuno, Naoki Ogawa, Yusuke Kozuka, Masaki Uchida, Yoshinori Tokura, and Masashi Kawasaki. Electric-field control of anomalous and topological Hall effects in oxide bilayer thin films. *Nature Communications*, 9(1):213, January 2018.

[20] Byungmin Sohn, Bongju Kim, Se Young Park, Hwan Young Choi, Jae Young Moon, Taeyang Choi, Young Jai Choi, Hua Zhou, Jun Woo Choi, Alessandro Bombardi, Dan. G. Porter, Seo Hyoung Chang, Jung Hoon Han, and Changyoung Kim. Stable humplike Hall effect and noncoplanar spin textures in $\mathrm{SrRuO_3}$ ultrathin films. *Phys. Rev. Res.*, 3:023232, Jun 2021.

[21] Lingfei Wang, Qiyuan Feng, Yoonkoo Kim, Rokyeon Kim, Ki Hoon Lee, Shawn D. Pollard, Yeong Jae Shin, Haibiao Zhou, Wei Peng, Daesu Lee, Wenjie Meng, Hyunsoo Yang, Jung Hoon Han, Miyoung Kim, Qingyou Lu, and Tae Won Noh. Ferroelectrically tunable magnetic skyrmions in ultrathin oxide heterostructures. *Nature Materials*, 17(12):1087–1094, December 2018.

[22] Qing Qin, Liang Liu, Weinan Lin, Xinyu Shu, Qidong Xie, Zhishiuh Lim, Changjian Li, Shikun He, Gan Moog Chow, and Jingsheng Chen. Emergence of Topological Hall Effect

in a SrRuO3 Single Layer. *Advanced Materials (Deerfield Beach, Fla.)*, 31(8):e1807008, February 2019.

[23] Keng-Yuan Meng, Adam S. Ahmed, Mirko Baćani, Andrada-Oana Mandru, Xue Zhao, Núria Bagués, Bryan D. Esser, Jose Flores, David W. McComb, Hans J. Hug, and Fengyuan Yang. Observation of Nanoscale Skyrmions in SrIrO3/SrRuO3 Bilayers. *Nano Letters*, 19(5):3169–3175, May 2019.

[24] Youdi Gu, Yi-Wen Wei, Kun Xu, Hongrui Zhang, Fei Wang, Fan Li, Muhammad Shahrukh Saleem, Cui-Zu Chang, Jirong Sun, Cheng Song, Ji Feng, Xiaoyan Zhong, Wei Liu, Zhidong Zhang, Jing Zhu, and Feng Pan. Interfacial oxygen-octahedral-tilting-driven electrically tunable topological Hall effect in ultrathin SrRuO3 films. *Journal of Physics D: Applied Physics*, 52(40):404001, July 2019.

[25] Wenbo Wang, Matthew W. Daniels, Zhaoliang Liao, Yifan Zhao, Jun Wang, Gertjan Koster, Guus Rijnders, Cui-Zu Chang, Di Xiao, and Weida Wu. Spin chirality fluctuation in two-dimensional ferromagnets with perpendicular magnetic anisotropy. *Nature Materials*, 18(10):1054–1059, October 2019.

[26] Byungmin Sohn, Bongju Kim, Jun Woo Choi, Seo Hyoung Chang, Jung Hoon Han, and Changyoung Kim. Hump-like structure in Hall signal from ultra-thin $SrRuO_3$ films without inhomogeneous anomalous Hall effect. *Current Applied Physics*, 20(1):186–190, January 2020.

[27] P. Zhang, A. Das, E. Barts, M. Azhar, L. Si, K. Held, M. Mostovoy, and T. Banerjee. Robust skyrmion-bubble textures in $\mathrm{SrRuO_3}$ thin films stabilized by magnetic anisotropy. *Phys. Rev. Res.*, 2:032026, Jul 2020.

[28] Changan Wang, Ching-Hao Chang, Andreas Herklotz, Chao Chen, Fabian Ganss, Ulrich Kentsch, Deyang Chen, Xingsen Gao, Yu-Jia Zeng, Olav Hellwig, Manfred Helm,

Sibylle Gemming, Ying-Hao Chu, and Shengqiang Zhou. Topological Hall Effect in Single Thick SrRuO3 Layers Induced by Defect Engineering. *Advanced Electronic Materials*, 6(6):2000184, 2020.

[29] Donghan Kim, Byungmin Sohn, Minsoo Kim, Sungsoo Hahn, Youngdo Kim, Jong Hyuk Kim, Young Jai Choi, and Changyoung Kim. Capping and gate control of anomalous Hall effect and hump structure in ultra-thin SrRuO3 films. *Applied Physics Letters*, 118(17):173102, 04 2021.

[30] Hai Huang, Sang-Jun Lee, Bongju Kim, Byungmin Sohn, Changyoung Kim, Chi-Chang Kao, and Jun-Sik Lee. Detection of the Chiral Spin Structure in Ferromagnetic SrRuO3 Thin Film. *ACS Applied Materials & Interfaces*, 12(33):37757–37763, 2020. PMID: 32696641.

[31] Zhuolu Li, Shengchun Shen, Zijun Tian, Kyle Hwangbo, Meng Wang, Yujia Wang, F. Michael Bartram, Liqun He, Yingjie Lyu, Yongqi Dong, Gang Wan, Haobo Li, Nianpeng Lu, Jiadong Zang, Hua Zhou, Elke Arenholz, Qing He, Luyi Yang, Weidong Luo, and Pu Yu. Reversible manipulation of the magnetic state in SrRuO3 through electric-field controlled proton evolution. *Nature Communications*, 11(1):184, January 2020.

[32] Lorenzo Vistoli, Wenbo Wang, Anke Sander, Qiuxiang Zhu, Blai Casals, Rafael Cichelero, Agnès Barthélémy, Stéphane Fusil, Gervasi Herranz, Sergio Valencia, Radu Abrudan, Eugen Weschke, Kazuki Nakazawa, Hiroshi Kohno, Jacobo Santamaria, Weida Wu, Vincent Garcia, and Manuel Bibes. Giant topological Hall effect in correlated oxide thin films. *Nature Physics*, 15(1):67–72, January 2019.

[33] M. Raju, A. P. Petrović, A. Yagil, K. S. Denisov, N. K. Duong, B. Göbel, E. Şaşıoğlu, O. M. Auslaender, I. Mertig, I. V. Rozhansky, and C. Panagopoulos. Colossal topological Hall effect at the transition between isolated and lattice-phase interfacial skyrmions. *Nature Communications*, 12(1):2758, May 2021.

[34] M. V. Sapozhnikov, N. S. Gusev, S. A. Gusev, D. A. Tatarskiy, Yu. V. Petrov, A. G. Temiryazev, and A. A. Fraerman. Direct observation of topological Hall effect in Co/Pt nanostructured films. *Physical Review B*, 103(5):054429, February 2021.

[35] Jue Jiang, Di Xiao, Fei Wang, Jae-Ho Shin, Domenico Andreoli, Jianxiao Zhang, Run Xiao, Yi-Fan Zhao, Morteza Kayyalha, Ling Zhang, Ke Wang, Jiadong Zang, Chaoxing Liu, Nitin Samarth, Moses H. W. Chan, and Cui-Zu Chang. Concurrence of quantum anomalous Hall and topological Hall effects in magnetic topological insulator sandwich heterostructures. *Nature Materials*, 19(7):732–737, July 2020.

[36] Xue Ren, Liang Liu, Bin Cui, Bin Cheng, Xiangxiang Zhao, Taiyu An, Ruiyue Chu, Mingfang Zhang, Weikang Liu, Guangjun Zhou, Weijie Kuai, and Jifan Hu. The Topological Hall Effect in CoGd Films Controlled by Hydrogen Migration under Gate Voltage. *Advanced Electronic Materials*, 10(5):2300752, 2024.

[37] Graham Kimbell, Changyoung Kim, Weida Wu, Mario Cuoco, and Jason W. A. Robinson. Challenges in identifying chiral spin textures via the topological Hall effect. *Communications Materials*, 3(1):1–18, 2022.

[38] Mengyun He, Yu Huang, Huimin Sun, Yu Fu, Peng Zhang, Kang L Wang, and Qing Lin He. Probing the percolation in the quantum anomalous Hall insulator. *New Journal of Physics*, 25(3):033003, mar 2023.

[39] Yi-Fan Zhao, Ruoxi Zhang, Ling-Jie Zhou, Ruobing Mei, Zi-Jie Yan, Moses H. W. Chan, Chao-Xing Liu, and Cui-Zu Chang. Zero Magnetic Field Plateau Phase Transition in Higher Chern Number Quantum Anomalous Hall Insulators. *Phys. Rev. Lett.*, 128:216801, May 2022.

[40] R. Y. Chen, R. Q. Zhang, Y. J. Zhou, H. Bai, F. Pan, and C. Song. Magnetic field direction dependence of topological Hall effect like features in synthetic ferromagnetic and antiferromagnetic multilayers. *Applied Physics Letters*, 116(24):242403, 06 2020.

[41] Meri Algarni, Cheng Tan, Guolin Zheng, Sultan Albarakati, Xiangde Zhu, James Partridge, Yanglin Zhu, Lawrence Farrar, Mingliang Tian, Jianhui Zhou, Xiaolin Wang, Zhiqiang Mao, and Lan Wang. Tunable artificial topological Hall effects in van der Waals heterointerfaces. *Phys. Rev. B*, 105:155407, Apr 2022.

[42] Chunjie Yan, Zui Tao, Zhenyu Gao, Zishuang Li, Xiao Xiao, Haozhe Wang, Lina Chen, and Ronghua Liu. Topological Hall-like magnetoresistance humps in anomalous Hall loops caused by planar Hall effect. *Phys. Rev. B*, 108:094414, Sep 2023.

[43] Jihang Yu, Liang Liu, Jinyu Deng, Chenghang Zhou, Hongxi Liu, Francis Poh, and Jingsheng Chen. Topological Hall effect in ferrimagnetic CoTb single layer. *Journal of Magnetism and Magnetic Materials*, 487:165316, 2019.

[44] Vivek Kumar, Nitesh Kumar, Manfred Reehuis, Jacob Gayles, A. S. Sukhanov, Andreas Hoser, Fran çoise Damay, Chandra Shekhar, Peter Adler, and Claudia Felser. Detection of antiskyrmions by topological Hall effect in Heusler compounds. *Phys. Rev. B*, 101:014424, Jan 2020.

[45] Subir Sen, Charanpreet Singh, Prashanta K. Mukharjee, Ramesh Nath, and Ajaya K. Nayak. Observation of the topological Hall effect and signature of room-temperature antiskyrmions in Mn-Ni-Ga D_{2d} Heusler magnets. *Phys. Rev. B*, 99:134404, Apr 2019.

[46] Daisuke Kan, Takahiro Moriyama, and Yuichi Shimakawa. Field-sweep-rate and time dependence of transverse resistivity anomalies in ultrathin $\mathrm{SrRuO_3}$ films. *Phys. Rev. B*, 101:014448, Jan 2020.

[47] Lena Wysocki, Lin Yang, Felix Gunkel, Regina Dittmann, Paul H. M. van Loosdrecht, and Ionela Lindfors-Vrejoiu. Validity of magnetotransport detection of skyrmions in epitaxial $\mathrm{srruo_3}$ heterostructures. *Phys. Rev. Materials*, 4:054402, May 2020.

[48] Bin Jia, Shuai Zhang, Zhe Ying, Hangkai Xie, Bo Chen, Muhammad Naveed, Fucong Fei, Minhao Zhang, Danfeng Pan, and Fengqi Song. Unconventional anomalous Hall effect in

magnetic topological insulator $MnBi_4Te_7$ device. *Applied Physics Letters*, 118(8):083101, 2021.

[49] Chang Liu, Yunyi Zang, Wei Ruan, Yan Gong, Ke He, Xucun Ma, Qi-Kun Xue, and Yayu Wang. Dimensional Crossover-Induced Topological Hall Effect in a Magnetic Topological Insulator. *Phys. Rev. Lett.*, 119:176809, Oct 2017.

[50] Yang Cheng, Sisheng Yu, Menglin Zhu, Jinwoo Hwang, and Fengyuan Yang. Evidence of the Topological Hall Effect in Pt/Antiferromagnetic Insulator Bilayers. *Phys. Rev. Lett.*, 123:237206, Dec 2019.

[51] Praveen Vir, Jacob Gayles, A. S. Sukhanov, Nitesh Kumar, Fran çoise Damay, Yan Sun, Jürgen Kübler, Chandra Shekhar, and Claudia Felser. Anisotropic topological Hall effect with real and momentum space Berry curvature in the antiskrymion-hosting Heusler compound $\mathrm{Mn_{1.4}PtSn}$. *Phys. Rev. B*, 99:140406, Apr 2019.

[52] Charles S. Spencer, Jacob Gayles, Nicholas A. Porter, Satoshi Sugimoto, Zabeada Aslam, Christian J. Kinane, Timothy R. Charlton, Frank Freimuth, Stanislav Chadov, Sean Langridge, Jairo Sinova, Claudia Felser, Stefan Blügel, Yuriy Mokrousov, and Christopher H. Marrows. Helical magnetic structure and the anomalous and topological Hall effects in epitaxial B20 $\mathrm{Fe_{1-y}Co_yGe}$ films. *Phys. Rev. B*, 97:214406, Jun 2018.

[53] Wenbo Wang, Yi-Fan Zhao, Fei Wang, Matthew W. Daniels, Cui-Zu Chang, Jiadong Zang, Di Xiao, and Weida Wu. Chiral-Bubble-Induced Topological Hall Effect in Ferromagnetic Topological Insulator Heterostructures. *Nano Letters*, 21(2):1108–1114, January 2021.

[54] Debangsu Roy, Noam Haham, James W. Reiner, Efrat Shimshoni, and Lior Klein. Intermixing of ordinary and anomalous Hall effect in $\mathrm{SrRuO_3}$. *Phys. Rev. B*, 92:235101, Dec 2015.

[55] Di Tian, Zhiwei Liu, Shengchun Shen, Zhuolu Li, Yu Zhou, Hongquan Liu, Hanghui Chen, and Pu Yu. Manipulating Berry curvature of $SrRuO_3$ thin films via epitaxial strain. *Proceedings of the National Academy of Sciences*, 118(18):e2101946118, 2021.

[56] J. C. Gallagher, K. Y. Meng, J. T. Brangham, H. L. Wang, B. D. Esser, D. W. McComb, and F. Y. Yang. Robust Zero-Field Skyrmion Formation in FeGe Epitaxial Thin Films. *Phys. Rev. Lett.*, 118:027201, Jan 2017.

[57] T. Yokouchi, N. Kanazawa, A. Tsukazaki, Y. Kozuka, M. Kawasaki, M. Ichikawa, F. Kagawa, and Y. Tokura. Stability of two-dimensional skyrmions in thin films of $Mn_{1-x}Fe_xSi$ investigated by the topological Hall effect. *Physical Review B*, 89(6):064416, February 2014.

[58] Gerald Malsch, Dmytro Ivaneyko, Peter Milde, Lena Wysocki, Lin Yang, Paul H. M. van Loosdrecht, Ionela Lindfors-Vrejoiu, and Lukas M. Eng. Correlating the Nanoscale Structural, Magnetic, and Magneto-Transport Properties in SrRuO3-Based Perovskite Thin Films: Implications for Oxide Skyrmion Devices. *ACS Applied Nano Materials*, 3(2):1182–1190, February 2020.

[59] S. Mühlbauer, B. Binz, F. Jonietz, C. Pfleiderer, A. Rosch, A. Neubauer, R. Georgii, and P. Böni. Skyrmion Lattice in a Chiral Magnet. *Science*, 323(5916):915–919, 2009.

[60] Jinwu Ye, Yong Baek Kim, A. J. Millis, B. I. Shraiman, P. Majumdar, and Z. Tešanović. Berry Phase Theory of the Anomalous Hall Effect: Application to Colossal Magnetoresistance Manganites. *Phys. Rev. Lett.*, 83:3737–3740, Nov 1999.

[61] P. Bruno, V. K. Dugaev, and M. Taillefumier. Topological Hall Effect and Berry Phase in Magnetic Nanostructures. *Physical Review Letters*, 93(9):096806, 2004.

[62] Y. Taguchi, Y. Oohara, H. Yoshizawa, N. Nagaosa, and Y. Tokura. Spin Chirality, Berry Phase, and Anomalous Hall Effect in a Frustrated Ferromagnet. *Science*, 291(5513):2573–2576, 2001.

[63] Masaru Onoda, Gen Tatara, and Naoto Nagaosa. Anomalous Hall Effect and Skyrmion Number in Real and Momentum Spaces. *Journal of the Physical Society of Japan*, 73(10):2624–2627, 2004.

[64] Naoto Nagaosa and Yoshinori Tokura. Topological properties and dynamics of magnetic skyrmions. *Nature Nanotechnology*, 8(12):899–911, Dec 2013.

[65] Daisuke Kan, Takahiro Moriyama, Kento Kobayashi, and Yuichi Shimakawa. Alternative to the topological interpretation of the transverse resistivity anomalies in $\mathrm{SrRuO_3}$. *Phys. Rev. B*, 98:180408, Nov 2018.

[66] A. Gerber. Interpretation of experimental evidence of the topological Hall effect. *Phys. Rev. B*, 98:214440, Dec 2018.

[67] D. J. Groenendijk, C. Autieri, T. C. van Thiel, W. Brzezicki, J. R. Hortensius, D. Afanasiev, N. Gauquelin, P. Barone, K. H. W. van den Bos, S. van Aert, J. Verbeeck, A. Filippetti, S. Picozzi, M. Cuoco, and A. D. Caviglia. Berry phase engineering at oxide interfaces. *Phys. Rev. Research*, 2:023404, Jun 2020.

[68] K. M. Fijalkowski, M. Hartl, M. Winnerlein, P. Mandal, S. Schreyeck, K. Brunner, C. Gould, and L. W. Molenkamp. Coexistence of Surface and Bulk Ferromagnetism Mimics Skyrmion Hall Effect in a Topological Insulator. *Phys. Rev. X*, 10:011012, Jan 2020.

[69] Graham Kimbell, Paul M. Sass, Bart Woltjes, Eun Kyo Ko, Tae Won Noh, Weida Wu, and Jason W. A. Robinson. Two-channel anomalous Hall effect in $\mathrm{SrRuO_3}$. *Phys. Rev. Materials*, 4:054414, May 2020.

[70] Gideok Kim, K. Son, Y. E. Suyolcu, L. Miao, N. J. Schreiber, H. P. Nair, D. Putzky, M. Minola, G. Christiani, P. A. van Aken, K. M. Shen, D. G. Schlom, G. Logvenov, and B. Keimer. Inhomogeneous ferromagnetism mimics signatures of the topological Hall effect in $\mathrm{SrRuO_3}$ films. *Physical Review Materials*, 4(10):104410, October 2020.

[71] Lin Yang, Lena Wysocki, Jörg Schöpf, Lei Jin, András Kovács, Felix Gunkel, Regina Dittmann, Paul H. M. van Loosdrecht, and Ionela Lindfors-Vrejoiu. Origin of the hump anomalies in the Hall resistance loops of ultrathin $SrRuO_3/SrIrO_3$ multilayers. *Phys. Rev. Mater.*, 5:014403, Jan 2021.

[72] Ludi Miao, Nathaniel J. Schreiber, Hari P. Nair, Berit H. Goodge, Shengwei Jiang, Jacob P. Ruf, Yonghun Lee, Matthew Fu, Boris Tsang, Yingfei Li, Cyrus Zeledon, Jie Shan, Kin Fai Mak, Lena F. Kourkoutis, Darrell G. Schlom, and Kyle M. Shen. Strain relaxation induced transverse resistivity anomalies in $SrRuO_3$ thin films. *Phys. Rev. B*, 102:064406, Aug 2020.

[73] E.H. Hall. XVIII. On the "Rotational Coefficient" in nickel and cobalt. *The London, Edinburgh, and Dublin Philosophical Magazine and Journal of Science*, 12(74):157–172, 1881.

[74] Robert Karplus and J. M. Luttinger. Hall Effect in Ferromagnetics. *Phys. Rev.*, 95:1154–1160, Sep 1954.

[75] J. Smit. The spontaneous Hall effect in ferromagnetics II. *Physica*, 24(1):39–51, 1958.

[76] L. Berger. Side-Jump Mechanism for the Hall Effect of Ferromagnets. *Phys. Rev. B*, 2:4559–4566, Dec 1970.

[77] T. Jungwirth, Qian Niu, and A. H. MacDonald. Anomalous Hall Effect in Ferromagnetic Semiconductors. *Phys. Rev. Lett.*, 88:207208, May 2002.

[78] Ryuichi Shindou and Naoto Nagaosa. Orbital Ferromagnetism and Anomalous Hall Effect in Antiferromagnets on the Distorted fcc Lattice. *Phys. Rev. Lett.*, 87:116801, Aug 2001.

[79] Naoto Nagaosa, Jairo Sinova, Shigeki Onoda, A. H. MacDonald, and N. P. Ong. Anomalous Hall effect. *Rev. Mod. Phys.*, 82:1539–1592, May 2010.

[80] Takeshi Tomizawa and Hiroshi Kontani. Anomalous Hall effect in the t_{2g} orbital kagome lattice due to noncollinearity: Significance of the orbital Aharonov-Bohm effect. *Phys. Rev. B*, 80:100401, Sep 2009.

[81] Hua Chen, Qian Niu, and A. H. MacDonald. Anomalous Hall Effect Arising from Noncollinear Antiferromagnetism. *Phys. Rev. Lett.*, 112:017205, Jan 2014.

[82] J. Kübler and C. Felser. Non-collinear antiferromagnets and the anomalous Hall effect. *EPL (Europhysics Letters)*, 108(6):67001, dec 2014.

[83] Satoru Nakatsuji, Naoki Kiyohara, and Tomoya Higo. Large anomalous Hall effect in a non-collinear antiferromagnet at room temperature. *Nature*, 527(7577):212–215, Nov 2015.

[84] Fei Wang, Xuepeng Wang, Yi-Fan Zhao, Di Xiao, Ling-Jie Zhou, Wei Liu, Zhidong Zhang, Weiwei Zhao, Moses H. W. Chan, Nitin Samarth, Chaoxing Liu, Haijun Zhang, and Cui-Zu Chang. Interface-induced sign reversal of the anomalous Hall effect in magnetic topological insulator heterostructures. *Nature Communications*, 12(1):79, January 2021.

[85] Lingfei Wang, Qiyuan Feng, Han Gyeol Lee, Eun Kyo Ko, Qingyou Lu, and Tae Won Noh. Controllable Thickness Inhomogeneity and Berry Curvature Engineering of Anomalous Hall Effect in SrRuO3 Ultrathin Films. *Nano Letters*, 20(4):2468–2477, April 2020.

[86] Ruxin Liu, Ruijie Xu, Yequan Chen, Liqi Zhou, Wenzhuo Zhuang, Xu Zhang, Chong Zhang, Zhongqiang Chen, Liming Chen, and Xuefeng Wang. Interface-induced transverse resistivity anomaly in AgNbO3/SrRuO3 heterostructures. *APL Materials*, 12(2):021122, February 2024.

[87] M. B. Isichenko. Percolation, statistical topography, and transport in random media. *Rev. Mod. Phys.*, 64:961–1043, Oct 1992.

[88] Graeme W. Milton. *The Theory of Composites*. Cambridge Monographs on Applied and Computational Mathematics. Cambridge University Press, 2002.

[89] Joseph B. Keller. A Theorem on the Conductivity of a Composite Medium. *Journal of Mathematical Physics*, 5(4):548–549, 1964.

[90] A. M. Dykhne. Conductivity of a Two-dimensional Two-phase System. *Soviet Journal of Experimental and Theoretical Physics*, 32:63, 1971.

[91] A. M. Dykhne. Anomalous Plasma Resistance in a Strong Magnetic Field. *Soviet Journal of Experimental and Theoretical Physics*, 32:348, 1971.

[92] Kenneth S. Mendelson. A theorem on the effective conductivity of a two-dimensional heterogeneous medium. *Journal of Applied Physics*, 46(11):4740–4741, 1975.

[93] G. W. Milton. Classical Hall effect in two-dimensional composites: A characterization of the set of realizable effective conductivity tensors. *Phys. Rev. B*, 38:11296–11303, Dec 1988.

[94] Z. Hashin and S. Shtrikman. A Variational Approach to the Theory of the Effective Magnetic Permeability of Multiphase Materials. *Journal of Applied Physics*, 33(10):3125–3131, 1962.

[95] Leonid Berlyand and Volodymyr Rybalko. *Getting acquainted with homogenization and multiscale*. Compact Textbooks in Mathematics. Birkhäuser/Springer, Cham, 2018.

[96] K. H. J. Buschow. Magnetic properties of amorphous rare-earth–cobalt alloys. *Journal of Applied Physics*, 51(5):2795–2798, 05 1980.

[97] T. Katayama Y. J. Choe, S. Tsunashima and S. Uchiyama. Magneto-Optic Kerr Spectra Of Amorphous RE-Co Thin Films. *J. Magn. Soc. Jpn.*, 11:Supplement, No. S1 273–276, 1987.

[98] P. Hansen, C. Clausen, G. Much, M. Rosenkranz, and K. Witter. Magnetic and magneto-optical properties of rare-earth transition-metal alloys containing Gd, Tb, Fe, Co. *Journal of Applied Physics*, 66(2):756–767, 07 1989.

[99] Joseph Finley and Luqiao Liu. Spin-Orbit-Torque Efficiency in Compensated Ferrimagnetic Cobalt-Terbium Alloys. *Phys. Rev. Appl.*, 6:054001, Nov 2016.

[100] Zheng-Yu Xiao, Zhi-Yong Quan, Wei Zhang, Dong Li, Hui-Hui Liu, Guo-Wei Zhou, Jun Zhang, Fei Zhang, Xia Liu, Xiao-Hong Xu, and Ming-Zhong Wu. Experimental observation of topological Hall effects in compensated ferrimagnet-heavy metal layered structures. *Science China Physics, Mechanics & Astronomy*, 64(8):287511, Jun 2021.

[101] Peter M. Levy and Shufeng Zhang. Resistivity due to Domain Wall Scattering. *Phys. Rev. Lett.*, 79:5110–5113, Dec 1997.

[102] Anders Logg, Kent-Andre Mardal, Garth N. Wells, et al. *Automated Solution of Differential Equations by the Finite Element Method*. Springer, 2012.

[103] Ilan T. Rosen, Molly P. Andersen, Linsey K. Rodenbach, Lixuan Tai, Peng Zhang, Kang L. Wang, M. A. Kastner, and David Goldhaber-Gordon. Measured Potential Profile in a Quantum Anomalous Hall System Suggests Bulk-Dominated Current Flow. *Phys. Rev. Lett.*, 129:246602, Dec 2022.

[104] G. M. Ferguson, Run Xiao, Anthony R. Richardella, David Low, Nitin Samarth, and Katja C. Nowack. Direct visualization of electronic transport in a quantum anomalous Hall insulator. *Nature Materials*, 22(9):1100–1105, Sep 2023.

[105] Dante Gatteschi, Roberta Sessoli, and Jacques Villain. *Molecular Nanomagnets*. Oxford University Press, 03 2006.

[106] Jörg Lehmann, Alejandro Gaita-Ariño, Eugenio Coronado, and Daniel Loss. Quantum computing with molecular spin systems. *J. Mater. Chem.*, 19:1672–1677, 2009.

[107] Guillem Aromí, David Aguilà, Patrick Gamez, Fernando Luis, and Olivier Roubeau. Design of magnetic coordination complexes for quantum computing. *Chem. Soc. Rev.*, 41:537–546, 2012.

[108] S Thiele, F Balestro, R Ballou, S Klyatskaya, M Ruben, and W Wernsdorfer. Electrically driven nuclear spin resonance in single-molecule magnets. *Science*, pages 1135–1138, 2014.

[109] Jessica Wahsner, Eric M. Gale, Aurora Rodríguez-Rodríguez, and Peter Caravan. Chemistry of mri contrast agents: Current challenges and new frontiers. *Chemical Reviews*, 119(2):957–1057, 2019.

[110] van der Meer M Atanasov M Hakl M Orlita M Neugebauer P Neese F Sarkar B van Slageren J Rechkemmer Y, Breitgoff FD. A four-coordinate cobalt(ii) single-ion magnet with coercivity and a very high energy barrier. *Nature Communications*, 2016.

[111] Nippe M. Slow Latendresse TP, Bhuvanesh NS. Magnetic relaxation in a lanthanide-[1]metallocenophane complex. *Journal of the American Chemical Society*, 2017.

[112] S. Cardona-Serra, J. M. Clemente-Juan, E. Coronado, A. Gaita-Ariño, A. Camón, M. Evangelisti, F. Luis, M. J. Martínez-Pérez, and J. Sesé. Lanthanoid Single-Ion Magnets Based on Polyoxometalates with a 5-fold Symmetry: The Series [LnP5W30O110]12– (Ln3+ = Tb, Dy, Ho, Er, Tm, and Yb). *Journal of the American Chemical Society*, 134(36):14982–14990, September 2012. Publisher: American Chemical Society.

[113] Yan-Cong Chen, Jun-Liang Liu, Liviu Ungur, Jiang Liu, Quan-Wen Li, Long-Fei Wang, Zhao-Ping Ni, Liviu F Chibotaru, Xiao-Ming Chen, and Ming-Liang Tong. Symmetry-supported magnetic blocking at 20 k in pentagonal bipyramidal dy(iii) single-ion magnets. *Journal of the American Chemical Society*, 138(8):2829—2837, March 2016.

[114] Naoto Ishikawa, Miki Sugita, Tadahiko Ishikawa, Shin ya Koshihara, and Youkoh Kaizu. Lanthanide double-decker complexes functioning as magnets at the single-molecular level. *Journal of the American Chemical Society*, 125 29:8694–5, 2003.

[115] Fu-Sheng Guo, Benjamin M. Day, Yan-Cong Chen, Ming-Liang Tong, Akseli Mansikkamäki, and Richard A. Layfield. Magnetic hysteresis up to 80 kelvin in a dysprosium metallocene single-molecule magnet. *Science*, 362(6421):1400–1403, 2018.

[116] Conrad A P Goodwin, Fabrizio Ortu, Daniel Reta, Nicholas F Chilton, and David P Mills. Molecular magnetic hysteresis at 60 kelvin in dysprosocenium. *Nature*, 548(7668):439—442, August 2017.

[117] Lawrence J. Berliner, Gareth R. Eaton, and Sandra S. Eaton. Distance measurements in biological systems by epr. In *Biological magnetic resonance*, 2002.

[118] D. A. Garanin. Dipolar-controlled spin tunneling and relaxation in molecular magnets. 2012.

[119] D. Gatteschi and R. Sessoli. Quantum Tunneling of Magnetization and Related Phenomena in Molecular Materials. *Angewandte Chemie International*, 42(3):268–297, 2003.

[120] R. Sessoli, D. Gatteschi, and A. Caneschi. Magnetic bistability in a metal-ion cluster. *Nature*, 365:141–143, 1993.

[121] Roberta Sessoli, Hui Lien Tsai, Ann R. Schake, Sheyi Wang, John B. Vincent, Kirsten Folting, Dante Gatteschi, George Christou, and David N. Hendrickson. High-spin molecules: [Mn_{12}O_{12}(O_2cr)_{16}(H_2o)_4]. *Journal of the American Chemical Society*, 115(5):1804–1816, March 1993. Publisher: American Chemical Society.

[122] Joseph M. Zadrozny and Jeffrey R. Long. Slow magnetic relaxation at zero field in the tetrahedral complex [co(sph)4]2–. *Journal of the American Chemical Society*, 133(51):20732–20734, 2011. PMID: 22142241.

[123] D. Attanasio, I. Collamati, and C. Daul. EPR properties of a cobalt(II) complex containing a low-symmetry porphyrin-like ligand. *Inorganic Chemistry*, 24:2746–2750, 2005.

[124] I. Bhowmick, A.J. Roehl, J.R. Neilson, A.K. Rappé, and M.P. Shores. Slow magnetic relaxation in octahedral low-spin Ni(III). *Chemical Science*, 9(31):6564–6571, 2018.

[125] F. Habib, P.H. Lin, J. Long, I. Korobkov, and W. Wernsdorfer. The use of magnetic dilution to elucidate the slow magnetic relaxation effects of a Dy2 single-molecule magnet. *Am Chem Soc.*, 133(23):8830–8833, June 2011.

[126] F. Luis, M.J. Martínez-Pérez, O. Montero, E. Coronado, S. Cardona-Serra, C. Marti-Gastaldo, J.M. Clemente-Juan, J. Sesé, D. Drung, and T. Schurig. Spin-lattice relaxation via quantum tunneling in an Er^{3+}-polyoxometalate molecular magnet. *Phys. Rev. B - Condens. Matter Mater. Phys.*, 82:3–6, 2010.

[127] J. M. Zadrozny and D.E. Freedman. Qubit Control Limited by Spin-Lattice Relaxation in a Nuclear Spin-Free Iron(III) Complex. *Inorg. Chem.*, 54, 2015.

[128] D Stinghen, m atzori, and C.M. fernandes. A rare example of four-coordinate nonoxido vanadium(IV) alkoxide in the solid state: Structure, spectroscopy, and magnetization dynamics. *Inorg. Chem.*, 57(18):11393–11403, 2018.

[129] Mihail Atanasov, Daniel Aravena, Elizaveta Suturina, Eckhard Bill, Dimitrios Maganas, and Frank Neese. First principles approach to the electronic structure, magnetic anisotropy and spin relaxation in mononuclear 3d-transition metal single molecule magnets. *Coordination Chemistry Reviews*, 289-290:177–214, 2015.

[130] C. Campochiaro, E Pavel, and E Solomon. Saturation Magnetization Magnetic Circular Dichroism Spectroscopy of Systems with Positive Zero-Field Splittings: Application to Fe-SiF_6 \cdot 6H_2o. *Inorg. Chem.*, 34:4669–4675, 1995.

[131] D. Swenson, N. C. Baenziger, and D. Coucouvanis. Tetrahedral mercaptide complexes. Crystal and molecular structures of [(C6H5)4P]2M(SC6H5)4 complexes (M = cadmium(II), zinc(II), nickel(II), cobalt(II), and manganese(II)). *Journal of the American Chemical Society*, 100(6):1932–1934, March 1978. Publisher: American Chemical Society.

[132] D. Coucouvanis, D. Swenson, N. C. Baenziger, D. G. Holah, A. Kostikas, A. Simpoulos, and V. Petrouleas. The crystal and molecular structures of [(C6H5)4P]2Fe(S2C4O2)2 and

[(C6H5)4P]2Fe(SC6H5)4, a structural analog of reduced rubredoxin. *Journal of the American Chemical Society*, 98(18):5721–5723, September 1976. Publisher: American Chemical Society.

[133] Elizaveta A. Suturina, Joscha Nehrkorn, Joseph M. Zadrozny, Junjie Liu, Mihail Atanasov, Thomas Weyhermüller, Dimitrios Maganas, Stephen Hill, Alexander Schnegg, Eckhard Bill, Jeffrey R. Long, and Frank Neese. Magneto-Structural Correlations in Pseudotetrahedral Forms of the [Co(SPh)4]2– Complex Probed by Magnetometry, MCD Spectroscopy, Advanced EPR Techniques, and ab Initio Electronic Structure Calculations. *Inorganic Chemistry*, 56(5):3102–3118, March 2017. Publisher: American Chemical Society.

[134] D.E. Fenton, R.R. Schroeder, and R.L. Lintvedt. Tetrahedral Mercaptide Complexes. Crystal and Molecular Structures of [(C_6h_5)_4p]2M(SC_6h_5)_4 Complexes (M=Cd(II), Zn(II), Ni(II), Co(II), and Mn(LI)). *J. Am. Chem. Soc.*, 100:1932–1934, 1977.

[135] D. Shindo and T. Oikawa. Energy Dispersive X-ray Spectroscopy. *Springer Japan*, pages 81–102.

[136] MS Windows NT kernel description. https://www.sciencedirect.com/science/article/pii/S2666386422000728. Accessed: 2010-09-30.

[137] D. G. Holah and D. Coucouvanis. Synthesis and characterization of a new series of first row element tetrahedral mercaptide complexes. *Journal of the American Chemical Society*, 97(23):6917–6919, November 1975. Publisher: American Chemical Society.

[138] Silvia Sottini, Giordano Poneti, Samuele Ciattini, Nikolaos Levesanos, Eleftherios Ferentinos, J. Krzystek, Lorenzo Sorace, and Panayotis Kyritsis. Magnetic Anisotropy of Tetrahedral CoII Single-Ion Magnets: Solid-State Effects. *Inorganic Chemistry*, 55(19):9537–9548, October 2016. Publisher: American Chemical Society.

[139] E.J. Hawrelak, W.H. Bernskoetter, E Lobkovsky, E. Bill, and P.J. Chirik. Square planar vs tetrahedral geometry in four coordinate iron(II) complexes. *Inorg. Chem.*, 44:3103–3111, 2005.

[140] J. Cirera, S. Alvarez, F. Neese, and J. Kortus. How to Build Molecules with Large Magnetic Anisotropy. 15:4078–4087, 2009.

[141] Andrzej T. Kowal, Isabel C. Zambrano, Isabel Moura, Jose J. G. Moura, Jean LeGall, and Michael K. Johnson. Electronic and magnetic properties of nickel-substituted rubredoxin: a variable-temperature magnetic circular dichroism study. *Inorganic Chemistry*, 27(7):1162–1166, April 1988. Publisher: American Chemical Society.

[142] O. Kahn. Molecular Magnetism (VCH). 1993.

[143] Roman Boča. Zero-field splitting in metal complexes. *Coordination Chemistry Reviews*, 248(9):757–815, 2004.

[144] J. Bendix, M. Brorson, and C.E. Schäffer. Accurate Empirical Spin-Orbit Coupling Parameters \zeta nd for Gaseous ndq Transition Metal Ions. The Parametrical Multiplet Term Model. *Inorg. Chem.*, 32(13):2838–2849, 1993.

[145] Michael J. Knapp, J. Krzystek, Louis-Claude Brunel, and David N. Hendrickson. High-Frequency EPR Study of the Ferrous Ion in the Reduced Rubredoxin Model [Fe(SPh)4]2-. *Inorganic Chemistry*, 39(2):281–288, January 2000. Publisher: American Chemical Society.

[146] C Duboc, M.N. Collomb, J. Pécaut, A. Deronzier, and F. Neese. Definition of magneto-structural correlations for the MnII ion. *Chem - A Eur. J.*, 14:6498–6509, 2008.

[147] Mykhailo Azarkh, Larysa V. Penkova, Svitlana V. Kats, Oleg A. Varzatskii, Yan Z. Voloshin, and Edgar J. J. Groenen. A Mononuclear Mn(II) Pseudoclathrochelate Complex Studied by Multi-Frequency Electron-Paramagnetic-Resonance Spectroscopy. *The Journal of Physical Chemistry Letters*, 5(5):886–889, March 2014. Publisher: American Chemical Society.

[148] R.M. Wood, D.M. Stucker, L.M. Jones, W.B. Lynch, S.K. Misra, and J.H. Freed. An EPR Study of Some Highly Distorted Tetrahedral Manganese(II) Complexes at High Magnetic Fields. *Inorg. Chem.*, 38:5384–5388, 1999.

[149] Y.S. Ding, K.X. Yu, D. Reta, F. Ortu, R.E.P. Winpenny, Y.Z. Zheng, and N.F. Chilton. Field- and temperature-dependent quantum tunnelling of the magnetisation in a large barrier single-molecule magnet. *Nat. Commun.*, 9:1–10, 2018.

[150] K.S. Cole and R.H. Cole. Dispersion and absorption in dielectrics I. Alternating current characteristics. *J. Chem. Phys.*, 9:341–351, 1941.

[151] R. Orbach. Spin-lattice relaxation in rare-earth salts. *Proc. R. Soc. London. Ser. A. Math. Phys. Sco.*, 264:458–484, 1961.

[152] G. {Molnár, M. Mikolasek, K. Ridier, A. Fahs, and W. Nicolazzi. Molecular Spin Crossover Materials: Review of the Lattice Dynamical Properties. *Ann. Phys.*, 531:1–21, 2019.

[153] A. Nava, L. Rigamonti, E. Zangrando, R. Sessoli, W. Wernsdorfer, and A. Cornia. Redox-Controlled Exchange Bias in a Supramolecular Chain of Fe4 Single-Molecule Magnets. *Angew. Chem., Int. Ed.*, 54:8777–8782, 2015.

[154] S. Demir and I.-R. Jeon. Radical ligand-containing single-molecule magnets. *Coordination Chemistry Reviews*, 289-290:149–176, 2015.

[155] C.E. Jackson and I. P. Moseley. A reaction-coordinate perspective of magnetic relaxation. *Chem. Soc. Rev.*, 50:6684–6699, 2021.

[156] J. Murphy. Spin-Lattice Relaxation Due to Local Vibrations with Temperature-Independent Amplitudes. *American Physical Society*, 145(1):241–247, 1966.

[157] D. Goldfarb and S. Stoll. *EPR Spectroscopy: Fundamentals and Methods*. (Wiley-VCH). 2018.

[158] Ryogo Kubo and Kazuhisa Tomita. A general theory of magnetic resonance absorption. *Journal of the Physical Society of Japan*, 9(6):888–919, 1954.

[159] R. Kubo, T. Endo, Kamohara S., Shimizu M., M. Fujii, and Takano H. *J. Phys. Soc. Japan*, pages 1172–1177, 1987.

[160] S. A. Wolf, D. D. Awschalom, R. A. Buhrman, J. M. Daughton, S. von Molnár, M. L. Roukes, A. Y. Chtchelkanova, and D. M. Treger. Spintronics: A Spin-Based Electronics Vision for the Future. *Science*, 294(5546):1488–1495, November 2001. Publisher: American Association for the Advancement of Science.

[161] Igor Žutić, Jaroslav Fabian, and S. Das Sarma. Spintronics: Fundamentals and applications. *Reviews of Modern Physics*, 76(2):323–410, April 2004. Publisher: American Physical Society.

[162] S. D. Bader and S. S. P. Parkin. Spintronics. *Annual Review of Condensed Matter Physics*, 1(Volume 1, 2010):71–88, August 2010. Publisher: Annual Reviews.

[163] Jairo Sinova, Sergio O. Valenzuela, J. Wunderlich, C.H. Back, and T. Jungwirth. Spin Hall effects. *Reviews of Modern Physics*, 87(4):1213–1260, October 2015. Publisher: American Physical Society.

[164] Y. K. Kato, R. C. Myers, A. C. Gossard, and D. D. Awschalom. Observation of the Spin Hall Effect in Semiconductors. *Science*, 306(5703):1910–1913, 2004. _eprint: https://www.science.org/doi/pdf/10.1126/science.1105514.

[165] Charles Day. Two groups observe the spin hall effect in semiconductors. *Physics Today*, 58(2):17–19, 02 2005.

[166] J. Wunderlich, B. Kaestner, J. Sinova, and T. Jungwirth. Experimental observation of the spin-hall effect in a two-dimensional spin-orbit coupled semiconductor system. *Phys. Rev. Lett.*, 94:047204, Feb 2005.

[167] V.I. Dyakonov, M. I. Perel. Possibility of orientating electron spins with current. *Sov. J. Exp. Theor. Phys. Lett. 13*, pages 467–469, 1971.

[168] J. E. Hirsch. Spin hall effect. *Phys. Rev. Lett.*, 83:1834–1837, Aug 1999.

[169] Shufeng Zhang. Spin hall effect in the presence of spin diffusion. *Phys. Rev. Lett.*, 85:393–396, Jul 2000.

[170] C. L. Kane and E. J. Mele. Quantum spin hall effect in graphene. *Phys. Rev. Lett.*, 95:226801, Nov 2005.

[171] G. Vignale G.F. Giuliani. Quantum theory of the electron liquid. *Cambridge University Press, Cambridge England*, 2005.

[172] Karyn Le Hur Stephan Rachel. Topological insulators and mott physics from the hubbard interaction. *Phys. Rev. B*, 82:075106, Aug 2010.

[173] Stephan Rachel. Interacting topological insulators: a review. *Reports on Progress in Physics*, 81(11):116501, oct 2018.

[174] S. Datta. Electronic transport in mesoscopic systems. *Cambridge University Press*, 1995.

[175] Alain Bourgeat and Andrey Piatnitski. Approximations of effective coefficients in stochastic homogenization. *Annales de l'Institut Henri Poincare (B) Probability and Statistics*, 40:153–165, 03 2004.

[176] I. A. Baratta, J. P. Dean, J. S. Dokken, M. Habera, J. S. Hale, C. N. Richardson, M. E. Rognes, M. W. Scroggs, N. Sime, and G. N. Wells. Dolfinx: The next generation fenics problem solving environment. 2023.

Appendix A

A.1 Approximation of the effective conductivity

Let us consider the following approximation for the effective conductivity, that depend C and M,

$$\bar{\sigma}_{\mathrm{h}} \approx \langle (\sigma_{\mathrm{h}} + C(\boldsymbol{r}))\,\mathrm{erf}\left(\frac{H - H_c}{\epsilon_H} + M(\boldsymbol{r})\right)\rangle. \tag{A.1}$$

We will now show that the correlation between $C(\boldsymbol{r})$ and $M(\boldsymbol{r})$ generally leads to hump/dip features in the Hall hysteresis loops. To calculate this, we use the series expansion for the error function, and the binomial theorem, obtaining

$$\bar{\sigma}_{\mathrm{h}} = \frac{2}{\sqrt{\pi}} \sum_{n=0}^{\infty} \sum_{l=0}^{2n+1} \frac{(-2)^n (2n-1)!!}{l!(2n+1-l)!} \frac{(H - H_c)^l}{\epsilon_H^l} \langle (\sigma_{\mathrm{h}} + C(\boldsymbol{r})) M^{2n+1-l}(\boldsymbol{r})\rangle. \tag{A.2}$$

Using Wick's theorem on the two terms $\langle CM^{2n+1-l}\rangle$ and $\langle M^{2n+1-l}\rangle$, we obtain two series whose terms are non-zero for even and odd l, respectively.

Where,

$$\text{Odd } l \quad \langle M^{2n+1-l}\rangle = \langle M^{2n-2k}\rangle = \mathcal{V}_M^{n-k}\,(2n-2k-1)!!, \tag{A.3}$$

$$\text{Even } l \quad \langle CM^{2n+1-l}\rangle = \langle CM^{2n-2k+1}\rangle = \mathcal{V}_{CM}\mathcal{V}_M^{n-k}\,(2n-2k+1)!!, \tag{A.4}$$

thus we have

$$\bar{\sigma}_{\mathrm{h}} = \frac{2}{\sqrt{\pi}} \sum_{n=0}^{\infty} \sum_{k=0}^{n} \frac{(-1)^n 2^k (2n-1)!! \mathcal{V}_M^{n-k}}{(n-k)!} \left[\frac{(H - H_c)^{2k+1}}{\epsilon_H^{2k+1}(2k+1)!}\sigma_{\mathrm{h}} + \frac{(H - H_c)^{2k}}{\epsilon_H^{2k}(2k)!}\mathcal{V}_{CM}\right]. \tag{A.5}$$

A.2 Bounds of the anomalous Hall conductivity in a 2-phase composite

We first consider a simple case. A 2D conductor has random magnetic domains with the following conductivity tensors

$$\boldsymbol{\sigma}_+ = \begin{pmatrix} \sigma_0 & -\sigma_{\rm h} \\ \sigma_{\rm h} & \sigma_0 \end{pmatrix}, \ \boldsymbol{\sigma}_- = \begin{pmatrix} \sigma_0 & \sigma_{\rm h} \\ -\sigma_{\rm h} & \sigma_0 \end{pmatrix}, \tag{A.6}$$

where σ_0 and σ_h are positive constants. The spatial variation of the local conductivity tensor of the system is described by

$$\boldsymbol{\sigma}(\boldsymbol{r}) = h(\boldsymbol{r})\boldsymbol{\sigma}_+ + [1 - h(\boldsymbol{r})]\boldsymbol{\sigma}_-, \tag{A.7}$$

where $h(\boldsymbol{r}) = 1$ in the domains with the local conductivity tensor $\boldsymbol{\sigma}_+$, and 0 otherwise. We would like to understand the behavior of the effective conductivity tensor $\bar{\boldsymbol{\sigma}}$ defined as

$$\langle \boldsymbol{j} \rangle = \bar{\boldsymbol{\sigma}} \cdot \langle \boldsymbol{E} \rangle, \tag{A.8}$$

where $\langle \dots \rangle$ means spatial average. In general $\bar{\boldsymbol{\sigma}}$ depends on the form of $h(\boldsymbol{r})$. So we will focus on the bounds of the components of $\bar{\boldsymbol{\sigma}}$.

We first perform a duality transformation which can transform $\boldsymbol{\sigma}(\boldsymbol{r})$ to diagonal tensors. The general form of the duality transformation is [93]

$$\boldsymbol{\sigma}' = (a\boldsymbol{\sigma} + b\boldsymbol{R}_\perp) \cdot (c\boldsymbol{I} + d\boldsymbol{R} \cdot \boldsymbol{\sigma})^{-1}, \tag{A.9}$$

where

$$\boldsymbol{R}_\perp = \begin{pmatrix} 0 & -1 \\ 1 & 0 \end{pmatrix} \tag{A.10}$$

is the $\pi/2$ rotation matrix, and a, b, c, d are arbitrary constants. It can be proved [91, 93] that the effective conductivity tensors for $\boldsymbol{\sigma}'$ and $\boldsymbol{\sigma}$ are related by the following equation

$$\bar{\boldsymbol{\sigma}}' = (a\bar{\boldsymbol{\sigma}} + b\boldsymbol{R}_\perp) \cdot (c\boldsymbol{I} + d\boldsymbol{R}_\perp \cdot \bar{\boldsymbol{\sigma}})^{-1}, \tag{A.11}$$

which will be used later to obtain the bounds of $\bar{\boldsymbol{\sigma}}$ from that of $\bar{\boldsymbol{\sigma}}'$.

$\boldsymbol{\sigma}'$ can be made diagonal by choosing $a = d = 1$ and

$$b = c = \sqrt{\sigma_0^2 + \sigma_h^2} \equiv \sqrt{\Delta}. \tag{A.12}$$

The explicit form of $\boldsymbol{\sigma}'$ in different domains, $\boldsymbol{\sigma}'_\pm$, is

$$\boldsymbol{\sigma}'_\pm = \frac{2\sigma_0\sqrt{\Delta}}{\sigma_0^2 + (\sqrt{\Delta} \mp \sigma_h)^2}\boldsymbol{I} \equiv \sigma'_\pm \boldsymbol{I}. \tag{A.13}$$

We have therefore transformed the original problem into a problem of finding the effective conductivity of the composite formed by two phases with different isotropic conductivities. The bounds of such an effective conductivity have been given in [88, 94], obtained using variational approaches. When applied to our problem they give

$$\bar{\sigma}' \in \left[\sigma'_- \frac{\sigma'_-\sigma_0 + (1+p)\sigma_h}{\sigma'_-\sigma_0 + (1-p)\sigma_h}, \sigma'_+ \frac{\sigma'_+\sigma_0 - (2-p)\sigma_h}{\sigma'_+\sigma_0 - p\sigma_h}\right], \tag{A.14}$$

where p is the area ratio of domains with $\boldsymbol{\sigma}_+$. According to [88], the bounds are realized when the composite has the form of packed coated cylinders (in 2D). In our case, such a configuration means that the system can be partitioned into circular coated cells of arbitrary sizes with the core being one domain and the shell or coating being the other domain, and the area ratio of the two domains in each cell is fixed to $p/(1-p)$. Now let $\bar{\boldsymbol{\sigma}} \equiv \bar{\sigma}_0\boldsymbol{I} + \bar{\sigma}_h\boldsymbol{R}_\perp$. Eq. (A.11) indicates that

$$\begin{aligned} \bar{\sigma}' &= \frac{\bar{\sigma}_0}{\sqrt{\Delta} - \bar{\sigma}_h}, \\ \bar{\sigma}_0^2 + \bar{\sigma}_h^2 &= \sigma_0^2 + \sigma_h^2 = \Delta, \end{aligned} \tag{A.15}$$

from which we can obtain

$$\bar{\sigma}' = \frac{\sqrt{\Delta - \bar{\sigma}_h^2}}{\sqrt{\Delta} - \bar{\sigma}_h}. \tag{A.16}$$

Combining Eqs. (A.14) and (A.16), we finally obtain the bounds of $\bar{\sigma}_h$:

$$\bar{\sigma}_h \in \left[-\sigma_h + \frac{2p\sigma_0^2\sigma_h}{\sigma_0^2 + (1-p)^2\sigma_h^2},\ \sigma_h - \frac{2(1-p)\sigma_0^2\sigma_h}{\sigma_0^2 + p^2\sigma_h^2} \right], \tag{A.17}$$

which takes the values of $\pm\sigma_h$ when $p = 1$ and $p = 0$, respectively, as expected. More importantly, one can see that the absolute value of $\bar{\sigma}_h$ can never exceed σ_h. The two bounds reduce to the trivial value $(2p-1)\sigma_h$ when $\sigma_h/\sigma_0 \to 0$, and $(2p-1)\sigma_h$ is also in-between the two bounds.

We next consider a slightly more complex case: the two domains have the following conductivity tensors

$$\boldsymbol{\sigma}_+ = \begin{pmatrix} \sigma_1 & -\sigma_\mathrm{h} \\ \sigma_\mathrm{h} & \sigma_1 \end{pmatrix},\ \boldsymbol{\sigma}_- = \begin{pmatrix} \sigma_2 & \sigma_\mathrm{h} \\ -\sigma_\mathrm{h} & \sigma_2 \end{pmatrix}, \tag{A.18}$$

with $\sigma_1 \neq \sigma_2$. Thus there is certain correlation between the longitudinal and Hall conductivities. For example, if $\sigma_1 > \sigma_2$, one can say that the positive magnetization domains have larger conductivity than the negative magnetization domains. Such situations could happen during a magnetization reversal, when the domains with negative magnetization first nucleate at the regions with lower conductivities or more defects, which is physically sensible. Note that the sense of positive and negative is reversed when considering the other half of the hysteresis curve during the magnetization reversal. Assume one starts from the uniform positive magnetization case with positive anomalous Hall conductivity, and slowly decreases the magnetic field. Negative magnetization domains will start to nucleate at regions with smaller longitudinal conductivity. However, when one starts from the uniform negative magnetization in the other half of the hysteresis curve, *positive* magnetization domains will first nucleate at regions with smaller longitudinal conductivity. Thus

the values of $\sigma_h(\boldsymbol{r})$ can be either positive- or negative-correlated with the longitudinal conductivity, depending on the material and on which half of the hysteresis curve is under consideration.

By using the same approach in the above section, after some algebra one can obtain the following bounds for $\bar{\sigma}_h$:

$$\bar{\sigma}_h/\sigma_h \in \left[-1+\frac{8p\sigma_2^2}{[(1-p)\sigma_1+(1+p)\sigma_2]^2+4(1-p)^2\sigma_h^2},\ 1-\frac{8(1-p)\sigma_1^2}{[(2-p)\sigma_1+p\sigma_2]^2+4p^2\sigma_h^2}\right] \tag{A.19}$$

Apparently $|\bar{\sigma}_h| < \sigma_h$, so that the absolute value of the effective Hall conductivity cannot exceed that of the local Hall conductivity. Nonetheless, Eq. (A.19) suggests that it is possible for the lower bound to go above the simple average $2p-1$ when

$$\sigma_2^2 \geqslant \left(\frac{1-p}{2}\sigma_1+\frac{1+p}{2}\sigma_2\right)^2+(1-p)^2\sigma_h^2, \tag{A.20}$$

which is easily satisfied when $\sigma_2 > \sigma_1$, and $\sigma_h \ll \sigma_1$. Conversely, the upper bound can be lower than the simple average when

$$\sigma_1^2 \geqslant \left(\frac{2-p}{2}\sigma_1+\frac{p}{2}\sigma_2\right)^2+p^2\sigma_h^2, \tag{A.21}$$

which is easily satisfied when $\sigma_1 > \sigma_2$ and $\sigma_h \ll \sigma_2$.

Interestingly, Eqs. (A.20) and (A.21) may explain the following behavior in certain experiments: When plotting the anomalous Hall conductivity versus the total magnetization, sometimes there is also hysteresis, which suggests that the effective anomalous Hall conductivity is not strictly proportional to the total magnetization throughout the magnetization reversal. Note that the total magnetization is nothing but $(2p-1)M_0$, where M_0 is the saturated magnetization. Since the designations of σ_1 and σ_2 are interchanged for the two halves of the hysteresis curve, it is indeed possible to have a hysteretic dependence between $\bar{\sigma}_h$ (bounded by Eq. (A.19)) and the total magnetization, when Eqs. (A.20) or (A.21) are satisfied. We should nonetheless note that the simple correlation in Eq. (A.18) does not apply throughout the hysteresis curve, as the regions with σ_1

and σ_2 are independent of magnetization. So this conclusion needs to be verified by more realistic numerical calculations.

A.3 Proof of Theorem 1

This section was completed by Evan Camrud, and Olivier Pinaud.

We recall that the microscopic conductivity reads $\boldsymbol{\sigma}(\boldsymbol{r}) = \boldsymbol{\sigma}_0(\boldsymbol{r}) + \sigma_{\rm h}(\boldsymbol{r})\mathbf{R}_\perp$, for $\boldsymbol{\sigma}_0(\boldsymbol{r})$ a positive definite diagonal matrix with entries σ_{xx} and σ_{yy}, and $\mathbf{R}_\perp$ the $\pi/2$ rotation matrix. We denote by $\bar{\boldsymbol{\sigma}}$ the corresponding effective conductivity with effective Hall conductivity $\bar{\sigma}_{\rm h}$. The assumptions in the theorem ensure that the effective conductivity is well-defined and constant [95].

The main ingredient of the proof is a variational formula for the homogenized coefficients. Before getting to this, the standard theory of stochastic homogenization gives first the following expression for the effective conductivity, see [175]:

$$\bar{\boldsymbol{\sigma}} = \lim_{L\to\infty} \boldsymbol{\sigma}^L, \tag{A.22}$$

where the Hall conductivity of $\boldsymbol{\sigma}^L$ is

$$\sigma_{\rm h}^L = \frac{1}{L^2}\int_{\Omega_L} \big(\boldsymbol{\sigma}(\mathbf{r})\nabla(\phi_\xi(\mathbf{r}) + \xi\cdot\mathbf{r})\big)\cdot\xi_\perp d\mathbf{r}. \tag{A.23}$$

Above, $\Omega_L = [-L/2, L/2]\times[-L/2, L/2]$, $\xi = (1,0)^T$, $\xi_\perp = (0,1)^T$ (T is for transposition), and for each $u\in\mathbb{R}^2$, ϕ_u is the unique (weak) solution to the corrector equation

$$\nabla\cdot\Big(\boldsymbol{\sigma}(\boldsymbol{r})\nabla(\phi_u(\mathbf{r}) + u\cdot\mathbf{r})\Big) = 0 \qquad \text{in } \Omega_L, \tag{A.24}$$

equipped with zero Dirichlet conditions at the boundary of Ω_L. Similar expressions hold for the diagonal terms in $\boldsymbol{\sigma}^L$ but these will not be needed.

In (A.22), the limit holds for almost all (in the probabilistic sense) realizations of the random fields σ_{xx}, σ_{yy} and $\sigma_{\rm h}$, and (A.23), (A.24) are defined for one of these realizations. Working with

$\boldsymbol{\sigma}^L$ instead of $\bar{\boldsymbol{\sigma}}$ makes it possible to make use of the following variational characterization of the homogenized conductivity. Further, we denote by $\boldsymbol{\sigma}_s^L = (\boldsymbol{\sigma}^L + (\boldsymbol{\sigma}^L)^T)/2$ (resp. $\boldsymbol{\sigma}_s = (\boldsymbol{\sigma} + \boldsymbol{\sigma}^T)/2)$) the symmetric part of $\boldsymbol{\sigma}^L$ (resp. $\boldsymbol{\sigma}$) and by $\boldsymbol{\sigma}_a^L = (\boldsymbol{\sigma} - (\boldsymbol{\sigma}^L)^T)/2$ (resp. $\boldsymbol{\sigma}_a = (\boldsymbol{\sigma} - \boldsymbol{\sigma}^T)/2)$) its antisymmetric part. Since (A.23) is the expression of the effective coefficient in standard periodic homogenization, we have, according to [88], page 277, for ξ_s and ξ_a two arbitrary vectors in $\mathbb{R}^2$,

$$\begin{pmatrix} \xi_s \\ \xi_a \end{pmatrix} \cdot \begin{pmatrix} -\boldsymbol{\sigma}_s^L & -\boldsymbol{\sigma}_a^L \\ \boldsymbol{\sigma}_a^L & \boldsymbol{\sigma}_s^L \end{pmatrix} \begin{pmatrix} \xi_s \\ \xi_a \end{pmatrix} =$$

$$\begin{array}{cc} \max & \min \\ \nabla \times e_s(\mathbf{r}) = 0 & \nabla \times e_a(\mathbf{r}) = 0 \\ < e_s >= \xi_s & < e_a >= \xi_a \end{array} \left\langle \begin{pmatrix} e_s \\ e_a \end{pmatrix} \cdot \begin{pmatrix} -\boldsymbol{\sigma}_s(\mathbf{r}) & -\boldsymbol{\sigma}_a(\mathbf{r}) \\ \boldsymbol{\sigma}_a(\mathbf{r}) & \boldsymbol{\sigma}_s(\mathbf{r}) \end{pmatrix} \begin{pmatrix} e_s \\ e_a \end{pmatrix} \right\rangle$$

where $\langle f \rangle = \int_{\Omega_L} f(\mathbf{r}) d\mathbf{r}/L^2$. The critical points solution to the saddle point problem are $\bar{e}_s = (\nabla\phi_\zeta + \nabla\phi'_{\zeta'})/2$ and $\bar{e}_a = (\nabla\phi_\zeta - \nabla\phi'_{\zeta'})/2$, where $\zeta = \xi_s + \xi_a$, $\zeta' = \xi_s - \xi_a$ and $\phi'_{\zeta'}$ solves (A.24) with $\boldsymbol{\sigma}$ replaced by $\boldsymbol{\sigma}^T$ and $u = \zeta'$.

With $\xi_s = (1,1)^T/2$, $\xi_a = (1,-1)^T/2$, and the fact that $\boldsymbol{\sigma}_a = \sigma_{\mathrm{h}} \mathbf{R}_\perp$ as well as $\boldsymbol{\sigma}_a^L = \sigma_{\mathrm{h}}^L \mathbf{R}_\perp$, direct algebra shows that

$$\sigma_{\mathrm{h}}^L = \begin{array}{cc} \min & \max \\ \nabla \times e_s(\mathbf{r}) = 0 & \nabla \times e_a(\mathbf{r}) = 0 \\ < e_s >= \xi_s & < e_a >= \xi_a \end{array} F_{\sigma_{\mathrm{h}}}(e_s, e_a) \tag{A.25}$$

where $F_{\sigma_{\mathrm{h}}}(e_s, e_a) =< e_s \cdot \boldsymbol{\sigma}_s e_s > - < e_a \cdot \boldsymbol{\sigma}_s e_a > + 2 < \sigma_{\mathrm{h}} e_s \cdot \mathbf{R}_\perp e_a >$. We now bound σ_{h}^L above and below. For this, since the assumption $-\sigma_M \leq \sigma_{\mathrm{h}} \leq \sigma_M$ holds, we have, independently of the sign of $e_s \cdot \mathbf{R}_\perp e_a$,

$$-\sigma_M (e_s \cdot \mathbf{R}_\perp e_a) \leq \sigma_{\mathrm{h}} (e_s \cdot \mathbf{R}_\perp e_a) \leq \sigma_M (e_s \cdot \mathbf{R}_\perp e_a).$$

As a consequence, we obtain from the definition of $F_{\sigma_{\rm h}}$ the inequality

$$F_{-\sigma_M}(e_s, e_a) \leq F_{\sigma_{\rm h}}(e_s, e_a) \leq F_{\sigma_M}(e_s, e_a),$$

which, according to the variational principle (A.25), implies that

$$\sigma^L_{\rm h,-} \leq \sigma^L_{\rm h} \leq \sigma^L_{\rm h,+}. \tag{A.26}$$

Above, $\sigma^L_{\rm h,\pm}$ is the homogenized Hall coefficient associated with the microscopic conductivity $\boldsymbol{\sigma}_\pm(\boldsymbol{r}) = \boldsymbol{\sigma}_0(\boldsymbol{r}) \pm \sigma_M \mathbf{R}_\perp$. To conclude the proof, it suffices then to show that $\lim_{L\to\infty} \sigma^L_{\rm h,\pm} = \pm\sigma_M$. This is done as follows. In the same way as (A.23), we have the following expression for $\sigma^L_{\rm h,+}$:

$$\sigma^L_{\rm h,+} = \frac{1}{L^2} \int_{\Omega_L} \big(\boldsymbol{\sigma}_+(\mathbf{r}) \nabla(\phi^+_\xi(\mathbf{r}) + \xi \cdot \mathbf{r})\big) \cdot \xi_\perp d\mathbf{r} \tag{A.27}$$

for the ξ and $\xi_\perp$ defined earlier. The function ϕ^+_ξ is the weak solutions to (A.24) with $\boldsymbol{\sigma}$ replaced by $\boldsymbol{\sigma}_+$. Since the off-diagonal entries of $\boldsymbol{\sigma}_+$ are equal to $\pm\sigma_M$ and are therefore constant, ϕ^+_ξ is actually solving (A.24) with $\boldsymbol{\sigma}$ replaced by $\boldsymbol{\sigma}_0$, that is

$$\nabla \cdot \Big(\boldsymbol{\sigma}_0(\boldsymbol{r}) \nabla(\phi^+_\xi(\mathbf{r}) + \xi \cdot \mathbf{r})\Big) = 0 \qquad \text{in } \Omega_L, \tag{A.28}$$

equipped with Dirichlet boundary conditions at the boundary of Ω_L. Multiplying (A.28) by $\xi_\perp \cdot \mathbf{r}$ and integrating by parts yields

$$L^{-2} \int_{\Omega_L} \big(\boldsymbol{\sigma}_0(\mathbf{r}) \nabla(\phi^+_\xi(\mathbf{r}) + \xi \cdot \mathbf{r})\big) \cdot \xi_\perp d\mathbf{r} = L^{-2} \int_{\partial\Omega_L} \boldsymbol{n} \cdot (\sigma_0(\mathbf{r})\xi)(\xi_\perp \cdot \mathbf{r}) dS,$$

where the right-hand-side corresponds to line integrals along the boundary $\partial\Omega_L$ of Ω_L and $\boldsymbol{n}$ is the outward unit normal to $\partial\Omega_L$. We denote the last term above by T_L. This allows us to rewrite $\sigma^L_{\rm h,+}$

as

$$\begin{aligned}\sigma^L_{\mathrm{h},+} &= \frac{1}{L^2}\int_{\Omega_L}\big(\boldsymbol{\sigma}_0(\mathbf{r})\nabla(\phi^+_\xi(\mathbf{r})+\xi\cdot\mathbf{r})\big)\cdot\xi_\perp d\mathbf{r} + \frac{\sigma_M}{L^2}\int_{\Omega_L}\big(\mathbf{R}_\perp\nabla(\phi^+_\xi(\mathbf{r})+\xi\cdot\mathbf{r})\big)\cdot\xi_\perp d\mathbf{r}\\ &= T_L + \sigma_M + \frac{\sigma_M}{L^2}\int_{\Omega_L}\big(\mathbf{R}_\perp\nabla\phi^+_\xi(\mathbf{r})\big)\cdot\xi_\perp d\mathbf{r}.\end{aligned}$$

Above, we used that $(\mathbf{R}_\perp\xi)\cdot\xi_\perp = 1$. Besides, the last term is equal to zero since ϕ^+_ξ vanishes on $\partial\Omega_L$. We now show that $\lim_{L\to\infty} T_L = 0$, which is a consequence of Birkhoff ergodic theorem. Indeed, direct calculations show that

$$T_L = \frac{1}{L^2}\int_{-L/2}^{L/2}\delta\sigma_{xx}(y)ydy = \int_{-1/2}^{1/2}\delta\sigma_{xx}(Ly)ydy,$$

where $\delta\sigma_{xx}(y) = \sigma_{xx}|_{x=L/2} - \sigma_{xx}|_{x=-L/2}$ (we recall that $\mathbf{r} = (x,y)$). We now exploit the separation of scales between $\delta\sigma_{xx}(Ly)$ and the function y. Let N_L be the integer part of $\sqrt{L}$. We break the interval $[-1/2, 1/2]$ into N_L intervals of length $1/N_L$ centered at $y_k = -1/2 + 1/(2N_L) + (k-1)/N_L$, for $k = 1, \cdots, N_L$. We denote these intervals by I_k. Hence,

$$T_L = \sum_{k=1}^{N_L}\int_{I_k}\delta\sigma_{xx}(Ly)ydy.$$

On each I_k, the function y varies slowly compared to $\delta\sigma_{xx}(Ly)$ for large L, and we can write

$$T_L = \sum_{k=1}^{N_L} y_k\int_{I_k}\delta\sigma_{xx}(Ly)dy + o(1),$$

where $o(1)$ is a term that goes to zero as $L\to\infty$. Since the random field $\delta\sigma_{xx}$ is stationary and ergodic, Birkhoff ergodic theorem implies that

$$\lim_{L\to\infty} N_L\int_{I_k}\delta\sigma_{xx}(Ly)dy = \mathbb{E}\{\delta\sigma_{xx}\}.$$

Note that $\mathbb{E}\{\delta\sigma_{xx}\}$ does not depend on position by stationarity of $\delta\sigma_{xx}$. This shows that

$$\begin{aligned} T_L &= N_L^{-1}\sum_{k=1}^{N_L} y_k N_L \int_{I_k} \delta\sigma_{xx}(Ly)dy + o(1) \\ &= \mathbb{E}\{\delta\sigma_{xx}\}N_L^{-1}\sum_{k=1}^{N_L} y_k + o(1) \\ &= \mathbb{E}\{\delta\sigma_{xx}\}\int_{-1/2}^{1/2} y dy + o(1). \end{aligned}$$

In the last line, we used the fact that $N_L^{-1}\sum_{k=1}^{N_L} y_k$ is a Riemann sum for the integral $\int_{-1/2}^{1/2} y dy$. Since σ_{xx} is stationary, it follows that $\mathbb{E}\{\sigma_{xx}\}$ is independent of position and as a consequence $\mathbb{E}\{\delta\sigma_{xx}\} = 0$. Hence $\lim_{L\to\infty} T_L = 0$ and $\lim_{L\to\infty} \sigma_{\mathrm{h},+}^L = \sigma_M$. We prove in the same way that $\lim_{L\to\infty} \sigma_{\mathrm{h},-}^L = -\sigma_M$.

We are now in position to conclude. Since $\lim_{L\to\infty} \sigma_{\mathrm{h},\pm}^L = \pm\sigma_M$ and $\lim_{L\to\infty} \sigma_{\mathrm{h}}^L = \bar{\sigma}_{\mathrm{h}}$, it suffices to pass to the limit in (A.26) to obtain $-\sigma_M \leq \bar{\sigma}_{\mathrm{h}} \leq \sigma_M$. This ends the proof of Theorem 1.

A.4 Homogenized Hall conductance in the presence of domain walls

Supplementary Fig. A.1 shows the finite-element results of Hall conductance G_{h} obtained by inverting the resistance tensor followed by antisymmetrization for 250 random instances of parameter sets using the domain wall resistivity model, as indicated in the figure caption.

A.5 FEniCS

To further explore how the domain wall resistivity effects the Hall response, we approached this problem numerically using FEniCS, a PDE solver implemented with Python [176]. To use FEniCS, we must precisely state the problem you wish to solve, the steps are as follows. One is to

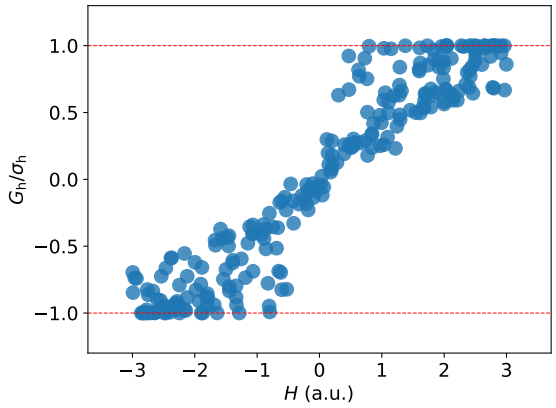

Figure A.1: Hall conductance G_{h} normalized to σ_{h}, obtained by inverting the resistance tensor for random realizations of the domain configurations in the presence of domain wall resistivities. $G_{\mathrm{h}}/\sigma_{\mathrm{h}}$ is strictly bounded within ± 1. The parameters used are $\xi \in [5 \times 10^{-3}, 5 \times 10^{-2}]$, $\sigma_{\perp} \in [-0.8, -0.1]$, $\sigma_{\parallel} \in [-0.7, -0.1]$, $\sigma_{\mathrm{h}} \in [0.05, 0.5]$, $\epsilon_W \in [0.2, 2.0]$, $\epsilon_H \in [0.2, 2.0]$, $H \in [-3.0, 3.0]$, $H_c = 0.0$, $\epsilon_W = 2.0$, $\sigma_0 = E_0 = 1.0$.

identify the domain, PDE, boundary conditions, and source terms. Next is to reformulate the PDE as a finite element variational problem. Then to write the python code, then call FEniCS.

The first step,

$$\nabla \cdot \sigma(\text{-}\nabla u(\mathbf{x})) = f(\mathbf{x});\ \mathbf{x} \in \Omega \tag{A.29}$$

$$u(\mathbf{x}) = u_D(\mathbf{x});\ \mathbf{x} \in \partial\Omega_D \tag{A.30}$$

$$\hat{\mathbf{n}} \cdot (\text{-}\sigma \nabla u(\mathbf{x})) = g(\mathbf{x});\ \mathbf{x} \in \partial\Omega_N \tag{A.31}$$

with $u(\mathbf{x})$ is the unknown trial function, $f(\mathbf{x})$ is the source function, $u_D(\mathbf{x})$ is the known Dirichlet boundary condition, and $g\mathbf{x})$ is the known Neumann boundary condition, Ω is the spatial domain of $u(\mathbf{x})$, and $\partial\Omega$ is the boundary of Ω.

Next, we multiply eqn (A.29) by a test function $v(\mathbf{x})$ that satisfies the Dirichlet boundary conditions, $v(\mathbf{x}) = 0; x \in \partial\Omega$, and integrate over the domain.

$$\text{-}\int_{\Omega} d\mathbf{x}\, v(\mathbf{x}) \nabla \cdot \sigma \nabla u(\mathbf{x}) = \int_{\Omega} d\mathbf{x}\, v(\mathbf{x}) f(\mathbf{x}) \tag{A.32}$$

The next step is to reduce the order of polynomial order of v and u to be as low as possible. This reduces the requirement of the polynomials used in the trial functions, here from being twice differentiable, down to once differentiable. This is a common practice using Finite Element method, because while the test functions that we cast over the domain Ω are required to be continuous, their first derivatives are not. This means that that the second derivatives are not as well defined. Doing by-parts on the left hand side of eqn (A.32) yields,

$$\begin{aligned} &=\text{-}\int_{\Omega} d\mathbf{x}\, v(\mathbf{x})\nabla\cdot\sigma\nabla u(\mathbf{x}) \\ &=\int_{\Omega} d\mathbf{x}\, \nabla v(\mathbf{x})\cdot(\sigma\nabla u(\mathbf{x})) - \int_{\partial\Omega} d\mathbf{S}\, v(\mathbf{x})\hat{\mathbf{n}}\cdot(\sigma\nabla u(\mathbf{x})) \\ &=\int_{\Omega} d\mathbf{x}\, \nabla v(\mathbf{x})\cdot(\sigma\nabla u(\mathbf{x})) + \int_{\partial\Omega_N} d\mathbf{S}\, v(\mathbf{x})g(\mathbf{x}) \end{aligned} \tag{A.33}$$

Using this result, and rearranging eqn (A.32) we get,

$$\int_{\Omega} d\mathbf{x}\, \nabla v(\mathbf{x})\cdot\sigma\nabla u(\mathbf{x}) = \int_{\Omega} d\mathbf{x}\, v(\mathbf{x})f(\mathbf{x}) - \int_{\partial\Omega_N} d\mathbf{S}\, v(\mathbf{x})g(\mathbf{x}) \tag{A.34}$$

Note the right hand side is completely known. If we require eqn (A.34) to hold for all $v(\mathbf{x}) \in \tilde{V}$, so-called test space, we obtain a problem that uniquely determines the solution $u(\mathbf{x}) \in V$, which lies within a possibly different function space. This is the weak form, or variational form of the original PDE.

The computational implementation proceeds as follows. First, we define the the domain Ω using FEniCS,

```
mesh=fen.UnitSquareMesh(N,N)
```

This creates a mesh over the unit square $[0,1]\times[0,1]$, where the parameter N specifies the number of subdivisions along each axis. Each square is then divided into two triangles. FEniCS also supports more complex domains constructed via unions and intersections of simpler shapes, and external mesh generation tools can be used for greater flexibility.

Next, we define the function space:

```
V = fen.FunctionSpace(mesh, "Lagrange", 1),
```

this creates a finite element space `V` over the mesh, using first-order (linear) Lagrange elements.

The trial and test functions, along with the source term, are defined as:

```
u = fen.TrialFunction(V)
v = fen.TestFunction(V)
f = fen.Constant(0)
```

Here, `u` and `v` are defined over `V`, and `f` represents a source (or sink), which we take to be zero.

We impose boundary conditions via:

```
bc1 = fen.Expression("x[0]==0? -1.0", degree = 1)
bc2 = fen.Expression("x[0]==0? -1.0", degree = 1)
g = bc1 + bc2
```

This corresponds to current flowing in from the left ($x = 0$) and out on the right ($x = 1$), with `g` encoding the total boundary condition.

We now define the bilinear form corresponding to the left-hand side of Eq. (A.34). The weak form is implemented as:

```
a=(( sig00 * u.dx(0) + sig01 * u.dx(1))*v.dx(0)
  +
   ( sig10 * u.dx(0) + sig11 * u.dx(1))*v.dx(1))*fen.dx
```

here `sig00` corresponds to σ_{11}, and so forth for the other components. The right-hand side is given by:

```
L = f*v*fen.dx - g*v*fen.ds
```

All terms in `L` are known functions.

The problem is then solved using:

```
fen.solve(a==L, u)
```

yielding `u`, the numerical solution defined over the domain.